Macroporous electrospun indium tin oxide electrodes for spectroelectrochemical analysis

Maciej Mierzwa

Sujet de thèse:

Electrodes macroporeuses d'oxyde d'indium dopé à l'étain préparées par électrofilage pour l'analyse spectroélectrochimique

Par

Maciej MIERZWA

Pour l'obtention de titre de **Docteur** de l'Université de Lorraine

Ecole Doctorale : Synthèse, Simulations, Applications: de la Molécule aux Edifices

Supramoléculaires (SESAMES), ED 412

Soutenance publique prévue le 7 décembre 2017 devant le jury composé de :

Rapporteurs: Neso Sojic, Professeur, Université de Bordeaux

Christine Kranz, Professeur, University of Ulm

Examinateurs: Solenne Fleutot, Maître de conférences, Université de Lorraine

Lydie Viau, Chargée de Recherches, Université de Franche-Comté

Directeur: Dr. Mathieu Etienne, Université de Lorraine

Co-directeur: Dr. Emmanuel Lamouroux, Maître de conférences, Université de Lorraine

_____

Laboratoire de Chimie Physique et Microbiologie pour l'Environnement (LCPME)

Unité mixte de recherche – UMR 756

405 Rue de Vandoeuvre, 54600, Villers-lès-Nancy, France

Structure et Réactivité des Systèmes Moléculaires Complexes (SRSMC)

UMR CNRS 7565

Boulevard des Aiguillettes BP 239, 54506, Vandoeuvre les Nancy

Acknowledgements

Table of contents

Abstract

There is a growing interest in finding new and commercially viable methods for performing spectroelectrochemical analysis. One of the new ideas is to use porous and transparent electrodes to achieve better selectivity, higher sensitivities and lower limits of detection. During this study, the electrospinning technique was employed for the production of electrodes that would fulfill these criteria. Firstly, a survey of the literature on meso- and macroporous and transparent electrodes is provided. It is concluded that this type of electrode with their higher surface area can indeed improve the spectral signal as well as the electrochemical response. With that in mind, an electrospinning protocol was used to form free-standing indium tin oxide nanofiber films. They were prepared from a suspension of polyvinylpyrrolidone (PVP) and indium and tin precursors with a ratio Sn/In =0.16. It was possible to manipulate the diameter of the fibers in the range between 110 and 235 nm. The thickness of the layer was adjustable between 12 and 120 μm depending on the time of preparation. Two-step heat treatment was necessary to obtain the final material: (1) to calcinate the layer and convert the raw material into indium tin oxide which was confirmed by X-ray diffractometry, (2) to ensure higher conductivity of the layer through sintering and introduction of oxygen vacancies. The electrochemical properties of the nanofibers have been characterized and optimized using dimethanolferrocene as a model probe. This porous ITO electrode has been applied to the electroanalysis of ascorbic acid and to spectroelectrochemistry using Prussian blue as a model system. Furthermore, the same electrospinning protocol was used to deposit macroporous layers on the solid substrate to achieve a higher mechanical stability. It was made possible by using a polystyrene film to prevent the delamination during calcination shrinking. This protocol also induced a change of morphology that resulted in the formation of highly interconnected nanofilaments of sizes between 70 and 170 nm. This new electrode material was found to be more stable and compact compared to free-standing mats. It was also more transparent. Another attribute of those electrodes were excellent electrochemical properties in comparison to a flat ITO electrode, like greatly enhanced oxidation of ascorbic acid. Moreover, the layers functionalized with methylated mesostructured silica were applied in detection of methylene blue with a linear range of detection between 20 nM and 2 μM and a limit of detection at 16.9 nM. A dynamic spectroelectrochemical measurement of dye mixture was also performed to show the capabilities of such electrode. Finally, the ITO nanofilament electrodes were used in electrochemiluminescence (ECL) generation with $Ru(bpy)_3^{2+}$ complex as luminophore and

tripropylamine as a co-reactant in three different modes. In the first one, both reagents were dissolved in the solution, and bare ITO nanofilaments were found to generate almost 7 times higher emission than flat ITO. Next, the Ru (II) complex was adsorbed on electrodes functionalized with silica, and similarly, the ECL generation was found to be 7 times higher than on flat ITO but the decay rate over several cycles suggested that it was not a stable method of immobilization. In the last mode, the complex derived from $Ru(bpy)_3^{2+}$ was covalently bound to the silica layer, and while the increase over flat ITO was only 6 times this method proved to be more stable over the longer time period, retaining about 75% of the original ECL intensity after 40 minutes, compared to 25% for the adsorbed complex.

Resumé

Il y a un intérêt croissant concernant la mise au point de nouvelles méthodes robustes pour réaliser des analyses spectro-électrochimiques. L'une des approches consiste à utiliser des électrodes poreuses et transparentes afin d'obtenir une meilleure sélectivité, des sensibilités plus élevées ainsi que des limites de détection inférieures. Au cours de cette étude, la technique d'électrofilage a été utilisée pour la préparation d'électrodes répondant à ces critères. Tout d'abord, l'analyse de la littérature sur les électrodes méso- et macro-poreuses et transparentes réalisée permet de conclure que ce type d'électrode—présentant une surface spécifique supérieure¬ aux électrodes planes—peut effectivement améliorer le signal spectral. Ainsi, un protocole d'électrofilage a été utilisé pour former des films autosupportés de nanofibres d'oxyde d'indium dopé à l'étain (indium tin oxide : ITO). Ils ont été préparés à partir d'une suspension de polyvinylpyrrolidone (PVP) et de précurseurs d'indium et d'étain avec un rapport Sn/In = 0,16. Les paramètres du procédé de préparation ont permis de contrôler le diamètre des fibres (entre 110 et 235 nm) ainsi que l'épaisseur de la couche (de 12 à 120 μm en fonction du temps de dépôt). Un traitement thermique en deux étapes est nécessaire pour (1) calciner la couche et convertir les précurseurs en oxyde d'indium et d'étain (confirmé par diffraction des rayons X), (2) améliorer la conductivité de la couche par frittage et introduction de sites vacants en oxygène. Les propriétés électrochimiques des nanofibres ainsi obtenues ont été caractérisées et optimisées en utilisant du diméthanolferrocène comme sonde modèle. Ce type d'électrode poreuse a été employée pour l'électroanalyse de l'acide ascorbique et pour la spectroélectrochimie utilisant le bleu de Prusse comme système modèle. En outre, la technique d'électrofilage a été utilisée pour le dépôt des couches macroporeuses sur un substrat solide afin d'obtenir une stabilité mécanique plus élevée. Le passage d'un matériau autosupporté à un matériaux supporté sur substrat plan solide a nécessité l'utilisation d'un film de polystyrène pré-déposé afin d'empêcher le délaminage pendant l'étape de calcination. Cette modification du protocole a conduit à la formation de nanofilaments de diamètre compris entre 70 et 170 nm fortement interconnectés. Ce nouveau matériau d'électrode s'est révélé plus stable, plus compact mais également plus transparent que le matériau autosupporté.

Une autre caractéristique de ces électrodes était leurs excellentes propriétés électrochimiques par rapport à une électrode d'ITO plane, permettant une nette amélioration de l'oxydation de l'acide ascorbique. Ces couches de nanofilaments d'ITO, après fonctionnalisation avec de la silice mésostructurée méthylée, ont également été testées pour la détection du bleu de

méthylène conduisant à une réponse linéaire entre 20 nM et 2 µM et une limite de détection de 16.9 nM. De plus, une mesure spectroélectrochimique dynamique d'un mélange de colorants a été effectuée pour montrer les capacités d'une telle électrode. Enfin, les électrodes de nanofilaments d'ITO ont été utilisées pour la génération d'électrochimiluminescence (ECL) avec le complexe $Ru(bpy)_3^{2+}$ comme luminophore et la tripropylamine en tant que co-réactif. Le complexe a été lié de manière covalente à la couche de silice. La génération d'ECL par rapport à l'ITO plan est 6 fois supérieure. L'immobilisation covalente permet de conserver environ 75% de l'intensité ECL originale après 40 minutes, contre 25% pour un complexe adsorbé sur silice. Par conséquent, l'immobilisation covalente induit une plus grande stabilité du système pendant une période plus longue.

General introduction

Spectroelectrochemistry is a relatively new field of electroanalytical chemistry that combines the electrochemical techniques with spectroscopic output.[1] In conventional electrochemical measurement the output provided is the electrical current that results from oxidation or reduction of the species as well as charging effects coming from the capacitive properties of the electrode surface. By coupling it with spectroscopical method of choice, one can also measure the signal in desired wavelength range which gives an additional array of data. This can be crucial in studying the mechanism of the reaction[2] or providing another mode of analytical detection.[3] The most cost-efficient way of realizing such combination is coupling with UV-Vis spectrometer which is a commonly used tool for sensing.[4] Another possible techniques which can give more detailed information of the studied system are Raman spectroscopy[5] and FT-IR.[6] From the electrochemical side, most of measurements are performed at constant potential but there are also reports of dynamic measurements were cyclic voltammetry was used and the spectroscopic signal was also measured in real time.[7]

In the literature one can find different experimental setups of this technique. In the first one the exciting beam does not go through the electrode, but instead is aligned to be parallel to it in close proximity.[8] For coupling with surface enhanced Raman spectroscopy (SERS) the beam is simply targeted at the electrode.[9] When there is a need for a beam to go through the electrode, one can use grid electrodes that have empty spaces to allow the light to go through[10] or transparent electrodes.[11]

Another technique that operates on a similar principle as spectroelectrochemical measurements is electrochemiluminescence generation. Here, because of the electrochemical input a light is generated which can be measured and quantified. Photon emission can be correlated with the concentration of the analyte in the solution and therefore this method has found many analytical applications, including commercial ones.[12]

Because of the rising interest in spectroelectrochemical techniques, researchers have looked for ways of enhancing the detection signals to improve the reliability and applicability. One of those ways is to employ porous electrodes like it is being done in electrochemistry. Higher surface area that those electrodes possess gives higher detection currents, better sensitivity and lower limits of detection. However, as mentioned before, many setups use the beam passing through the electrode as it is the only way to measure the changes happening directly on the electrode and not only in the vicinity. Therefore there has been an ongoing inquiry into

the possibility of using transparent and porous electrodes as it would improve the electrochemical side of the experiment to also enhance the spectral response. For this reason transparent conductive oxides (TCOs) are heavily investigated in the literature for the purpose of forming a transparent, porous and conductive layer that could be such an electrode.[13] There exists a number of methods of deposition for such materials, like random nanoparticle agglomerates[14], templated deposition[15], physical methods[16], electrospinning[17] and top-down methods.[18] There is a big variety in obtainable morphologies and pore sizes that can accommodate different needs.

One method of developing the surface area of the electrodes is the deposition of mesostructured silica layers through electrochemically-assisted deposition.[19] Such layers can be easily deposited on TCO electrodes. Their porosity ensures good mass transfer throughout the film. They are also negatively charged which can help in preconcentration of positively charged anions.

For the purpose of this thesis project an electrospinning protocol was chosen as it can produce macroporous layers that can be later additionally functionalized with additional mesostructured layer like silica. The technique requires preparation of a viscous solution containing precursors to which a high voltage is applied to promote the fiber deposition on the grounded collector. Electrodes were prepared in the form of a free-standing mat or immobilized on a solid substrate and tested in various electrochemical and spectroelectrochemical tests like ascorbic acid or methylene blue detection. The possibility of improving the electrochemiluminescence generation was also explored. Characterization of the layers was also performed by X-ray diffractometry, scanning electron microscopy and profilometry.

Introduction générale

La spectro-électrochimie est un domaine relativement nouveau de la chimie électro-analytique qui combine les techniques électrochimiques et un signal spectroscopique.[1] Dans la mesure électrochimique classique, le signal de sortie fourni est le courant électrique résultant de l'oxydation ou de la réduction des espèces chimiques ainsi que des effets de charge provenant des propriétés capacitives de la surface de l'électrode. En la couplant avec une méthode spectroscopique de choix, il est également possible de mesurer le signal dans une gamme de longueurs d'onde souhaitée, donnant une source supplémentaire d'informations. Cet aspect peut être crucial pour l'étude du mécanisme d'une réaction[2] ou pour fournir un autre mode de détection analytique.[3] Le moyen le plus rentable de réaliser une telle combinaison est le couplage avec un spectromètre UV-Vis qui est un outil couramment utilisé en chimie analytique.[4] Les autres techniques d'analyse spectroscopique permettant d'obtenir une information détaillée sur la nature du système étudié sont les spectroscopies vibrationnelles Raman[5] et FT-IR.[6] Du côté électrochimique, la plupart des mesures sont effectuées à un potentiel constant, cependant il est également possible de réaliser des mesures dynamiques. Du côté électrochimique, la plupart des mesures sont effectuées à un potentiel constant, cependant il est également possible de réaliser des mesures dynamiques. Par exemple la voltammétrie cyclique peut être utilisée et le signal spectroscopique mesuré en temps réel.[7]

Dans la littérature, différentes configurations expérimentales de cette technique ont été décrites. Par exemple, le faisceau d'excitation peut être aligné parallèlement à l'électrode, pour se retrouver à proximité étroite de celle-ci.[8] Pour le couplage avec la spectroscopie Raman exaltée de surface (SERS), le faisceau est simplement pointé sur l'électrode.[9] Quand il y a besoin que le faisceau passe à travers l'électrode, il est possible d'utiliser des électrodes sous forme de grille présentant des espaces vides pour permettre à la lumière de passer[10] ou des électrodes transparentes.[11]

Une autre technique qui, dans le principe, ressemble aux mesures spectro-électrochimiques est la génération d'électrochimiluminescence. Dans ce cas, un phénomène électrochimique, induit la génération de lumière (mesurable et quantifiable). L'émission de photons est corrélable avec la concentration de l'analyte dans la solution. Par conséquent, cette méthode trouve de nombreuses applications analytiques, y compris des applications industrielles.[12]

En raison de l'intérêt croissant pour les techniques spectro-électrochimiques, les chercheurs s'intéressent aux moyens d'améliorer les signaux de détection afin d'augmenter la fiabilité et

l'applicabilité de ces techniques. L'une des solutions consiste à utiliser des électrodes poreuses. L'importante surface spécifique que possède ce type d'électrodes donne des courants de détection plus élevés, une meilleure sensibilité et des limites de détection plus basses. Cependant, comme mentionné précédemment, beaucoup de configurations utilisent un faisceau passant à travers l'électrode comme c'est le seul moyen de mesurer les changements se produisant directement sur l'électrode et non seulement dans son voisinage. Dans ce contexte il apparait que les études portant sur l'utilisation d'électrodes transparentes et poreuses sont d'actualité. En effet, leur utilisation améliorerait à la fois l'aspect électrochimique de l'expérience et la réponse spectroscopique. Pour cette raison, les oxydes conducteurs transparents (transparent conductive oxide, TCO) sont fortement étudiés dans la littérature afin de former une couche transparente, poreuse et conductrice.[13] Il existe un certain nombre de méthodes de dépôt pour de tels matériaux TCO, comme la formation d'agglomérats de nanoparticules[14], les dépôts à partir de modèles[15], les méthodes physiques[16], l'électrofilage[17] et des approches technologiques descendantes (top-down).[18] Il existe une grande variété de morphologies et de tailles de pores pouvant être obtenues afin de répondre aux différents besoins.

Une manière d'augmenter la surface spécifique des électrodes est le dépôt de couches mésoporeuses de silice par dépôt assisté électrochimiquement.[19] De telles couches ont une surface spécifique élevée et peuvent être facilement déposées sur des électrodes TCO. Leurs canaux perpendiculaires à la surface de l'électrode assurent un bon transfert de masse dans tout le film. Ils sont également chargés négativement ce qui peut aider à la préconcentration des anions chargés positivement.

Pour mener à bien ce projet de thèse, un protocole d'électrofilage a été choisi car il permet la production de couches macroporeuses pouvant être fonctionnalisées dans un second temps par un autre matériau, comme par exemple une couche mésoporeuse de silice. Cette technique nécessite la préparation d'une solution visqueuse, contenant les précurseurs, soumise à une différence de tension pour favoriser le dépôt de fibres sur le collecteur connecté à la terre. Les électrodes ainsi préparées sont soit obtenues sous forme d'un film auto-supporté, soit immobilisées sur un substrat solide. Elles ont été testées pour la détection électrochimique et spectroélectrochimique de différentes molécules, comme celles de l'acide ascorbique ou du bleu de méthylène. La possibilité d'améliorer la génération d'électrochimiluminescence a également été explorée. La caractérisation des différents dépôts d'électrofilage a été aussi réalisée par diffraction des rayons X, microscopie électronique à balayage et profilométrie.

Chapter 1. Literature survey of transparent and porous electrodes and their applications

1.1 Introduction

Optically transparent electrodes (OTEs) have become one of the most interesting research areas in recent years. They have found many applications in touch-screens[20], light-emitting diodes[21], dye-sensitized solar cells (DSSCs)[22], spectroelectrochemistry[2] and spectroelectroanalysis.[1] To improve the capabilities of those electrodes, scientists have started to look for ways to change the morphology and developing the surface for various application needs. From that, a new direction of research has originated – transparent and porous electrodes and resulted in the emergence of many methods of deposition yielding various porous structures like nanoparticle deposition, templated deposition, physical methods, top-down methods or electrospinning (Figure 1.1). It has been postulated before that one could enhance light-harvesting capabilities in DSSCs, by using a transparent electrode with
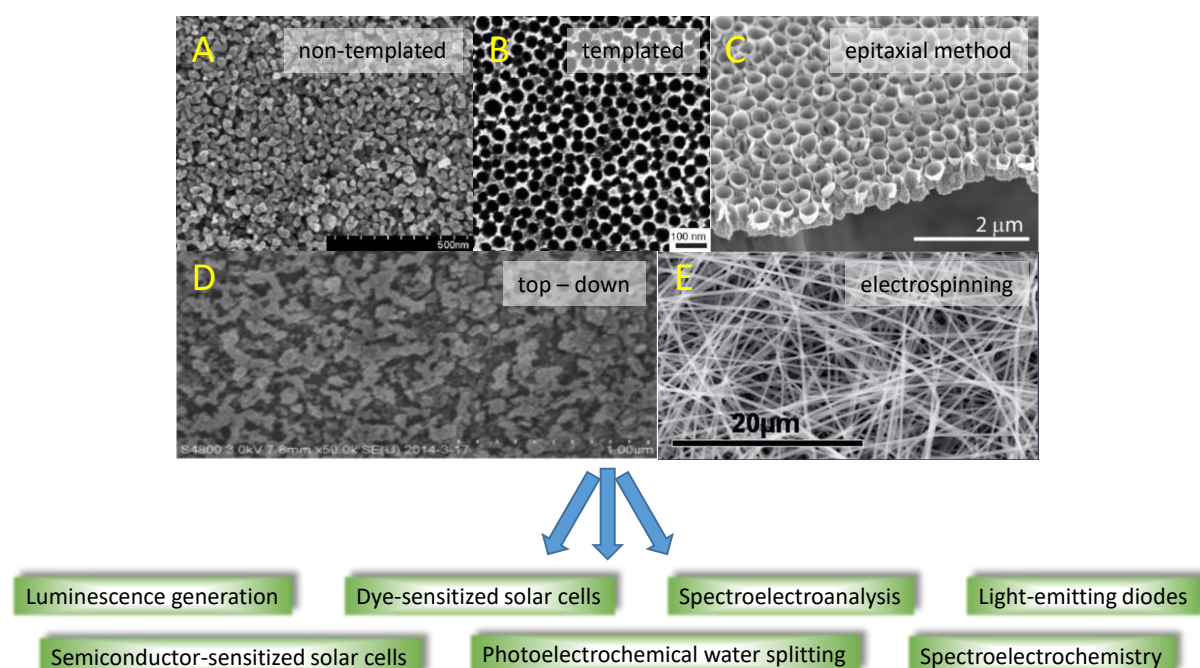
Figure 1.1. Presentation of different types of methods for depositing transparent and porous ITO (A) ITO nanoparticle layer deposited by doctor-blade and annealed in 750°C[23], (B) templated mesoporous ITO deposited using nanocrystals[24], (C) macroporous ITO formed by shadow evaporation at 45°[25], (D) ITO layer made by anodization at 10 V[26], (E) macroporous ITO nanofibers deposited by electrospinning[27], as well as proposed applications.

higher surface area because it would reduce the hole-electron pair recombination through minimizing the path that photogenerated electron has to travel before reaching a conductive charge collector.[28] Furthermore, combining the ability of passing the light through an electrode of high electroactive surface area could prove useful in photo-assisted electrochemical experiments[29] or enhancing a spectroscopic response by increased load of immobilized electrochromic species.[30] First attempts to fabricate such an electrode utilized a semiconductor, in most cases it was tin oxide. It has been tested in DSSCs[31] as well as spectroelectrochemical study of proteins.[4] But with the rise of a new class of materials – transparent conductive oxides (TCOs) new possibilities have been opened as TCOs offer a conductivity only one or two orders of magnitude lower than commonly used metal electrodes[32] while remaining optically transparent. Moreover, new carbon-based composites are also entering the fray as an alternative to inorganic materials.[21] This literature survey will go over porous and transparent metal oxide electrode materials with proven electrochemical capabilities and transparency and it will include their preparation methods. Additionally, the proposed applications that benefit from higher electroactive surface area and high transparency will be presented with the goal to highlight the interest of using porous TCOs in combined spectroscopic and electrochemical analysis.

1.2. Preparation methods of the porous transparent conductive oxides

So far, the most commonly used TCO is indium tin oxide (In_2O_3:Sn, ITO) and it has found many commercial applications like touch-screens and liquid crystal displays thanks to its superior conductivity and optical transparency over the competitors.[33] Its main drawback is an elevated cost and a low availability of metallic indium. However, it lacks UV transparency as most of TCOs. Cheaper alternatives are doped tin oxides like antimony tin oxide (SnO_2:Sb, ATO) or fluorine tin oxide (SnO_2:F, FTO)[33] but their drawback are worse conductivity and transparency. Another emerging material is niobium tin oxide (SnO_2:Nb, NTO).[34] Finally, aluminum and boron doped zinc oxides (ZnO_2:Al, AZO and ZnO_2:B, BZO respectively)[35,36] are the other alternatives. A list presenting developed porous TCO electrodes along with their most important parameters (such as pore size and conductivity) is presented in Table 1.1.

1.2.1. Non-templated particle deposition

One of the first methods of deposition of porous TCO was done by Goebbert *et al.* in which they have prepared colloidal suspensions of ITO and ATO nanopowders that were later deposited by dip coating.[14] Later on, the deposits were calcined at high temperature in order
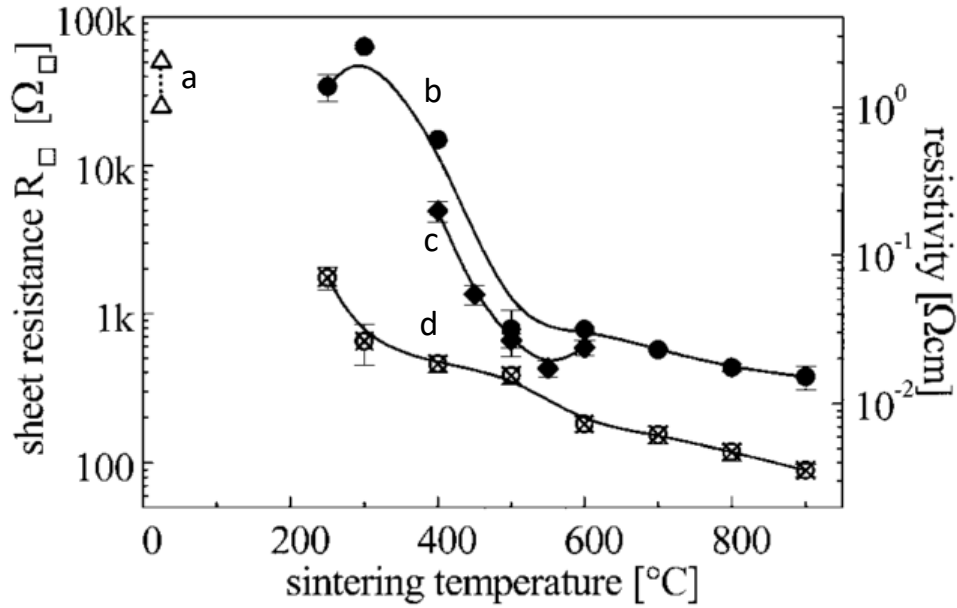
Figure 1.2. *Resistivity parameters as a function of sintering temperature of 400 nm thick layers of (a) ITO deposited at room temperature and cured under UV, (b) as deposited ITO, (c) as deposited ATO, (d) ITO additionally treated in nitrogen in 300°C.*[14]

to evaluate their resistivity and it was found that ITO and ATO films have reached resistivity of $3.4*10^{-3}$ Ω cm and $2*10^{-2}$ Ω cm respectively (Figure 1.2). Similar method was chosen by Niedziolka *et al.* that involved the deposition of ITO nanoparticles by dip coating to increase the electroactive surface area of an ITO electrode in a controlled manner by more than one order of magnitude while keeping the sample optically transparent.[37] No heat treatment was necessary to achieve the effect but the method required a conductive substrate. Another approach was chosen by Ederth *et al.* where a dispersion consisting of ITO nanoparticles (ca. 16 nm in diameter) was spin-coated over a chosen substrate and calcined. The electrodes composed of randomly packed agglomerates were mesoporous (2-50 nm, filling factor of ITO phase 0.3-0.4) and the films remained conductive and optically transparent, even at a thickness of 1 μm.[38] Several other studies regarding properties and optimization of similarly deposited layers of ITO from ethanolic solutions have followed. It was found that porous ITO electrodes could achieve as much as 140-fold higher roughness than flat electrode measured by redox current density of adsorbed ruthenium complex owing to increased active surface area.[39] It was also used to deposit a conductive anti-reflective coating.[40]

Spin-coating method was also studied by Liu *et al.* for deposition of ATO porous and transparent films to establish the relationship between conductivity and doping level and it

was found that a resistivity of $5.2*10^{-1}$ Ω cm could have been achieved while increasing the doping up to 20 % doping with 300 nm pore size. However, at the same time the transparency went down from 80 % (for undoped SbO_2) to around 61% (in 300 – 800 nm range, Figure 1.3).[41] Bubenhofer *et al.* have also studied similar films and their interactions with various non-conductive coatings to simulate a resistance increase with environmentally-sourced impurities.[42] A simple protocol of casting the ATO nanoparticle dispersion was developed by Guo *et al.* to study the electron transfer in such porous layers.[43] Similar procedure involving drop-coating of ITO nanoparticle suspension on flat ITO plates was developed by Kato *et al.* and resulted in a mesoporous ITO electrode with sheet resistance of 8.4 kΩ sq^{-1} after annealing in 450 °C, with a thickness of ca. 3 μm, and a pore diameter up to 100 nm.[29,44] In another report, drop-coated nanoparticle electrode was found to have specific capacitance of 3 F m^{-2} compared to just 0.14 F m^{-2} for planar unmodified ITO.[45] Finally, a protocol of spin-coating of AZO nanorods was also reported.[46]
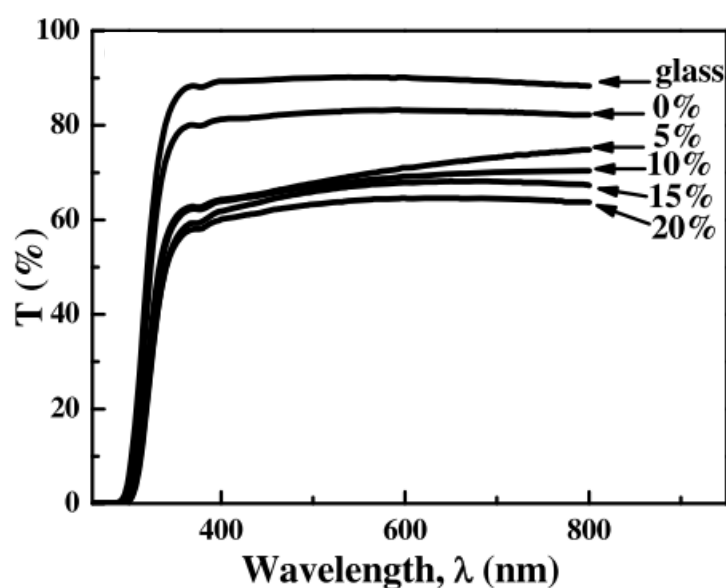
Figure 1.3. Transmittance of the ATO layers with different level of Sb doping.[41]

Furthermore, a number of similar in principle methods involving doctor-blade deposition of ITO has been devised.[47–49] FTO porous transparent electrode has been also deposited by Yang *et al.* by doctor-blading FTO nanoparticles. The electrodes were then functionalized in a standard procedure with TiO_2 for application in DSSC.[50] Gross *et al.* have studied this method of ITO nanoparticle deposition using different annealing time and temperature and the sheet resistance could be lowered to achieve 50 Ω sq^{-1} after treatment at 1000 °C.[23] Detailed study

on photoinduced interfacial electron transfer has been reported with similar porous and transparent films.[51]

Finally, it is worth mentioning a composite ITO-TiO$_2$ porous electrode prepared by spin coating of mixture of two types of respective nanoparticles with which a significant increase in response time of electrochromic device (around two times faster) could be achieved compared to solely transparent electrodes through screen-printing from ITO nanoparticle paste.[52]

Main characteristic of almost all of the listed non-templated nanoparticle-based deposition methods is that they yield a layer that is mesoporous (2-50 nm pore size) and non-ordered. The active surface area size depends on the dimensions of the nanoparticles and the degree of their agglomeration in prepared paste or dispersion. Besides those methods that yield mesoporous films, another interesting method was presented by Forman *et al.* that relies on using much larger ITO particles, of around 44 μm in diameter. Because of that the resulting layer was macroporous and transparent with roughness factor reaching 95. Spray deposition was employed to produce the electrodes.[53]

1.2.2. Templated deposition

It was quickly realized that structures using simple deposition of nanoparticles yield rather chaotic and unorganized deposits that could not reach their full potential. The surface area and the access to each pore could be improved by obtaining a more organized structure. Therefore, a new approach for the preparation of the porous electrodes composed of TCOs has been targeted through the employment of templating methods that allow to control the porosity and achieve ordered structure. Usually the first step of deposition was a sol-gel deposition by dip coating, spin-coating or drop-coating from a mixture of precursor salts and a template. Afterwards, in virtually all cases, heating must be employed to sinter the material, converting the deposit into a highly conductive doped oxide, and to remove the template. The major obstacle to this was an issue of preserving the structure through the heating. Indeed, a crystalline material like ITO or other TCOs could easily recrystallize during the calcination process resulting in the collapse of the porous structure. The first example of successful deposition of mesoporous TCO by templating was presented by Pohl and Dunn where deposition of mesoporous ITO was made possible through spin coating from inorganic salt precursors and cetyltrimethylammonium bromide (CTAB) as template. Successful achievement of the structure was confirmed by XRD studies, but no proof of conductivity was

shown.[54] Similar approach was used by Zhang *et al.* to achieve pore size in the range of 2-2.5 nm (depending on Sn doping level) and surface area in the range of 280-340 m^{2}g^{-1}. Best level of Sn doping was found to be 10 mol % with a resistivity of 1.2*10^{-2} Ω cm and a transparency higher than 80 % (in 500 – 800 nm wavelength range). Slow heating rate was found instrumental for the safe removal of the template.[55]

In later studies, CTAB has been replaced as template in favor of block copolymers. First example of this shift is the publication by Fattakhova-Rohlfing *et al.* in which a mesoporous ITO layer was templated by poly(ethylene-co-butylene)-b-poly(ethylene oxide) diblock copolymer (also known as KLE) and deposited by dip-coating using organic salt as indium precursor. Figure 1.4 presents tunneling electron microscopy images of the obtained layers, in a direction perpendicular or parallel to the substrate, and a high-resolution image showing lattice planes. Thanks to the higher surface area created by the template a much higher
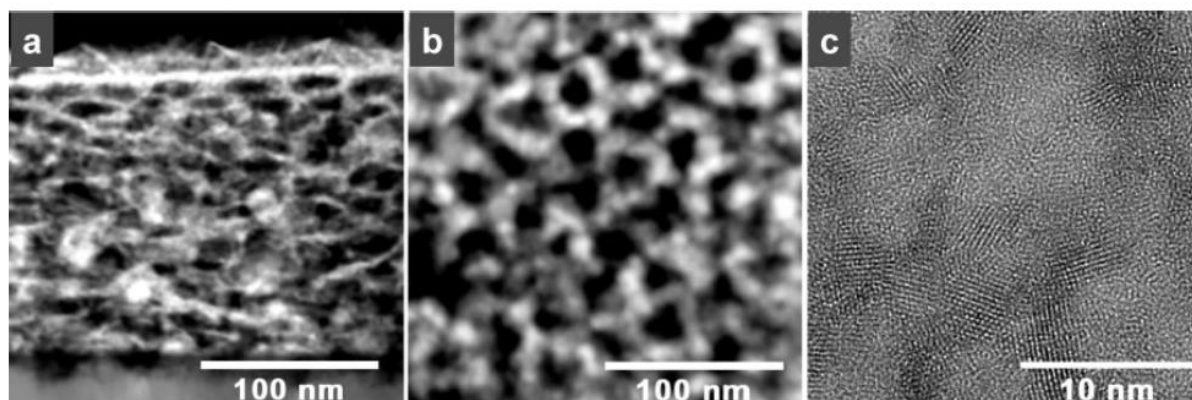
Figure 1.4. Images of mesoporous ITO at 450°C in air and nitrogen for 10 min captured by scanning electron microscopy in high-angle annular dark-field contrast (a) perpendicular and (b) parallel to the substrate plane and (c) by high-resolution transmission electron microcopy of a 20 nm wide section.[15]

loading of the dye – Eosin Y has been achieved on the porous electrode than on the flat one which was confirmed both by electrochemistry and UV-Vis spectrometry.[15,56,57] Furthermore, two other studies have focused on optimizing the deposition procedure. In the first one, Graberg *et al.* shown that a templating polymer of smaller molecular weight might be advantageous in order to increase the loading of electrochromic probe like Prussian blue, as the resulting pores are smaller and the surface area is bigger. However, the higher surface area came at a price of higher specific resistance of this film compared to films templated with bigger molecule.[58] In the second publication, a method for multilayered films is presented to achieve even higher surface area and grafting density of ruthenium complex used for

photocurrent generation.[59] Both studies also point out the importance of additional heat treatment under reducing atmosphere to improve electrical properties of mesoporous ITO. Later, it was found out by Wang *et al.* that a similar procedure could be applied to the deposition of transparent and mesoporous ATO films with a conductivity only one order of magnitude lower than compact films (by templating with KLE or polyisobutylene-b-poly(ethylene oxide) (in short PIB-PEO)).[60] Another type of triblock copolymer Poly(ethylene glycol)-b-poly(propylene glycol)-b-poly(ethylene glycol) (in short F127) was employed by Hou *et al.* as template for mesoporous ATO. It was found that the roughness factor (RF) measured from their electrochemical response was around 250 which was 3-times more than previously reported electrodes consisting of randomly deposited nanoparticles.[61] The material had elliptical pores with dimensions around 12.5 nm along the major axis and 5.6 nm along the minor axis and it had a surface area of 83 m^2g^{-1}. F127 has also been successfully used for templating of AZO and BZO by Ueno *et al.* A mixture of the block copolymer, zinc acetate and appropriate doping source (aluminum nitrate or boric acid) was spin coated and later calcined, achieving mesoporous films.[62] Another example of triblock copolymer was sulfonated HmSEBmS which was used for the deposition of mesoporous ATO.[63] Furthermore, an interesting approach was proposed by Aksu *et al.* where a special metalorganic precursor containing both indium and tin atoms has been prepared and deposited by dip coating together with three different block copolymer templates (KLE, F127, Brij700) and depending on which has been used, different surface area (44 – 200 m^2g^{-1}) and resistivity (0.64 – 1.73*10^{-2} Ω cm) could be achieved.[64] Finally, a method of preparation of mesoporous ATO particles has been developed by Volosin *et al.* that involved in-situ combination of sol-gel deposition of the oxide with subsequent polymerization of the monomeric templates – resorcinol and formaldehyde to avoid the structure collapse during calcination.[65] The porosity of the obtained particles was tuned to achieve a surface area ranging from 35 to 100 m^2*g^{-1} with an average pore size ranging from 7 to 33 nm. Those particles were later deposited to form a transparent and porous film.[66–68]

Muller *et al.* were the first to show that it was possible to obtain porous TCO layers from preformed nanocrystals instead of using salt precursor. The final porous film had a better cristallinity, Moreover, more popular F127 could have been used to achieve a high degree of order instead of less available KLE copolymers. Here, mesoporous ATO was prepared to host electroactive guest in order to estimate the active surface area which was found to be up to 50 times bigger than that of a flat electrode as portrayed on Figure 1.5. It is also noticeable that

increasing the calcination temperature improved the conductivity and that increasing the surface results in higher capacitance currents. Pore sizes ranged from 6 to 8 nm.[13,69] A similar concept was applied to mesoporous ITO.[70] Buonsanti *et al*. have shown that the pore size in ITO films prepared from nanocrystals could be controlled in a range between 23 and 34 nm by use of differently sized PDMA-b-PS templates.[24] More recently, it was found that the pore size in porous ATO layers could be adjusted between 10 and 80 nm not by the size of the template, which was poly(ethylene oxide-b-hexyl acrylate) (PEO-b-PHA) but by manipulating the sizes of the micelles it produced in the precursor solution with HCl content.[71]
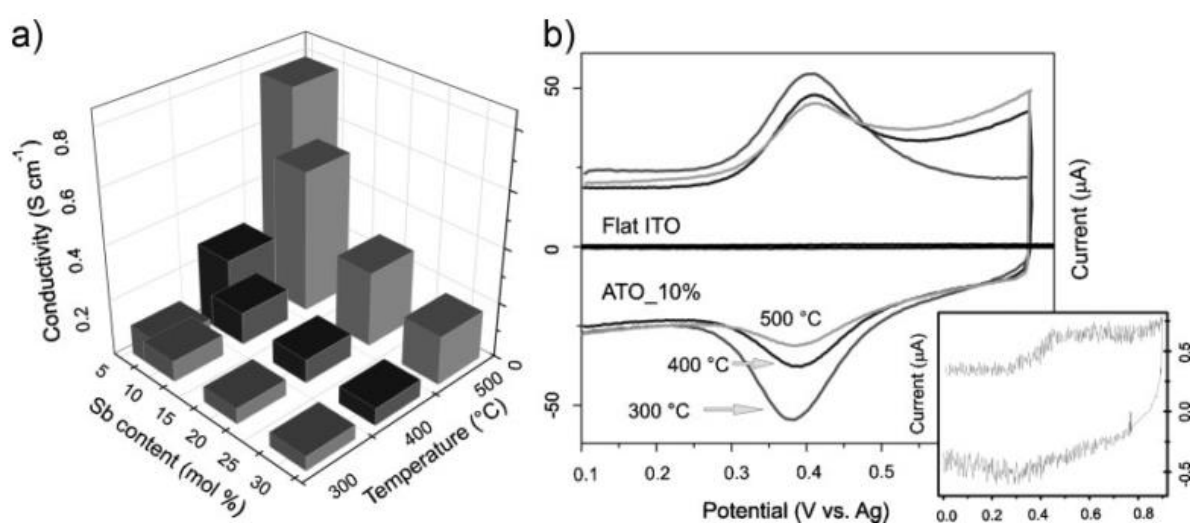
Figure 1.5. (a) Dependence of conductivity on Sb doping level and calcination temperature of mesoporous ATO films. (b) Cyclic voltammograms of ferrocenecarboxylic acid that was covalently attached to the electrode surface of layers calcined in 300, 400 and 500 °C as well as on flat ITO (also on the inset). Average thickness of the film was 210 nm, scan speed for cyclic voltammetry was 50 mv s^{-1}.[69]

The methods that we described previously focus on using a molecular template. In consequence, the transparent films prepared in that way were mostly mesoporous (2-50 nm). Their clear advantage is a higher surface area available for molecule immobilization or surface reactions. Their drawback is a more difficult mass transfer in the volume of the electrode. That statement prompted researchers to find a way to use bigger templates in order to achieve macroporosity. The first templated macroporous transparent electrode can be attributed to Wang *et al*. They deposited ITO by electrophoresis in a porous (100 or 200 nm diameter) polycarbonate (PC) membrane.[72] Resulting nanowires had lengths up to 25 μm and

16

diameters respective to the pore size of the membrane that was later burned off. The disadvantages of this method are the requirement of a conductive substrate for electrophoresis and the lack of interconnections between the nanowires. Later on, the introductions of beads (polymer or silica) as templates have brought a new TCO architecture of interconnected ordered macroporous layers. The first ones to achieve this were Arsenault *et al.* who used silica spheres in order to obtain a macroporous ATO film (Figure 1.6). This technique involved infiltration of a deposited bead layer with preformed nanocrystals followed by the infiltration of the precursor sol. These two steps allowed reaching a high conductivity.[73] Another similar method was developed with polystyrene beads as template. A solution of prepared FTO precursors was used to infiltrate the structure of the opal matrix and, after calcination and template removal, a macroporous (pore size ~200 nm) ordered FTO film was obtained.[74,75]
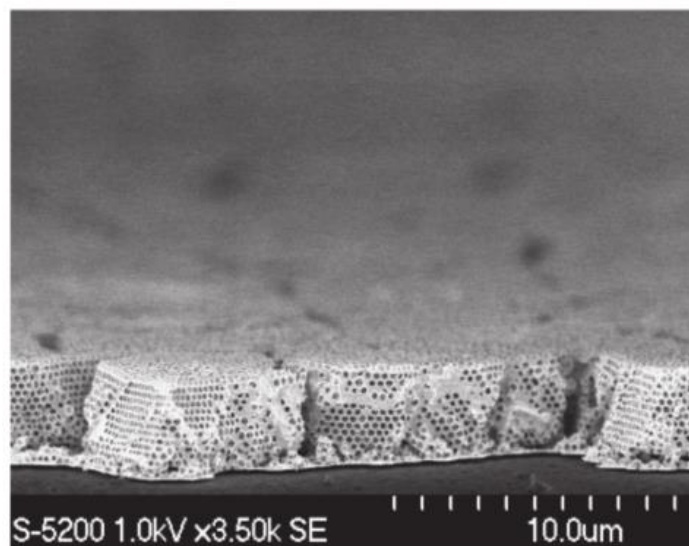
Figure 1.6. Scanning electron microscopy image periodic macroporous ATO layer.[73]

Enhanced electrochemical properties compared to flat electrodes were reported while the transparency (~50 %) remained satisfactory for potential applications. Polystyrene opal beads (550 nm diameter) were also used as template by Moir *et al.* to produce macroporous and ordered ATO layers from nanocrystals. Such architecture allowed for increasing the active surface area (measured by capacitance) by more than two orders of magnitude while maintaining transmittance above 60 % in 400-800 nm range.[76] Another contribution has shown the advantage of using preformed nanocrystals over standard solution of salt precursors in obtaining templated macroporous structures.[77] Here, PMMA beads (100 and 370 nm diameter) were used for the deposition of ITO and the structure obtained in the former

case (100 nm) was much more ordered than the latter (370 nm). But more importantly, a high transparency was maintained despite the development of the surface that allowed for enhanced surface coverage with cytochrome *c*, 7 to 10 times higher than the theoretical coverage of a monolayer on a flat surface. Later, macroporous ATO was also reported using similar procedure.[78] Interesting approach has been presented by Mersch *et al.* where the natural ability of big ITO nanoparticles (< 50 nm diameter) to form mesoporous layers by dip-coating was combined with templating by large PS beads with diameter of 750 nm. The resulting structure was claimed to have both macro- and mesoporosity[79] and was later replicated in different reports.[80,81]

1.2.3. Physical deposition methods

Physical deposition methods have been extensively investigated as a way to deposit porous TCO films because of innate advantages, like the relative simplicity of the protocol and high reproducibility owing to tight control. Their main drawback is the cost of the specialized equipment that is required. One of the first methods used by Naghavi *et al.* was the pulsed laser deposition which could be used to deposit disordered mesoporous ATO with electrochromic properties.[82] The same method was applied for the deposition of AZO[83–85] and ITO films.[86] It was also found that the morphology could be adjusted to obtain different levels of porosity by manipulating the pressure in the chamber (Figure 1.7). The ratio between the amount of adsorbed dye and the amount of dye that can be detected electrochemically was determined with films prepared in different conditions. Almost 80 % of the dye was detectable by electrochemistry when the layer was deposited at the pressure of 200 mTorr. The most popular physical deposition method is vapor deposition which could be realized in different configurations. Joanni *et al.* reported first protocol that involved radio frequency (RF) sputtering of ITO which yielded a structure of branching nanowires.[87] RF sputtering also proved to be useful in deposition of flexible layers of ITO with small degree of porosity achieved by pretreatment of the polymer substrate. The layers were transparent with sheet resistance of 230 Ω sq^{-1}.[88,89] AZO films with small levels of porosity were also successfully deposited using RF sputtering.[90] Regular physical vapor deposition of ITO resulted in a simple nanowire morphology as shown by Noh *et al.* with the aim to challenge the major problem of solar cells that is charge recombination. It was observed that the 3D architecture lowered the charge collection time significantly by 4 to 10 times (depending on the current density) compared to a planar electrode.[91] Similar ITO nanowire electrode was also reported with an average wire length of 12 μm.[92]
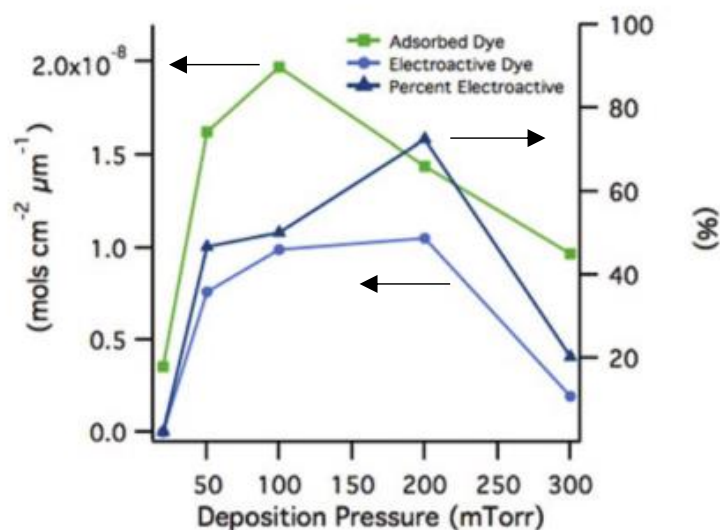
Figure 1.7. *Dye loading (Ru-C) and its electroactive fraction on PLD-deposited porous ITO vs deposition pressure measured by desorption and cyclic voltammetry.*[86]

A considerable improvement was then achieved by applying oblique or glancing angle (GLAD) techniques where the vapor flux is not perpendicular to the substrate but at an angle. Krause *et al.* reported one of the first protocols for the deposition of mesoporous ITO electrode deposited by GLAD (Figure 1.8 presents different film thicknesses), achieving surface area of ~50 m^2 g^{-1}, i.e. 200 times more than a planar film. [93–96] Number of studies have also shown the possibility of tuning the properties of GLAD-deposited ITO[97] to suit different needs like thin film solar cells[16], enhanced chemisorption[98] or improvement of light extraction at targeted wavelength.[99] As shown by Dickey *et al.* it is also possible in physical vapor deposition to achieve nanotubular morphology sheet resistance of ~259 Ω sq^{-1} by using a porous template like anodized aluminum oxide.[25] Similar in principle but using different precursors, the method of metaloorganic chemical vapor deposition was used to deposit ITO in the cavities of porous glass, resulting in film with resistivity between 10^{-1} and 10^{-2} Ω cm and a surface area of 79 m^2 g^{-1} but with only 30 % transmittance at 550 nm.[100] Moreover, the use of 2.2 μm PS macroparticles template was applied to produce macroporous SnO_2 and AZO films by atomic layer deposition (ALD).[101] Later on, similar concept using beads with 350 nm diameter, was applied for the deposition of porous ITO.[102] ALD was also used to deposit NTO (niobium-doped tin oxide) on porous TiO_2.[103] Chemical vapor deposition has also been successfully used to deposit a layer on pre-drilled quartz substrates to form a

macroporous FTO layer.[104] Finally, a method for spray pyrolysis deposition of AZO was developed and it was found that lowest resistivity of $0.56*10^{-3}$ Ω cm was achieved at 1.5 % of Al doping.[105]
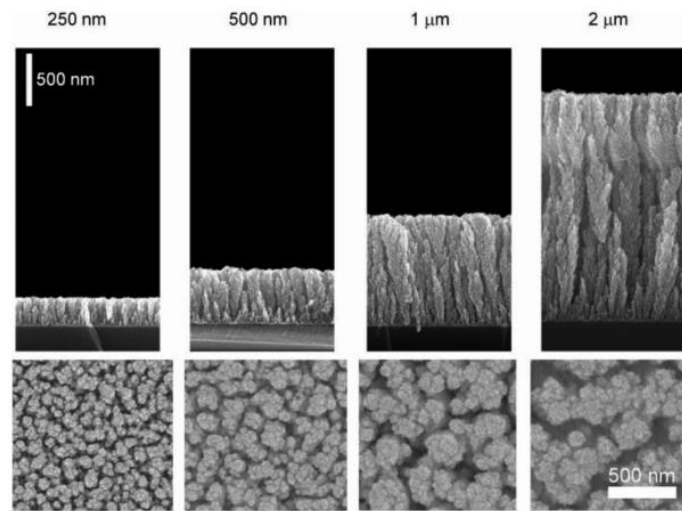
Figure 1.8. Side- and top-view SEM images of ITO films of differing thickness deposited by glancing angle deposition at 80°.[95]

1.2.4. Top-down methods

Another subsection of fabrication of porous TCOs includes top-down methods that may provide an interesting alternative to dominantly reported bottom-up protocols. Here, the starting point is a flat film of a TCO (often commercially available). Kang *et al.* have developed a method of introducing porosity to flat ITO films by etching in acid.[18] On Figure 1.9 the samples etched for increasing amount of time are portrayed. It was found that the longer process endured the bigger was the drop in transparency and conductivity of the layer, but the higher surface area has enabled to achieve higher light intensity in the prepared LED. An approach that is similar in principle has been used by Lee *et al.* An electrochemical treatment in acid resulted in anodization and subsequent formation of the porous layer. [26,106] Finally, FTO with developed surface was prepared by patterning and reactive ion etching.[107]
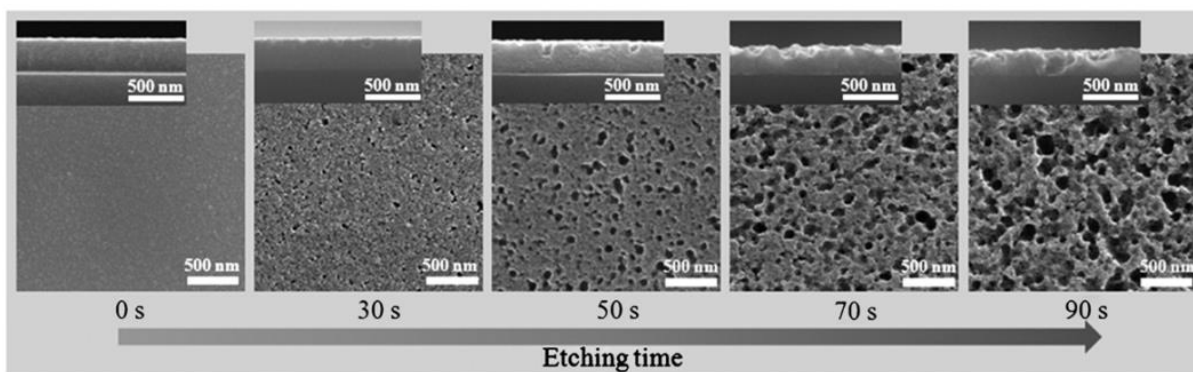
Figure 1.9. Top-view SEM images of etching process of ITO film and the pore formation including the cross-section view in the respective insets.[18]

1.2.5. Electrospinning

In recent decade an increasing amount of attention was put into electrospinning of TCOs, as a quick way of depositing macroporous and transparent layers of ITO[108–111] and ATO.[112,113] The technique relies on forming very thin fibers thanks to applying a strong electric field to a viscous polymer solution. In order to deposit a TCO fiber layer, a precursor must be added the solution usually a mixture of salts of the desired metals. The electrospun layers are highly macroporous and it was found that, in contrast to regular flat ITO electrodes, the maximum conductivity of the electrospun layer is achieved at Sn doping level of around 12.5%.[114] The first example of a truly conductive, porous and transparent electrospun layer was presented by Wu *et al.* achieving sheet resistance of only 550 Ω sq^{-1} with 80 % transparency (at 550 nm).[115] The procedure could be optimized for better transparency but at the cost of a higher sheet resistance (Figure 1.10). Better sheet resistance of 400 Ω sq^{-1} for ATO was obtained by depositing porous layers in the form of free-standing mats and using ATO nanoparticles as precursors.[17] Similarly AZO nanofibers have been prepared and it was found that the grain size becomes lower with rising Al doping levels.[116] Since then several publications on macroporous electrospun ITO has been published.[27,117]
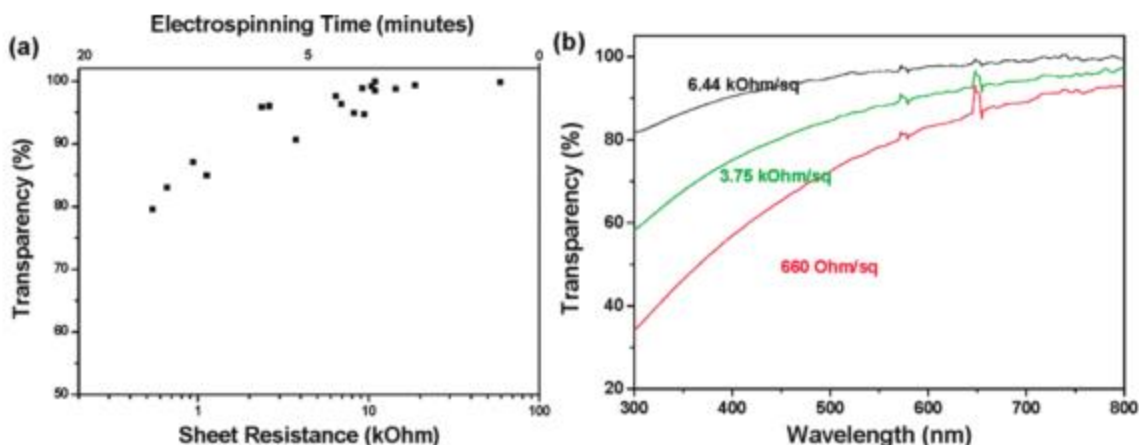
Figure 1.10. (a) Transmittance at 550 nm vs sheet resistance and electrospinning time for ITO nanofibers. (b) Transmittance in UV-Vis range for electrospun ITO of different sheet resistance.[115]

1.3. Applications of the porous transparent conductive oxides

In this part, the applications of porous and transparent metal oxide electrodes will be summarized. Because of growing needs for environmentally friendly energy sources most of existing applications are in photovoltaics and photoelectrochemical water splitting. Nevertheless, from those numerous works revolving around photocurrent generation one can draw important trends and conclusions for further applications in electroanalysis combined with spectroscopic analysis.

1.3.1. Energy generation and storage (photovoltaics, water splitting)

Photovoltaics became an important field for the development of transparent and porous electrodes as there is an intense ongoing research for efficient ways of utilizing sunlight as power source to reduce the reliance on fossil fuels due to climate and economic issues. Most popular realization of this idea are dye-sensitized solar cells (DSSCs). A work by Chappel *et al.* could be considered as a precursor in the field where SnO_2 mesoporous electrode was used as a base for the preparation of a DSSC with photocurrent conversion efficiency (PCE) reaching 1.125 %.[31] First application of TCOs came in 2007 with the report from Joanni *et al.* with branched ITO nanowires that were generating current density of 0.066 mA cm^{-1} and open circuit voltage (OCV) at 523 mV at illumination of 100 mW cm^{-1}. However, the PCE was only 0.15%.[87] Since then, a number of DSSCs based on porous electrodes were developed.[46,49,52,72,105,107,117] Most notable examples are AZO macroporous films achieving 4.9 % PCE[101] or FTO-nanoparticle based electrode developed by Yang *et al.* reaching 4.6 % PCE,
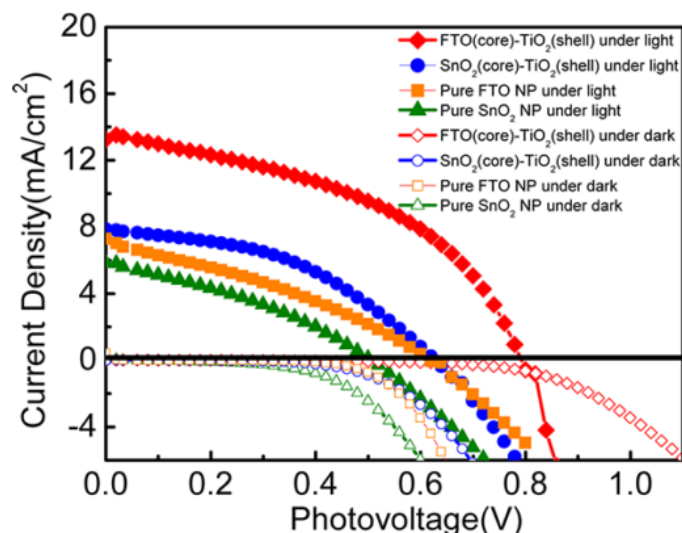
Figure 1.11. Current density vs voltage curves of different DSSCs based on FTO nanoparticles and undoped SnO2 nanoparticles, both with or without TiO2 shell. The measurements were done at 1.5 G illumination or under dark conditions.[50]

OCV at 760 mV and current density of 13 mA cm^{-2} under illumination of AM 1.5 G. In their research the importance of using more conductive, fluorine-doped tin oxide was highlighted (Figure 1.11).[50] In another example, ITO nanowires were shown to reduce the charge collection time 4 to 10 times over nanoparticle-based ones, achieving 3.8 % PCE.[91] Following the DSSCs in concept, semiconductor-sensitized solar cells have also been prepared[47,48] with highest achieved efficiency on porous electrodes of 1.66%[27] as well as organic solar cells with 6.74 % PCE.[89] Moreover, by simple dye sensitization of mesoporous ITO a photocurrent generation 150-fold higher than on flat electrode was made possible.[59] In another application an improvement of PCE of tandem solar cells from 12.27 % to 13.6 % based on GLAD-ITO was reported.[16] Finally, several biophotovoltaic applications have recently appeared. An electrode based on ATO nanoparticles was applied in generating photocurrents from deposited bacterial centers and was capable of generating 10 mA*cm^{-2} current density.[68] A different approach for generating photocurrents was demonstrated using deposited photosystem I on meso- and macroporous ATO.[71] It was found out that bigger pores are a better host for the protein, enhancing the generated currents 11-fold over planar electrode. Templated ITO electrode was also used to accommodate photosystem I protein, generating current density of 150 μA*cm^{-2}. [80]

Another application of porous electrodes in energy production is the photoelectrochemical water splitting. It shares the principle of capturing the solar energy with photovoltaics but

23

instead of electrical current the energy is transformed into the breaking of O-H bonds in water molecule and in some cases to generate hydrogen that could be later stored and used as a clean fuel. In 2012, the first application of mesoporous ITO in water splitting was shown by Kato *et al.* where Photosystem II (PSII) catalyzed oxygen generation from water, leading to a current density of 1.6 µA*cm^{-2} during a red light irradiation of 8 mW*cm^{-2}.[29] Later, it was found out that immobilization of PSII through covalent bond is also possible.[44] It is also feasible to couple the PSII-covered electrode with one electrode functionalized with a hydrogenase to achieve final light-to-hydrogen conversion efficiency of 5.4 %.[79] In the latest application of this electrode design, Os-based redox polymer (Figure 1.12) light-to-current efficiency of 6.9 % for oxygen evolution with turnover frequency (TOF) of 3.6 mol O$_2$*(mol PSII)$^{-1}$*s^{-1} with no mediator addition.[81] Two templated electrodes deposited by ALD were also used for water splitting after deposition of hematite. In the first one, NTO was used, reaching a current density of 2.35 mA cm^{-2} thanks to the host-guest architecture.[103] In the second, a porous ITO allowed for achieving 1.53 mA cm^{-2}.[102] Another approach involves drilled FTO electrodes. It has been applied in water photoelectrolysis to improve certain parameters of the reaction like lowering of the onset potential and improving the charge transfer.[104] Finally, ITO nanowire electrode has been applied in hydrogen generation and achieved 2.4-fold increase over planar TiO$_2$ system with current density of 16.2 mA cm^{-2} at 1.0 V$_{RHE}$.[92]
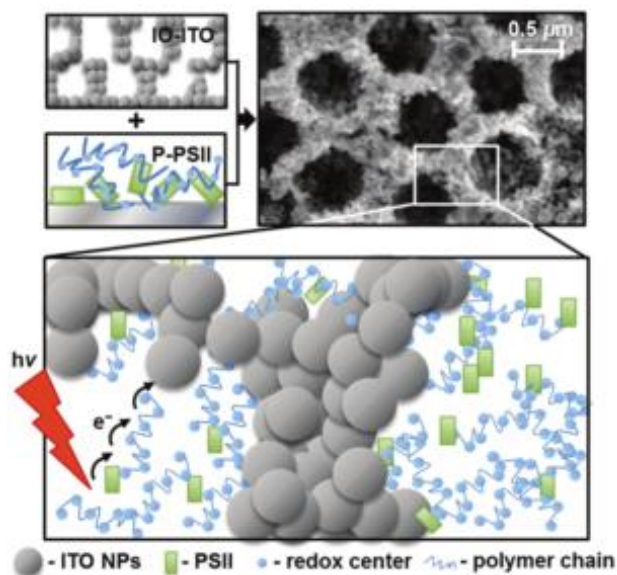
Figure 1.12. Scheme representing Photosystem II wired through a redox polymer to a hierarchically structured porous ITO electrode with the electron transfer path indicated after the photoexcitation of PS II. The SEM image of the porous ITO is also attached.[81]

From this section, despite the wide variety of configurations, one can try to draw conclusions for potential of applications in electroanalysis. It is obvious that a very important factor is the conductivity of the porous layer as the high resistance can severely impede the electrochemical response. As shown before, higher conductivity of the layer is useful in improving the kinetics of the photoelectrochemical reaction and charge transfer[50]. High resistivity therefore might be a problem when performing electroanalysis of some analytes. Another important factor is the type of porosity that is used. While mesoporous electrodes can provide higher surface area macroporous electrode could provide better access to the pores. In general, mesoporous ordered layers might be the most suitable for detecting compounds, as the surface available for sensitization (and therefore electrochemistry) could be increased by over two orders of magnitude with good access to the pores.[59] On the other hand if the sensing would need to be realized by immobilizing the protein then a more open macroporous structure would more preferable.[79,80] These prospects of utilizing transparent and porous electrodes are exciting because they could combine increased electrochemical sensitivity through higher active surface area that allows for immobilization or preconcentration of higher amount of spectroscopically detectable compound.

1.3.2. Electroanalysis

One of the first examples of using a porous and transparent electrode in studying a molecule with spectroelectrochemistry was a work of Topoglidis *et al.* where a tin oxide mesoporous film was used to adsorb small heme proteins. The goal of that study was to follow the direct electrochemistry of those proteins and their interaction with nitric oxide and it was shown that this kind of electrode can be used as a sensor.[4] The sensing potential was also explored with porous FTO to detect common ions in water solution.[106] The first example of a transparent conducting oxide electrode used for spectroelectroanalytical application was the work made by Frasca *et al.* in 2010 where an ITO mesoporous transparent electrode was used for the immobilization of cytochrome *c*. The authors studied the properties of the immobilized protein under different applied voltage (Figure 1.13).[57] In the course of the study surface concentration was found to be 10 times higher than on similarly modified planar electrodes and the structure integrity of the protein was well maintained. Surface concentrations of oxidized and reduced protein were comparable proving that the protein was fully redox active. Such layer was then applied for detection of superoxides by amperometry. Tin-rich mesoporous ITO was also used to study the spectroelectrochemical behavior of cytochrome *c*.
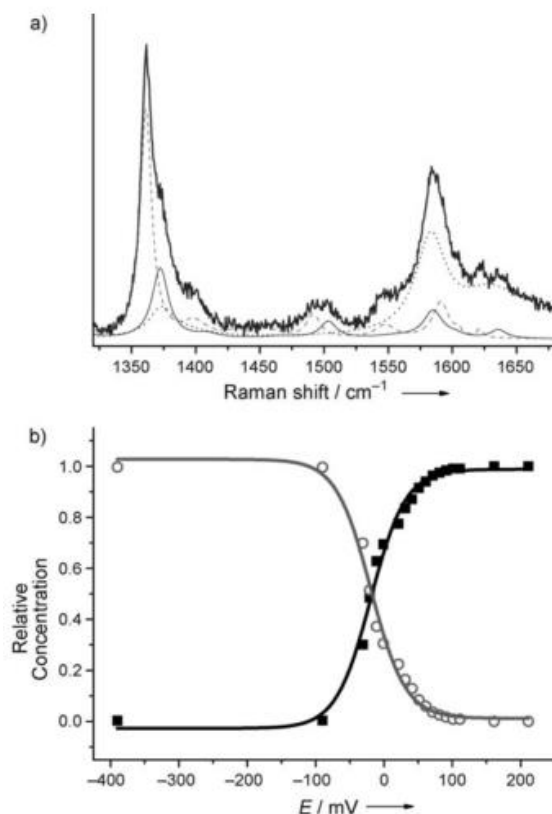
Figure 1.13. (a) Resonance Raman spectrum measured at 0 V of cytochrome c *deposited on mesoporous ITO divided into contributions from ferric (solid line) and ferrous forms (dashed line) of the protein as well as the substrate (dotted line). (b) Relative concentration of the ferrous (cricles) and ferric (squares) forms of cytochrome* c *vs the potential applied. Lines represent fitting of the experimental data to Nernst equation.*[57]

Two different templates were used for the deposition of the porous ITO electrode and it was found that despite having larger size KLE polymer-templated layers did not provide better access to the surface area than smaller F127.[64] The postulated reason for that was that the KLE-templated layers were less ordered and had less pore interconnections. It has been also shown that the spectral response of immobilized cytochrome *c* could be changed electrochemically with mesoporous ATO as well. The surface coverage was found to be 2 orders of magnitudes higher than that for planar electrodes.[67] Furthermore, adsorption of microperoxidase-11 (MP-11) was also studied by combining time-resolved UV-Vis spectrometry and electrochemistry (Figure 1.14).[94] The concept was later expanded and more detailed study of immobilized MP-11 and the catalytic mechanism of O_2 reduction was studied in detail thanks to combined spectral and electrochemical approaches. Variable thickness of the porous layer allowed for studying different loading of the protein.[95] Finally,

adsorption of cytochrome *c* and neuroglobin was performed on mesoporous ITO and thanks to high transparency of the electrodes the thermodynamic and kinetic parameters of electron transfer between these proteins and the surface could be calculated from voltabsorptograms.[96]
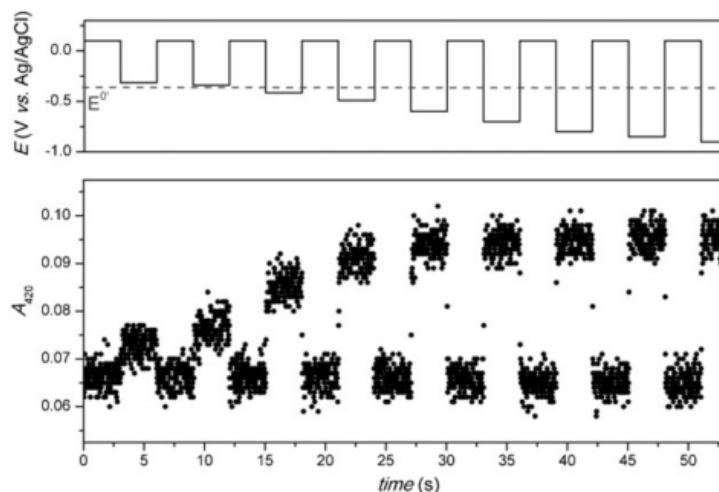
Figure 1.14. Absorbance measured at 420 nm vs the applied potential pulses (from 0.1 to -0.9 V) of mesoporous ITO electrode loaded with Microperoxidase-11 in 0.1 M HEPES, pH=7.[94]

Not only proteins have been studied in electroanalysis on transparent and porous electrodes. $[Ru(bpy)_3](PF_6)_2$ phosphonate derivative was immobilized by Hoertz *et al.* on mesoporous ITO leading to the current response 140 times bigger than on a planar electrode.[39] Because of this, it was possible to follow the change of oxidation state of ruthenium (Figure 1.15) through spectrometry upon applying different potentials (0.55 V for reduced form and 1.55 V for oxidized form). Moreover, the transparency of the electrode can be useful in electroanalysis not only for the purpose of following the electrochromic properties but also by allowing to determine the presence of the compound on the surface with simple technique that is UV-Vis spectrometry. For example in the work by Muller *et al.* the presence of immobilized cytochrome *c* could be confirmed by such measurement and coupled with electrochemical experiment give convincing evidence of successful grafting procedure.[13] The same concept was also applied in different reports to confirm the immobilization of ruthenium complex[51], Eosin Y carbonate[15] and again cytochrome *c*.[64] Transparent porous electrodes were also used to deposit electrochromic species like viologen on macroporous FTO in solid state electrolyte.[75] Finally, a mesoporous ATO electrode has been used in generation of electrochemiluminescence where higher surface area helped in covalent immobilization of larger amount of Ru complex so that the achieved luminescence was estimated to be 132 higher than on planar electrode (Figure 1.16).[61] This is relevant for electroanalysis because

ECL can be used in a construction of very sensitive sensors capable of detecting picomolar concentrations[12] and increasing the ECL intensity by 2 orders of magnitude could bring the limits of detection even lower.
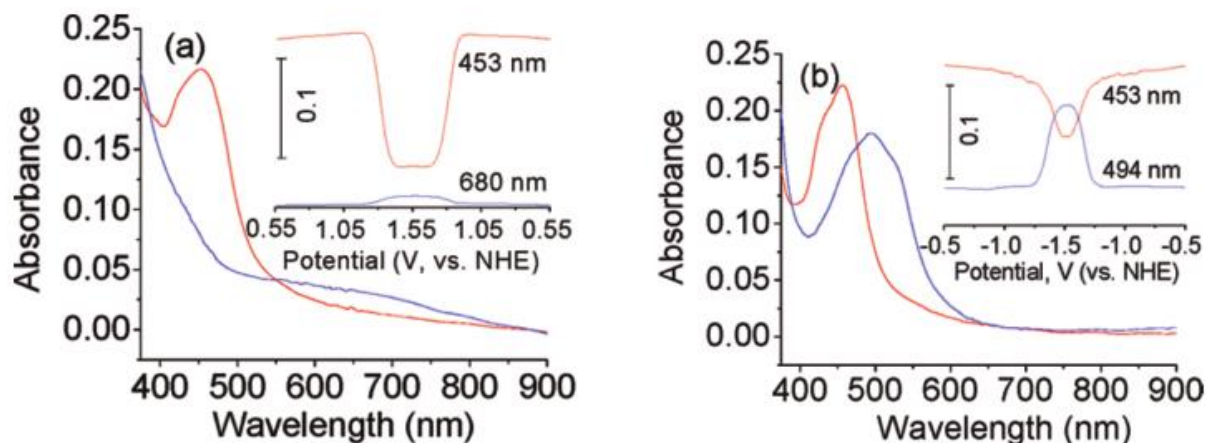
Figure 1.15. UV-Vis absorbance spectra of Ru immobilized on porous ITO electrode in reduced (red) and oxidized (blue) form. The inset shows absorbance changes at two different wavelengths during a cyclic voltammetry scanning (at 10 mV s^{-1}) in (a) 0.1 M HClO$_4$ and (b) n-Bu$_4$NPF$_6$/MeCN.[39]
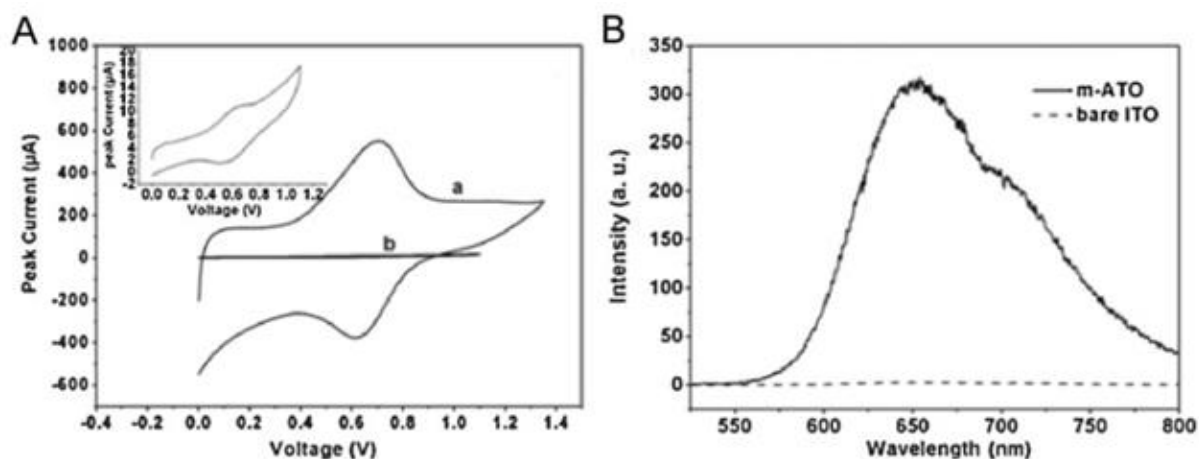
Figure 1.16. (A) Cyclic voltammetry of ferrocene carboxylic acid immobilized on (a) mesoporous ITO and (b and inset) dense ITO films (scan speed 100 mV s^{-1}). (B) Electrochemiluminescence intensity of porous and dense ITO films.[61]

1.3.3. Other applications

Alongside the most popular applications transparent porous electrodes were also used in several niche areas. For example, macroporous AZO was used as a very sensitive light

switch[116]. In another publication mesoporous ITO was used to build a GaN- based LED that achieved 35% higher efficiency than conventional diodes.[18] Furthermore, influence of the dual-layer porosity of ITO on electroluminescence (EL) in the same type of LED was studied and it was found that the EL of such device was improved by properly adjusting the porosity the reduced reflectivity of the film.[99] Electrodeposition of bismuth on macroporous ATO electrodes was used to prove the concept of photonic crystal switch where the reflectivity of the film could be tuned from 5 to 30 % range by applying different potential.[73] Finally, a mesoporous ITO electrode was used to fabricate a solar biocapacitor – a device which is able to capture and store the solar energy at the same time (Figure 1.17).[45] It was capable of reaching a power density of 6 mW * m^{-2}.
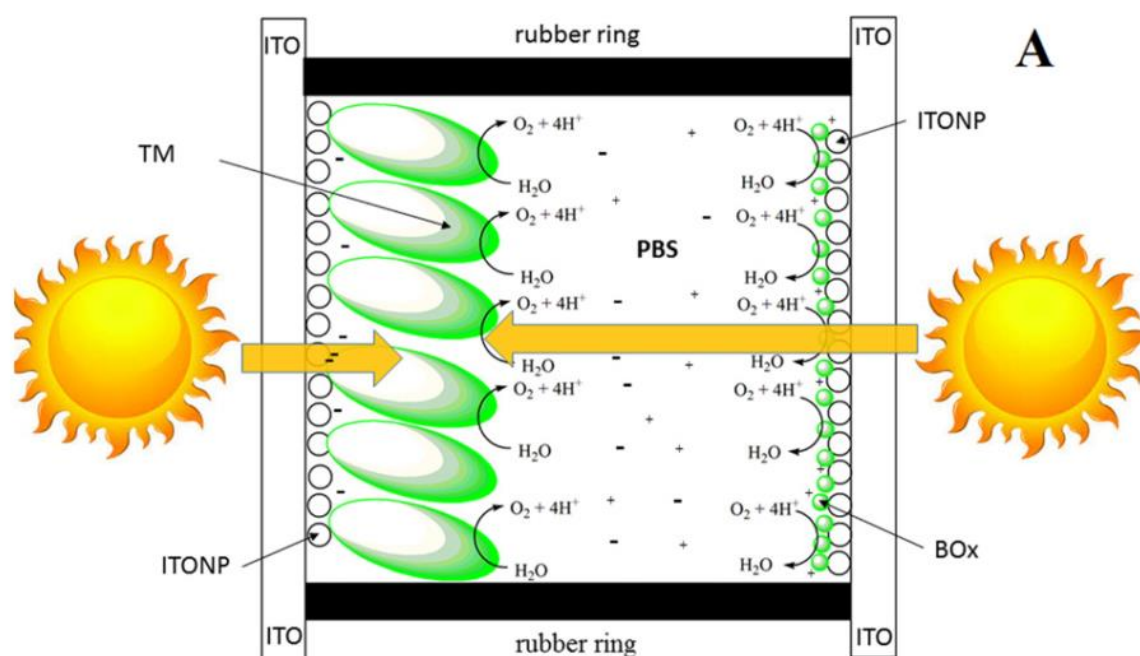
Figure 1.17. Molecular mechanism of solar biosupercapacitor functioning. ITO – ITO plate, ITONP – ITO nanoparticle, TM – thylakoid membrane, BOx – bilirubin oxidase.[45]

1.4. Porous and transparent organic electrode materials

Compared to inorganic transparent and conductive materials organic materials like polymers or carbon presents a different range of useful qualities like flexibility[118] or lower cost of preparation due to lack of need for expensive metals. In the literature many examples of transparent carbon materials[21] have been presented but this introductory part will discuss only examples with porous structures on meso- and macroscale. In 2010 Malavé Osuna *et al.* reported the deposition of PEDOT on carbon nanotube films that resulted in the formation of

a macroporous transparent electrode.[119] Another interesting protocol involved using a mesoporous silica film (SBA-15) as template for the deposition of a thin organic layer that was later carbonized to obtain conductive mesoporous carbon electrode (Figure 11).[120] A different way to prepare transparent macroporous carbon electrodes relies on chemical vapor deposition on an anodized alumina template with channels 80 nm in diameter and 140 nm in length. Additionally, an array of nanotubes that were 25 nm in diameter and 330 nm in length could be added on top of those films to increase the surface area.[121] Furthermore, deposition of a composite polyaniline – reduced graphene oxide (PANI-RGO) on FTO substrate was demonstrated which resulted in a worm-like morphology.[122] Finally, two protocols of porous graphene were published. In the first one, a micro- and mesoporous electrode was prepared using prismlike graphene blocks with surface area of 909 m^2*g^{-1}.[123] In the second, one graphene was deposited using MOCVD with NaCl crystals as template achieving surface area of 1105.6 m^2*g^{-1}.[124] Most popular application of those organic electrodes is in flexible transparent supercapacitors. They are capable of reaching the power densities of 19 $mW*cm^{-3}$ [121], 190 $mW*cm^{-3}$ [123] and 562 $mW*cm^{-3}$.[124] In another report WO3 on macroporous PEDOT/CNT composite is used for potential display applications.[119] Finally, a mesoporous PANI-RGO composite electrode was tested as a counter electrode in bifacial DSSC.[122]
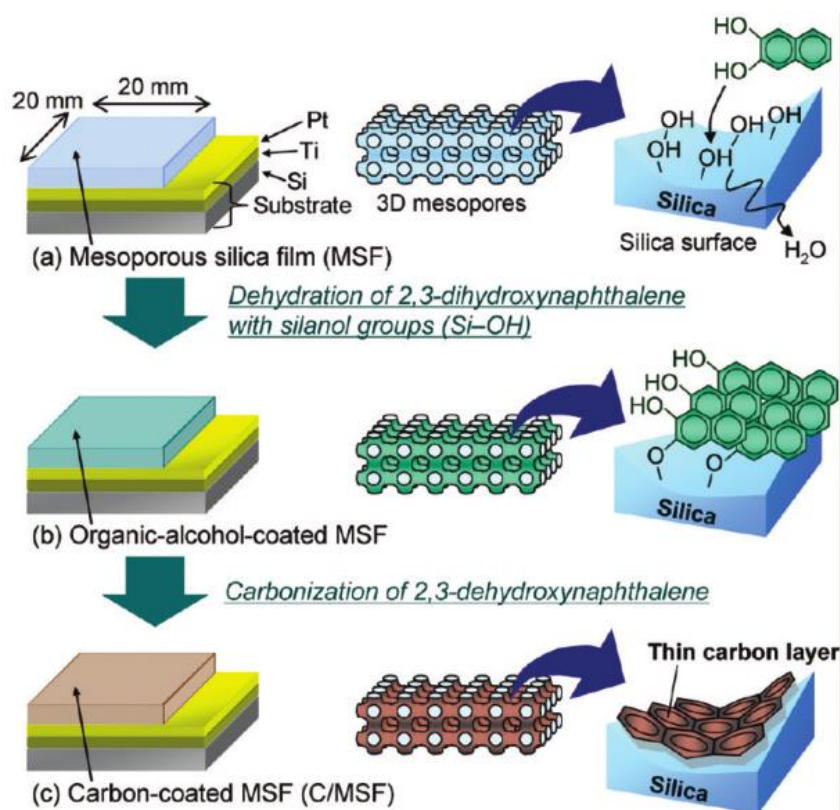
Figure 1.18. *Preparation method of thin transparent carbon layer on mesoporous silica*[120]

30

1.4. Conclusions

In this report we have presented a comprehensive list of methods for depositing porous and transparent layers composed of conductive oxides. Those methods range from the simplest depositions of unorganized nanoparticles, electrospinning or top-down methods, to more elaborate methods including templated depositions or physical deposition methods. The architectures and pore sizes can vary from few nanometers to dozens of microns and are adjustable to achieve desired effect and both meso- and macroporous films can be obtained of different thickness ranging from 100 nm to 5 μm. Furthermore, due to the porous nature of those electrodes the transparency in some cases might be as low as 40% in the visible wavelength range but it can even reach up to 95 % for the best ones. One persistent limitation is the lack of UV transparency which can be achieved only using carbon materials that have lower overall transparency. Finally, applications of those electrodes were presented and so far the focus of the scientific world has been put on energy generation. Considering the maturity of this material science field, new development in analytical protocols combining spectroscopic and electroanalytical in porous and transparent electrode should appear in the future. First such applications are already present like the studies of protein behavior under different applied potential or the enhanced ECL generation.

Table 1.1. Summary of the deposition methods of porous transparent TCO electrodes. Alongside the methods the characteristics of the resulting material are presented, like porosity, resistivity and transparency. Used abbreviations and symbols: R_s = sheet resistance, ρ = resistivity, T_{vis} = average transparency in the visual wavelength range, ECL = electrochemiluminescence, DSSC – dye-sensitized solar cell, LED = light-emitting diode, ITO – indium tin-doped oxide, ATO – antimony-doped tin oxide, FTO – fluorine-doped tin oxide, NTO – niobium-doped tin oxide, AZO – aluminum-doped zinc oxide, BZO – boron-doped tin oxide

Material	Deposition method	Porosity	Application	Other parameters	Ref.
ITO	Non-templated nanoparticle deposition	Mesoporous, disordered	-	$\rho = 3.4 \cdot 10^{-3}$ Ω cm	[14]
ITO	Non-templated nanoparticle deposition	Mesoporous, disordered	-	(deposited on already conductive substrate)	[37]
ITO	Non-templated nanoparticle deposition	Mesoporous, disordered	-	$\rho = \sim 10^{-2}$ Ω cm, $T_{vis} = 90$ %	[38]
ITO	Non-templated nanoparticle deposition	Mesoporous, disordered	-	$R_s = 45$ Ω sq^{-1}, $T_{vis} = 50$ %	[39]
ITO	Non-templated nanoparticle deposition	Mesoporous, disordered	-	$R_s = 4.02$ kΩ sq^{-1}, $T_{vis} = 90$ %	[40]
ITO	Non-templated nanoparticle deposition	Mesoporous, disordered	Photoelectrochemical water oxidation	$R_s = 8.4$ kΩ sq^{-1},	[29,44]
ITO	Non-templated nanoparticle deposition	Mesoporous, disordered	Solar biosupercapacitor	(deposited on already conductive substrate)	[45]
ITO	Non-templated nanoparticle deposition	Mesoporous, disordered	Semiconductor--sensitized solar cell	(deposited on already conductive substrate)	[47,48]
ITO	Non-templated nanoparticle deposition	Mesoporous, disordered	-	$T_{vis} = 50$ %	[49]

ITO	Non-templated nanoparticle deposition	45-49 %, mesoporous, disordered	-	$\rho = 2.27 * 10^{-2}$ Ωcm, $R_s = 50$ Ω sq^{-1}, $T_{vis} = 90$ %	[23]
ITO	Non-templated nanoparticle deposition	Mesoporous, disordered	-	$T_{vis} = 60$ %	[51]
ITO-TiO$_2$ composite	Non-templated nanoparticle deposition	Mesoporous, disordered	DSSC	(deposited on already conductive substrate)	[52]
ITO	Non-templated particle deposition	Macroporous, disordered	-	$R_s = 0.2\text{-}2$ kΩ sq^{-1} $T_{vis} = 10\text{-}30$ %	[53]
ITO	Salt precursor deposition templated by CTAB	Mesoporous, pore size 4.4 nm, ordered	-		[54]
ITO	Salt precursor deposition templated by CTAB	Mesoporous, pore size 2-2.5 nm, ordered	-	$\rho = 1.2 * 10^{-2}$ Ωcm, $T_{vis} = 80$ %	[55]
ITO	Salt precursor deposition templated by block copolymer (KLE)	Mesoporous, pore size 15-20 nm, periodically ordered	Spectroelectrochemistry	$\rho = 2 * 10^{-2}$ Ωcm, $R_s = 1.3$ kΩ sq^{-1}, $T_{vis} = 90$ %	[15,56,57]
ITO	Salt precursor deposition templated by block copolymer (PIB-PEO)	Mesoporous, pore size 20-25 or 35-45 nm, ordered	-		[58]
ITO	Salt precursor deposition templated by block copolymer (PIB-PEO)	Mesoporous, pore size ~25 nm, ordered	DSSC	$\rho = 2.5 * 10^{-2}$ Ωcm $T_{vis} = 80$ %	[59]
ITO	Metaloorganic precursor deposition templated by block copolymers	Mesoporous, pore size 5, 6.5 or 12.5 nm, disordered	-	$\rho_1 = 0.64 * 10^{-2}$ Ωcm, $R_{s1} = 91$ Ω sq^{-1}, $\rho_2 = 1.73 * 10^{-2}$ Ωcm, $R_{s2} = 115$ Ω sq^{-1} $T_{vis} = 60$ %	[64]

ITO	Nanoparticle deposition templated by block copolymer (F127)	44 %, mesoporous, pore size 10-15 nm, disordered	-	$\rho = 10.5 * 10^{-2}$ Ωcm	[70]
ITO	Nanocrystal deposition templated by block copolymer (PDMA-PS)	Mesoporous, pore size 23, 33, 34 nm, ordered			[24]
ITO	Salt precursor deposition templated by PC membrane	Macroporous, pore size 100 and 200 nm, disordered	DSSC	(deposited on already conductive substrate)	[72]
ITO	Nanoparticle deposition templated by PMMA beads	Macroporous, pore size 100 (ordered) and 370 nm (disordered)	-	$\rho = 25 * 10^{-2}$ Ωcm, $T_{vis} = 80$ %	[77]
ITO	Nanoparticle deposition templated by PS beads	Meso- (disordered) and macroporous (~750 nm pore size, ordered)	Photoelectrochemical water splitting, photocurrent generation	(deposited on already conductive substrate)	[79–81]
ITO	Pulsed laser deposition	Mesoporous, disordered	DSSC	$R_s = 80$ Ω sq^{-1}	[86]
ITO	Radio frequency sputtering	Macroporous (not inter-connected), disordered	-		[87]
ITO	Radio frequency sputtering	Macroporous (not inter-connected), disordered	Organic solar cell	$\rho = 0.2 - 0.35 * 10^{-2}$ Ωcm, $R_s = 200 – 450$ Ω sq^{-1} $T_{vis} = 95$ %	[88,89]
ITO	Physical vapor deposition	Macroporous (not inter-connected), disordered	DSSC	$\rho = 0.047 * 10^{-2}$ Ωcm	[91,92]
ITO	Glancing angle deposition	Mesoporous, disordered	Spectroelectrochemistry	(deposited on already conductive substrate)	[93–96]
ITO	Glancing angle deposition	Mesoporous, disordered	-	$\rho = 0.25-0.75 * 10^{-2}$ Ωcm	[97]

ITO	Glancing angle deposition	Mesoporous, disordered	Tandem thin film solar cell	ρ = 0.05-0.2 * 10^{-2} Ωcm R_s = 15-70 Ω sq^{-1} T_{vis} = 79 – 95 %	[16]
ITO	Glancing angle deposition	Mesoporous, disordered	-	T_{vis} = 5 – 80 % (deposited on already conductive substrate)	[98]
ITO	Glancing angle deposition	Mesoporous, disordered	LED		[99]
ITO	Physical vapor deposition templated by AAO	Macroporous, ordered	-	R_s = 108.6 – 259.4 Ω sq^{-1} T_{vis} = 80 %	[25]
ITO	Atomic layer deposition templated by PS particles/inverse opal structure SiO_2	Macroporous, pore size 350 nm, ordered	Photoelectrochemical water splitting	(deposited on already conductive substrate)	[102]
ITO	Etching with HNO_3	Mesoporous, disordered	LED	R_s = 60 – 130 Ω sq^{-1} T_{vis} = 70 – 90 %	[18]
ITO	Anodic etching	Macroporous, disordered	-	ρ = 11* 10^{-2} – 100 Ωcm T_{vis} = 90 %	[26]
ITO	Electrospinning	Macroporous, disordered	-		[115]
ITO	Electrospinning	Macroporous, disordered	Semiconductor- -sensitized solar cell	R_s = 0.3 – 6.4 $k\Omega$ sq^{-1} T_{vis} = 79-99 %	[27]
ITO	Electrospinning	Macroporous, disordered	DSSC	"Resistance of the 1.2-1.5 µm thick mat was 2 $k\Omega$ cm^{-1}"	[117]
ATO	Non-templated nanoparticle deposition	Mesoporous, disordered	-	ρ = 1.7 * 10^{-2} Ω cm	[14]

35

ATO	Non-templated nanoparticle deposition	Mesoporous, disordered	-	$\rho = 52 * 10^{-2}$ Ω cm $T_{vis} = 60-80$ %	[41]
ATO	Non-templated nanoparticle deposition	Mesoporous, disordered	-	$\rho = 4000 * 10^{-2}$ Ω cm	[42]
ATO	Non-templated nanoparticle deposition	Mesoporous, disordered	-	$T_{vis} = 50-80$ %	[43]
ATO	Salt precursor deposition templated by block copolymers (KLE and PIB-PEO)	Mesoporous, ordered	-	$\rho = 3.44 * 10^{-2}$ Ω cm (best)	[60]
ATO	Salt precursor deposition templated by block copolymer (F127)	Mesoporous, pores elpitical with 12.5 x 5.6 nm size, ordered	ECL	$\rho = 10 * 10^{-2}$ Ω cm $T_{vis} = 85$ %	[61]
ATO	Salt precursor deposition templated by block copolymer (HmSEBmS)	Mesoporous, pore size 15 nm, ordered (the most optimal variant)	-	$\rho = 100 * 10^{-2}$ Ω cm	[63]
ATO	Salt precursor deposition templated by organic network	Mesoporous, avg. pore size 7.2 – 33 nm, disordered	Spectroelectrochemistry, photocurrent generation with bacterial centers	$T_{vis} = 80$ % (deposited on already conductive substrate)	[65–68]
ATO	Nanocrystal deposition templated by block copolymer (F127)	Mesoporous, pore size 10 nm, porosity ~ 50 %, ordered	-	$\rho = 125 * 10^{-2}$ Ω cm	[13,69]
ATO	Nanoparticle deposition templated by block copolymer PEO-PHA	Meso- and macroporous, pore size 10 or 80nm, ordered, also up to 300 nm disordered	Biophotovoltaics	(deposited on already conductive substrate)	[71]

ATO	Nanocrystal deposition templated by silica particles	Macroporous, pore size ~200 nm, ordered	-	$R_s = 100 \, \Omega \, sq^{-1}$	[73]
ATO	Nanocrystal deposition templated by PS particles	Macroporous, pore size ~200 nm, ordered	-	$T_{vis} = 60$ % (deposited on already conductive substrate)	[76]
ATO	Nanoparticle deposition templated by PMMA beads	Macroporous, pore size 370 nm, ordered	-	$T_{vis} = 80$ % (deposited on already conductive substrate)	[78]
ATO	Pulsed laser deposition	Mesoporous, disordered	-	$T_{vis} = 50$ % (deposited on already conductive substrate)	[82]
ATO	Electrospinning	Macroporous, disordered	-	$R_s = 400 \, \Omega \, sq^{-1}$	[17]
FTO	Non-templated nanoparticle deposition	Mesoporous, disordered	DSSC	(deposited on already conductive substrate)	[50]
FTO	Salt precursor deposition templated by PS particles	Macroporous, pore size ~200 nm, ordered	DSSC	(deposited on already conductive substrate)	[74,75]
FTO	Chemical vapor deposition template by pre-drilled substrate	Macroporous, pores conical (30 – 150 μm), ordered	Photoelectrochemical water splitting	$R_s = 40 \, \Omega \, sq^{-1}$ $T_{vis} = 60$ %	[104]
FTO	Anodic etching	Macroporous, disordered	-	$R_s = 15\text{-}19 \, \Omega \, sq^{-1}$ $T_{vis} = 40 – 50$ %	[106]
FTO	Patterned reactive ion etching	Macroporous, ordered	DSSC	$T_{vis} = 70$ %	[107]
NTO	Atomic layer deposition templated by TiO_2	Macroporous, disordered	Photoelectrochemical water splitting	$\rho = 2.7 – 7.1 * 10^{-2} \, \Omega$ cm $T_{vis} = 90$ %	[103]
AZO	Non-templated nanorod deposition	Mesoporous, disordered	DSSC		[46]

AZO	Salt precursor deposition templated by block copolymer (F127)	Mesoporous, disordered	-	$\rho = 8 * 10^{-2}$ Ω cm $T_{vis} = 83$ %	[62]
AZO	Pulsed laser deposition	Mesoporous, disordered	-	$\rho = 0.04 - 10 * 10^{-2}$ Ω cm $R_s = 10 - 2000$ Ω sq^{-1} $T_{vis} = 55\text{-}90$ %	[83–85]
AZO	Radio frequency sputtering	Mesoporous, disordered	-	$R_s = 137 - 692$ Ω sq^{-1} $T_{vis} = 75 - 90$ %	[90]
AZO	Atomic layer deposition template by PS beads	Macroporous, disordered	DSSC	(deposited on already conductive substrate)	[101]
AZO	Spray pyrolysis	Mesoporous, disordered	DSSC	(deposited on already conductive substrate)	[105]
AZO	Electrospinning	Macroporous, disordered	Light-driven switch		[116]
BZO	Salt precursor deposition templated by block copolymer (F127)	Mesoporous, disordered	-	$\rho = 1.7 - 2.4 * 10^{-2}$ Ω cm $T_{vis} = 71 - 99$ %	[62]

Positioning of the PhD thesis

From the literature survey it is possible to conclude that there exist many methods and protocols for the deposition of the porous and transparent electrodes that could be useful for sensing applications. One must carefully consider what criteria the electrode must possess. Certainly, a high surface area is desirable, as well as good conductivity and transparency in desired wavelength range. Moreover, volume of the material and interconnections between the pores must be large enough to allow post-functionalization. For this reason for the purpose of this work the electrospinning method was chosen. The electrospun electrodes in general are macroporous, which helps in mass transfer, but they do not possess high surface area themselves, but it is possible to functionalize such electrode with an additional mesoporous layer. This could be additionally beneficial since such an electrospun electrode can serve as a base for many different ways of functionalization depending on the desired application. In this thesis it is shown how such electrode can be functionalized with methylated or azide-group-functionalized silica layers. Furthermore, the electrospun electrodes through calcination can reach very high conductivites, in the range of flat commercial films. Finally, electrospun electrodes composed of transparent conductive oxides are transparent in the visible wavelength range. Thereby, it is possible to couple electrochemical measurements with UV-Vis detection and to explore electrochemiluminescence generation. In addition to fulfilling the basic criteria, electrospinning is a cheap and relatively simple technique that can be used in most laboratories and upscaled for potential industrial needs.

Chapter 2. Experimental

2.1. Chemicals

Indium (III) nitrate hydrate 99.99 %, tetraethoxysilane, methyl-triethoxysilane and 3-chloropropyltrimethoxysilane were purchased from Alfa Aesar. Anhydrous tin (II) chloride 98 %, cethyltimethylammonium bromide and Meldola's blue were obtained from Acros Organics. Hydrochloric acid 37 %, polyvinylpyrrolidone of average Mw = 1,300,000, tin(IV) chloride pentahydrate 98 %, iron(III) chloride hexahydrate 98 %, methylene green, tetrabutylammonium bromide, sodium azide, ruthenium (III) chloride trihydrate, polystyrene of average Mw = 280,000, 1,1'-dimethanolferrocene 98 % and N,N'-dimethylformamide 99.8 % were purchased from Sigma Aldrich and ethanol absolute and acetone 99.9 % were obtained from Carlo Erba. L (+) Ascorbic Acid 99.7 % was a Merck product and potassium chloride 99 % as well as copper (II) acetate were Prolabo products. Methylene blue, lithium chloride and potassium hexacyanoferrate(III) 99% were obtained from Fluka. 2,2'-bipyridine was a Lancaster product. Acetonitrile was purchased from Biosolve.

2.2. Preparation of the suspension

The suspension from which electrospinning was conducted was prepared as follows: 1.12 g of $In(NO_3)_3 * xH_2O$ (ca. 186 mM) and 0.084 g of $SnCl_2$ (ca. 30 mM) were dissolved in mixture of 8.1 mL of ethanol and 6.75 mL of dimethylformamide. Then, the mixture was stirred 3 hours until complete dissolution of the salts. Afterwards 1.2 g of polyvinylpyrrolidone (PVP) was added and again the stirring continued for 2 h until complete dissolution. All steps have been performed at room temperature.

2.3. Preparation of indium tin oxide free-standing nanofiber mats

2.3.1. Electrospinning experiment

Standard horizontal setup was used for electrospinning (Figure 2.1). In short, KdScientific syringe pump was used to deliver solution from 5 ml syringe through a needle 21G with the outer diameter of 0.8 mm. Flow rate imposed by the pump was optimized and then kept at 2 μl min^{-1} during all experiments. Ahead was placed stainless steel collector plate with dimensions of 28 cm x 28 cm. The distance between the needle tip and the collector plate was kept at 12.5 cm. High voltage power supply by Iseg was used to apply potential, with negative pole being connected to the needle. Voltage applied was 10 kV in all experiments unless stated otherwise. Collector plate was connected to ground (0 V) hence the resulting potential

of electrospinning is equal to voltage applied throughout all the experiments. Time of deposition varied between 5 to 40 minutes. After electrospinning procedure, the electrospun matter was stripped off of steel plate collector and became a free-standing mat.
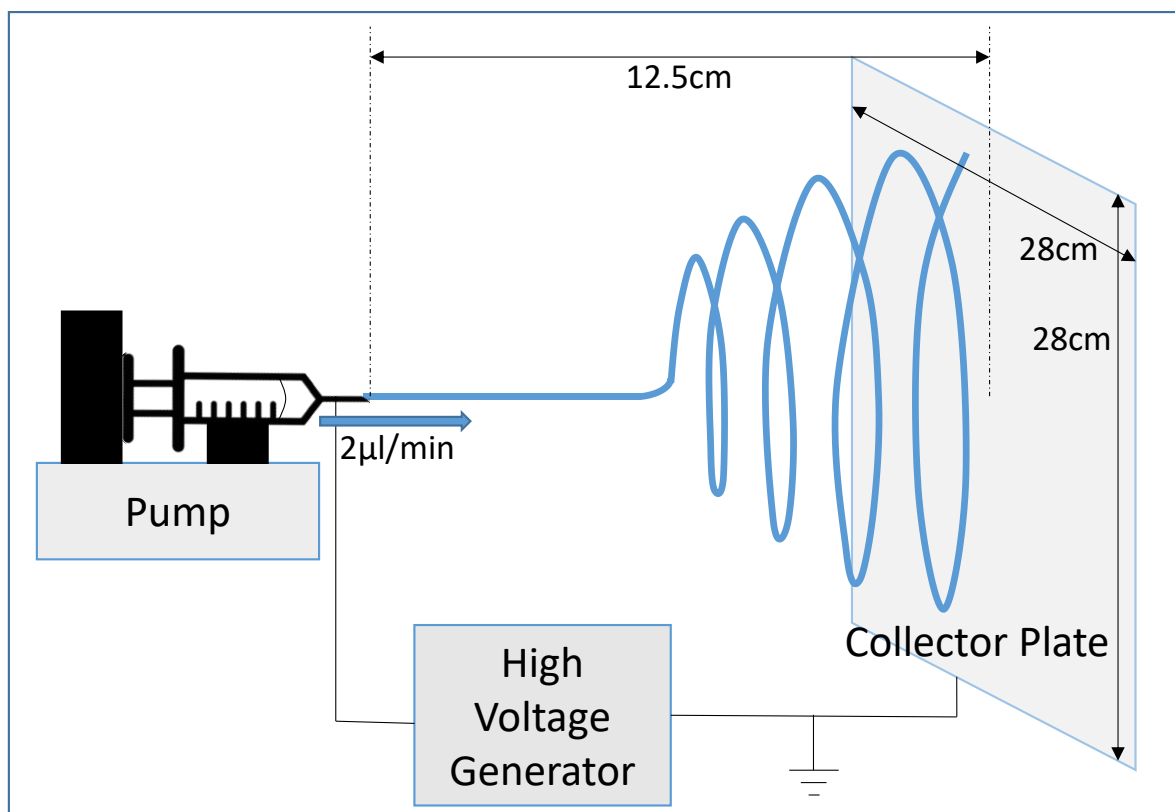
Figure 2.1. *Electrospinning configuration used for deposition of nanofiber layers.*

2.3.2. Post-treatment

Nanofiber mats were transferred to oven to undergo calcination in 500 ˚C in air for 1 h (with temperature ramp of 100 ˚C h^{-1}). Afterwards, they were treated at 1000 ˚C for 1h under nitrogen atmosphere (with temperature ramp of 100 ˚C h^{-1}) unless stated otherwise in results section. Nitrogen gas was treated with help of two adsorbent cartridges (oxygen adsorbent and water adsorbent) provided from "Spectron Gas Control Systems GmbH, Germany".

2.3.3. Preparation of mats for measurements

Free-standing mats were immobilized on glass using two different procedures. First type of immobilization went as follows: a double-sided scotch tape was placed on the glass plate, afterwards a nanofiber layers was placed on top of the tape and firmly pressed to ensure proper adhesion. Second type of immobilization was done using previously published procedure [49]. Shortly, glass plate was wetted with 5 % SnCl$_4$ hydrate solution in ethanol.

Afterwards the nanofiber mat was placed on the glass. The electrode was ready after ethanol evaporation.

2.4. Measurement procedures for indium tin oxide free-standing nanofiber mats

2.4.1. Electrochemical measurements

Cyclic voltamperometry was performed in a solution containing 5 mM of dimethanolferrocene and 0.1 M KCl. Ascorbic acid electroanalysis was evaluated in 0.1 M KCl as well. Palmsense Emstat potentiostat was used for those measurements with standard three-electrode setup. Reference electrode was Ag/AgCl/KCl 3M. Counter electrode was made of stainless steel and working electrodes had geometric surface area about 12.6 mm^2. For deposition of Prussian blue on nanofibers solution of 5 mM $FeCl_3$, 5 mM $K_3[Fe(CN)_6]$, 0.01 M HCl and 0.1 M KCl was used and the deposition was performed for 60 s in 0.5 V.

2.4.2. Spectroelectrochemical measurements

Agilent Technologies Cary 60 UV-Vis spectrometer was used for spectroelectrochemical measurements. The same potentiostat as mentioned before were used and the experiments were conducted in 0.1 M KCl, 0.01 M HCl solution. Three-electrode setup was used with Ag/AgCl pseudoreference electrode, platinum wire as counter electrode and ITO nanofiber mats as working electrodes.

2.5. Preparation of indium tin oxide nanofilament layers

2.5.1. Substrate preparation

Fused silica plates used as substrates were polished with alumina (0.1 and 0.05 µm) and afterwards rinsed with water and ethanol. Then the plates, dimensions 20x20x1 or 30x10x1 mm, were covered by polystyrene solution in toluene 10% w/w by drop coating and left for solvent evaporation under the hood for around 1h. The volume used for the thick film formation was 300 and 225 µl respectively (0.75 µl mm^{-2}).

2.5.2. Electrospinning experiment and post-treatment

The electrospinning procedure and equipment is similar to one used for obtaining ITO free-standing mats (section 2.3.1) including the flow rate of 2 µl min^{-1} and the size of the collector plate of 28 x 28 cm. The only changes to the protocol were as follows: distance between the needle tip and the collector plate was kept at 10 cm, voltage applied was 9 kV and in the

middle of collector plate the fused substrates covered with PS were immobilized with double-sided carbon tape. Time of deposition was 20 minutes and relative humidity was around 50% at room temperature.

After the electrospinning the fused silica plates covered with nanofibers were transferred to the oven to undergo calcination in 500 ˚C in air for 1 h (with temperature ramp of 100 ˚C h^{-1}). Afterwards, they were treated at 1000 ˚C for 1h under nitrogen atmosphere (with temperature ramp of 100 ˚C h^{-1}) unless stated otherwise in the results section. Nitrogen gas was treated with help of two adsorbent cartridges (oxygen adsorbent and water adsorbent) provided from "Spectron Gas Control Systems GmbH, Germany". Then, the samples have been left to cool down in the oven. Finally, after heat treatment the samples were rinsed with water and then with ethanol. The whole procedure of preparing the samples for further experiments is presented in graphic form on Figure 2.2.
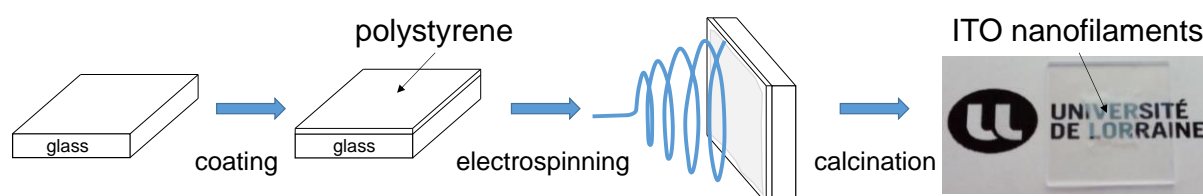
Figure 2.2. *Experimental procedure scheme for obtaining ITO nanofilament layers. The picture is showing the porous ITO in the wet state.*

2.5.3. Mesostructured methylated silica deposition

The functionalization of ITO plates or ITO nanofilament layers on fused silica with methylated mesostructured silica was achieved by applying -1.3 V for 20 s or longer if specified in deposition solution according to previously published procedure.[125] Preparation of the sol was as follows: 0.47 g of cethyltrimethylammonium bromide was dissolved in mixture of 20 ml of ethanol and 20 ml of 0.1 M solution of $NaNO_3$ in water. After the complete dissolution 0.65 ml of tetraethoxysilane and 0.23 ml of methyl-triethoxysilane were added followed by adjusting pH to 3 with HCl. Afterwards the plates were put in oven at 130 °C overnight. Finally, the surfactant was removed in 0.1M HCl under stirring for 15 minutes. Finally plates were rinsed with water and then with ethanol.

2.5.4. Click-functionalized silica deposition and Ru complex functionalization

2.5.4.1. Synthesis of 4-[(2-propyn-1-yloxy)methyl]-4'-methyl-2,2'-bipyridine (bpy')

The synthesis of the bipyridine derivative was performed by a previously reported procedure[126] starting from 4,4'-dimethyl-2,2'-dipyridyl in three main steps:

- Synthesis of 4-(carboxyaldehyde)-4'-methyl-2,2'-bipyridine

- Synthesis of 4-(hydroxymehtyl)-4'-methyl-2,2'-bipyridine

- Synthesis of 4-[2-propyn-1-yloxy)methyl]-4'-methyl-2,2'-bipyridine

2.5.4.2. Synthesis of $Ru(bpy)_2Cl_2$

$RuCl_3.3H_2O$ (1.0 g; 8.8 mmol), bipyridine (1.2 g; 7.6 mmol), and LiCl (1.1 g) were refluxed in reagent grade DMF (7 ml) for 8 h with magnetic stirring. Then, the reaction mixture was cooled to room temperature, and reagent grade acetone (32 ml) was added. The reaction mixture was afterwards cooled to 0°C overnight. The mixture was then filtered, yielding a red-violet filtrate and a black crystalline substance. Finally, the solid was washed three times with 10 ml of water followed by three 10 ml of diethyl ether, and was subsequently dried by suction (yield: 0.72 g; 39.1%).

2.5.4.3. Synthesis of $[Ru(bpy)_2(bpy')](PF_6)_2$

$Ru(bpy)_2.Cl_2$ (2 mmol), and 4-[2-propyn-1-yloxy)methyl]-4'-methyl-2,2'-bipyridine (1 mmol), and LiCl (1.077 g) were refluxed in reagent grade DMF (20 ml) for 24 h with magnetic stirring. The reaction mixture was cooled to room temperature, and reagent grade acetone (50 ml) was added. The mixture was then filtered, yielding a red-orange solid (0.3 g).

2.5.4.4. Preparation of azide-functionalized silica precursor

The precursor, (3-azidopropyl)trimethoxysilane (AzPTMS), was prepared following previously published procedure: 3-chloropropyltrimethoxysilane (4 g, 19.1 mmol) was added to a solution of sodium azide (2.16 g, 33.2 mmol) and tetrabutylammonium bromide (1.290 g, 4 mmol) in dry acetonitrile (100 mL) under nitrogen atmosphere. Then, the reaction mixture was stirred under reflux for 48 h. Afterwards this period, the solvent was reduced under reduced pressure. The crude mixture was diluted in cyclohexane and filtered. finally, the solvent was removed from the resulting filtrate and the crude oil obtained was distilled under reduced pressure.

2.5.4.5. Deposition of click-functionalized mesoporous silica films

The functionalization of ITO plates or ITO nanofilament layers on fused silica with methylated mesostructured silica was achieved by applying -1.3 V for 20 s or longer if specified in deposition solution according to previously published procedure.[125] The composition of the sol was prepared as follows: 200 mM of TEOS and 50 mM of AzPTMS as the silica precursor, 64 mM CTAB in 0.1 M $NaNO_3$ as supporting electrolyte. The sol pH was adjusted to 3 by the addition of 0.1 M HCl and stirred for 2.5 hours. Afterwards the plates were put in oven at 130 °C overnight. Finally, the surfactant was removed in 0.1M HCl in ethanol under stirring for 15 minutes.

2.5.4.6. Functionalization with Ru complex

The $[Ru(bpy)_3(bpy')]^{2+}$-functionalized silica films have been prepared on flat and porous ITO electrodes by by functionalizing vertically-aligned mesoporous films described in Section 2.5.4.5, using Huisgen click chemistry with ethynyl-$Ru(bpy)_2(bpy')$. The click reaction was conducted for 18-24 hours, where the surfactant-extracted azide-functionalized films were immersed in the dark in a mixture solution of ethynyl-$Ru(bpy)_2(bpy')$ (20.0 mg) in DMF/H_2O (10/10 mL), Cu(II)acetate 1 M (20 µL) and Ascorbic Acid 1 M (50 µL).

2.6. Measurement procedures for indium tin oxide nanofilament layers

2.6.1. Electrochemical measurements

Cyclic voltamperometry (CV) was performed in an aqueous solution containing 5 mM of dimethanolferrocene and 0.1 M KCl. Ascorbic acid electroanalysis was evaluated in aqueous 0.1 M KCl as well. Palmsense Emstat potentiostat was used for those measurements with a standard three-electrode setup. Reference electrode was an Ag/AgCl/KCl 3 M. Counter electrode was made of stainless steel and working electrodes had geometric surface area of 12.6 mm^2.

Differential pulse voltammetry (DPV) detection of methylene blue was performed in the same as CV. The procedure was as follows: a dried electrode was soaked for 5 minutes in desired concentration of the analyte for adsorption. Then it was quickly rinsed with water, dried with nitrogen flow and installed in the cell for DPV measurement. For regeneration of the electrode it was put in a stirred solution of 0.1 M HCl in water and rinsed with water afterwards. DPV measurement parameters were as follows: 20s equilibration in -0.05 V, scan between 0.05 and

-0.4 V, step potential -5 mV, modulation amplitude 50 mV, modulation time 0.2 s, interval time 0.5 s, effective scan rate: 10 mV/s.

2.6.2. Spectral measurements

Agilent Technologies Cary 60 UV-Vis spectrometer was used for spectral measurements. For industrial dyes detection a sample would be dipped into the 100 µM solution of respective dye for 60 s. Afterwards it was quickly rinsed with water and then put into the cell for measurement the experiment.

2.6.3. Electrochemiluminescence measurements

For electrochemiluminescence measurements SAFAS Xenius XM instrument was coupled with EmStat potentiostat. The cell was adapted from standard sample holder to include Ag/AgCl reference electrode, Pt counter electrode and space to mount the working electrode.

2.7. Characterization

High-resolution scanning electron microscopy was performed using JEOL J7600F instrument with 1 kV acceleration. Energy-dispersive X-ray spectroscopy was done using JEOL Neoscope JCM 6000 with 15 kV acceleration.

The XRD measurements were performed using a Panalytical X'Pert Pro diffractometer equipped with a Cu tube, a Ge (111) incident-beam monochromator (λ=1.5406Å) and a X'Celerator detector. Wide-angle X-ray scattering (WAXS) measurements were collected using 0.02 rad Soller slits, programmable divergence and anti-scatter slits, the irradiated area was fixed to 10x10 mm. The X'Celerator detector was used as "scanning line detector (1D)" with 2.122° active length. Data collection was carried out in the scattering angle range 5–70° with a 0.0167° step over 90 min. Small-angle X-ray scattering (SAXS) measurements were collected using 0.02 rad Soller slits, 1/16° fixed divergence and anti-scatter slits. The X'Celerator detector was used as "scanning line detector (1D)" with 0.518° active length. Data collection was carried out in the scattering angle range 0.8–12° with a 0.0167° step over 60 min. Average crystallite size has been obtained using Scherrer's equation where shape factor (K) = 0.9 and X-ray wavelength (λ) = 0.15406 nm on the main peaks of each phase. KLA-Tencor P6 was used for profilometry.

Chapter 3. Indium tin oxide free-standing nanofiber mats and their potential applications in electrochemistry and spectroelectrochemistry

3.1. Introduction

Porous electrodes have been of interest for many years. Their main applications are supercapacitors, electrocatalysis and electroanalysis.[127–129] High electroactive surface area allows for improving the detection of analytes. Indeed, creating bigger area of contact between an electrode and a solution can enhance the sensitivity of the analytical method, i.e. by preconcentration of the analyte on the electrode material itself or on a deposited layer[130], and gives the opportunity to improve the detection selectivity, i.e. by lowering the detection potential of important analytes such as H_2O_2 or NADH.[131]

In some situations, an electrochemical detection at porous electrodes can be advantageously combined with a spectroscopic detection.[57,96,132,133] In general, spectroelectrochemistry allows to analyze single and multiple electron-transfer processes and redox reactions[1] and authorizes a multimode selectivity beneficial for the analytical chemistry.[3,134] A transparent material is however needed to perform spectroelectrochemical measurements through the electrode surface.[134]

According to Cao *et al.*[21] the most applied among the developed transparent materials are transparent conducting oxides (TCOs): indium-tin oxide (ITO), antimony-tin oxide (ATO) and fluorine-tin oxide (FTO). Additionally there are carbon materials like thin layers of graphene or PEDOT or carbon composites of transparent non-conductive polymers with conductive fillers. Of aforementioned materials the most commonly used is ITO. Their very low resistivity (10-50 Ω sq-1)[21] and high transparency (80-95%)[21] have allowed commercial application of non-porous ITO thin films on a wide scale in touch screen devices.[135,136]

ITO can also be prepared in a form of porous electrode and it can be obtained with different degrees of porosity that may suit different goals.[137] One popular group are mesoporous electrodes that offer big relative surface area (up to 200 m2 g-1).[64] There exists a number of methods that allow deposition of thin, well-ordered mesoporous layers. The first group of such methods are vacuum methods like sputtering[88,138], glancing angle deposition[16,139], metalorganic chemical vapor deposition[100] or pulsed laser deposition.[140] Next group are wet

and evaporation methods like spin coating[38,40,54,64], nanocrystal assembly[24,70], doctor blade[23,141], dip-coating[37,58], sol-gel deposition[40] and nanocasting.[142] As mentioned, resulting mesoporous layers have some advantages like high surface area but at the same time diffusion can be dampened and further functionalization is limited.

Another approach is to get a macroporous surface which despite having lower relative surface area possesses some advantages over mesoporous materials like a wider access to the internal surface and better mass transfer through the electrode. Additionally, after the deposition, if needed, they can be functionalized with meso- or microporous layers to maximize the specific surface area or to introduce catalytic activity.[143,144] One common way to obtain macroporous ITO layers is through templating using various procedures like electrochemically assisted deposition[145], self-assembly deposition[146] or electrophoretic deposition.[72] Another way to deposit macroporous ITO layers is electrospinning.[27,108–110,114,115,117,147,148] Compared to methods achieving macroporosity through templating, nanofiber films generated using electrospinning do not have the problem of narrow connections that the former often possess.[77]

Electrospinning of ITO has been already performed using different setups, precursors (indium and tin salts or nanoparticles), solvents (water, methanol, DMF/ethanol mixture) and polymers (poly(vinyl alcohol), poly(ethylene oxide), polyvinylpyrrolidone).[27,108–110,114,115,117,147,148] So far their application was tested in photovoltaic devices[117] or sensing of trimethylamine.[147] However, until now there was no investigation into electrochemical properties of electrospun ITO nanofiber layers despite their great potential. In this work we show the application of electrospun ITO nanofiber layers in electrochemistry and electroanalysis and we demonstrate its suitability for spectroelectrochemistry. Some key parameters of deposition and treatment for these specific applications have been optimized and the materials have been carefully characterized with scanning electron microscopy (SEM) and X-ray diffraction (XRD) techniques.

3.2. Results and discussion

3.2.1 Optimization of electrospinning

Electrospinning as a deposition technique is easily tunable through several parameters such as the concentration of polymer[149–151] or salt[149] in the suspension, the distance between the needle and the collector,[152] the flow rate,[153,154] the applied potential and the time of deposition.[110,155] The relation between electrospinning parameters and final nanofiber

morphology can vary from one report to another. Therefore, it is necessary to establish the basic deposition protocol when approaching a new composition mixture.

The composition of the suspension used in this work is a combination of previous reports from literature that had been applied successfully in the production of indium-tin oxide nanofibers[147] or particles.[156] The weight ratio between water and DMF (1:1) and the PVP content (12 % w/w) proposed by Qi *et al.*[147] were found the most suitable. This solvent ratio enabled for easy dissolution of precursors and the relatively high polymer content ensured the repeatable formation of fibers through the electrospinning process. A Sn/In atomic ratio of 0.16 (recalculated from 15% wt. content of SnO_2) was chosen as it provided the best conductivity for indium-tin oxide particles.[156]

In this work, the final geometric surface area of the electrode material had to be in the range of 1 cm^2. The procedure had to account for the important shrinkage that occurred during calcination, as the layer lost up to 80% of its original size. It was found that 12.5 cm between the needle and the collector plate (combined with 28 cm x 28 cm collector plate) was a distance that regardless of other parameters resulted in a discoid fiber mat with diameter of about 6 cm that reached after calcination a suitable dimension.

The next step was to choose an appropriate flow rate by increasing it incrementally (0.5 µl min^{-1} per electrospinning experiment); using a flow higher than 2 µL min^{-1} resulted in an accumulation of solution as a bubble on the needle tip that occasionally burst and sprayed onto the nanofiber mat, harming the neat and ordered structure. On the other side using a lower speed reduced the mass flow and the deposition of same quantity of material took a longer time. A flow rate of 2 µl min^{-1} was kept for all electrospinning depositions.

The direct result of electrospinning was a mat of nanofibers composed of indium-tin hydroxides and polyvinylpyrrolidone. The samples were then calcined in air at 500 °C. Polyvinylpyrrolidone was burned out and indium and tin hydroxides were converted into oxides. As an illustration of the obtained materials, Figure 3.1A reports SEM images of the fibers prepared at 10 kV after calcination. A neat nanofiber structure was observed, that could be suitable for electrochemistry. The fibers were at least longer than 200 µm, i.e., the largest scale of SEM imaging (data not shown). Nanofibers were not organized and created a structure similar to a mesh. Most of the fibers were straight with a limited curvature. A homogenous deposit was visible through the whole area. Additionally, "beads on a string" defects commonly reported in the literature[113,149] were not present.

As a next step, the optimal voltage had to be defined. A series of electrospinning experiments have been conducted at 7.5, 8.75, 10 and 12.5 kV. Increasing the voltage resulted in thicker nanofibers from about 70 nm at 7.5 kV up to 250 nm at 12.5 kV (measurements after calcination). Indeed, the driving force of electrospinning is the electrostatic attraction of charged particles in the needle to the grounded collector plate. Therefore the higher voltage enabled more suspension to be transferred, leading to thicker fibers after solvent evaporation and calcination.[151]
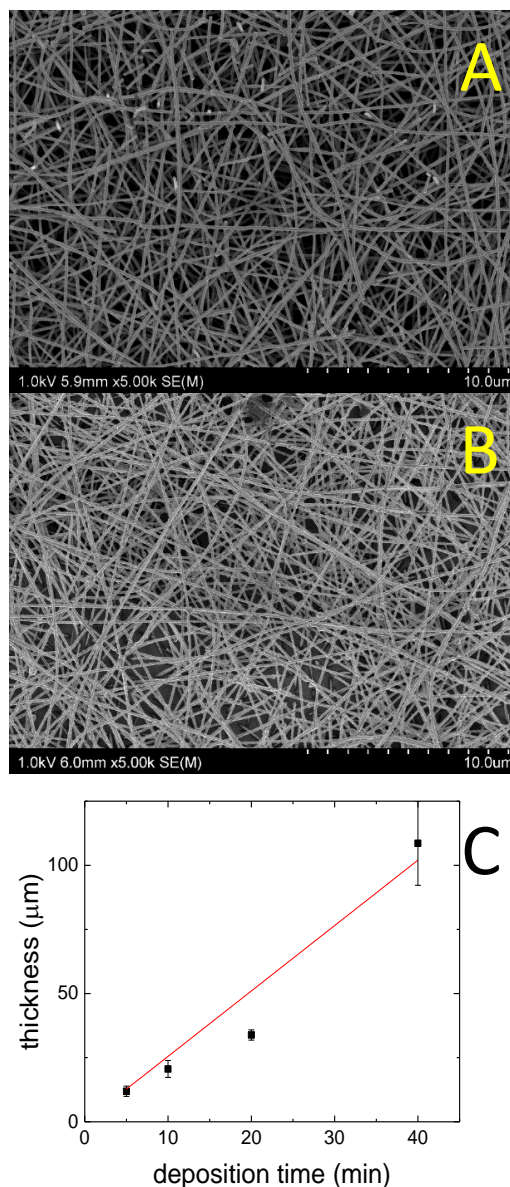
Figure 3.1. Scanning electron microscopy of electrospun ITO nanofibers (A) after calcination at 500 °C and (B) after a thermal treatment at 1000 °C under nitrogen. This material was electrospun at 10 kV for 20 min. (C) Dependence between the deposition time and the thickness of nanofiber layers deposited at 10 kV.

However, the material prepared at 12.5 kV resulted in nanofibers being curvier than those prepared at lower voltage and the film itself had visible macroscopic defects, the layer was not homogenous and some areas were not covered by the fibers. It has been assumed that thin nanofibers could possibly be broken more easily during later treatment and experiments. As a result, 10 kV was chosen for further experiments as it was able to produce the thickest fibers without sacrificing the neat morphology.

Finally, the deposition speed was evaluated. The layer grew about 3 μm min^{-1} in the 5-40 min time range allowing the adjustment of the thickness from 12 μm to more than 100 μm (Figure 3.1C). 20 min deposition was then used in most of the experiments discussed in the next sections.

3.2.2. Electrochemical behavior of calcined ITO nanofibers

A common drawback of nanofibers is related to the polycrystallinity observed for low calcination temperatures that results in a relatively lower conductivity than in thin films.[27] However, one requirement for application of ITO nanofibers in electrochemistry is that the electrode provides a suitable conductivity. The optimal material prepared by electrospinning at 10 kV for 20 min and calcined at 500 °C in air (so-called 500Air) was immobilized on a scotch tape for characterization. In these conditions, a sheet resistance of 4.5 ± 0.05 kΩ sq^{-1} was measured, which is about 100 times higher than the conductivity reported for ITO electrodes (10-50 Ω sq^{-1}).[21]

The electrochemical properties of ITO materials were here evaluated by cyclic voltamperometry (CV) of dimethanolferrocene (Figure 3.2). In this experiment the potential of the working electrode was scanned at 50 mV s^{-1} between -0.2 V to 1.2 V vs Ag/AgCl 3 M reference electrode. When the CV was performed with a commercial ITO film electrode with low resistivity (22 Ω sq^{-1} using the same method of measurement as for nanofiber electrodes), well defined peaks of current were observed at 0.342 V and 0.183 V for oxidation and reduction reactions, respectively (Figure 3.2A). The difference of potential between these two peaks was 0.159 V which correspond to a pseudo reversible electrochemical signal and the redox potential was 0.26 V vs Ag/AgCl. Peak currents were in the range of 120 μA.

The same experiment on the ITO nanofiber sample 500Air led to much worse electrochemical response. The high resistivity of the electrode material did not prevent the electrochemical experiment to be performed, however the oxidation was observed at more positive potential, around 1V, was poorly defined and the current was at least 5 times lower on the nanofibers
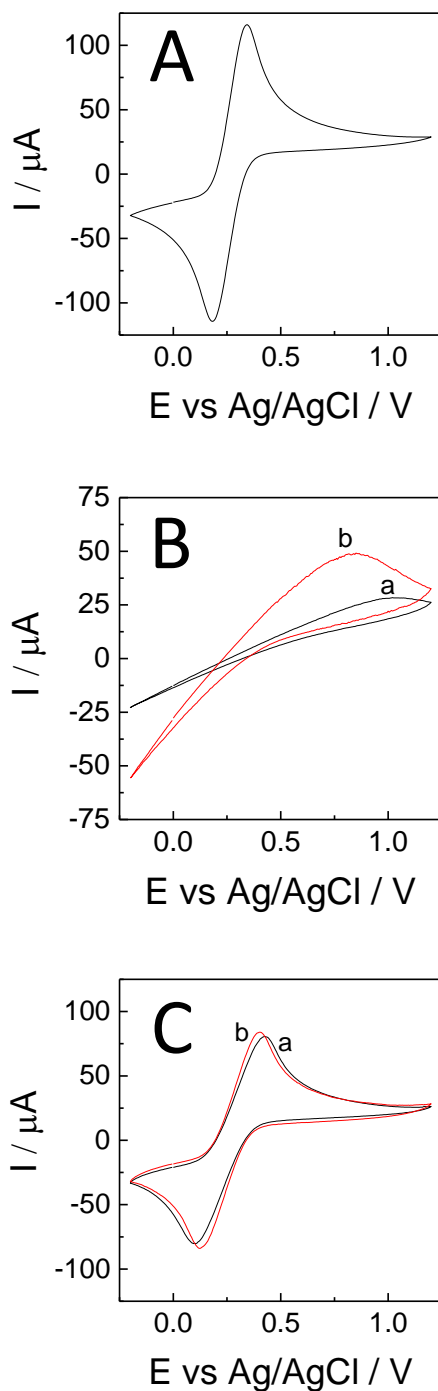
Figure 3.2. *Cyclic voltamperograms of 5 mM dimethanolferrocene on (A) commercial flat ITO electrode, (B) ITO nanofiber layers treated at 500 ° C (a, black) in air 500Air (no thermal treatment), (b, red) 500N$_2$ (thermal treatment in 500 °C under nitrogen), (C) ITO nanofiber layers (a, black) 1000Air (thermal treatment in 1000 °C in air) and (b, red) 1000N$_2$ (thermal treatment in 1000 °C under nitrogen). Fibers were electrospun at 10 kV for 20 min. Electrolyte was 0.1 M KCl in water and scan rate was 50 mV s^{-1}. Electrode area was equal to 12.6 mm^2.*

than on ITO film electrode. Moreover no reduction signal could be measured. The electrochemistry of dimethanolferrocene on ITO nanofiber calcined at 500 °C was thus irreversible. Such electrode is basically unsuitable for any electrochemical experiment, no matter the application. Therefore, different post-treatments had to be explored in order to increase the conductivity and the reactivity of the electrospun ITO nanofibers.

3.2.3. Thermal treatment of ITO nanofibers

There are already several reports in the literature dealing with the question of conductivity of porous ITO. Gross *et al.* show that a higher temperature treatment, up to 1000 °C can result in reducing resistivity of porous ITO up to one order of magnitude.[23] In our case, sintering might increase the grain size, reducing the volume of grain boundaries that dampen the conductive properties and most importantly make connections between neighboring nanofibers. Using inert or reductive atmosphere is another strategy that is used to tackle the problem of high resistivity.[38,70,117] It has been postulated that annealing under nitrogen introduces oxygen vacancies and results in a higher charge carrier concentration that increases conductivity.[157] The helpful effect of increased calcination temperature has also been shown using nitrogen atmosphere.[156]

In this work, we have evaluated the influence of both nitrogen atmosphere and high temperature on the conductivity of the electrodes. All ITO nanofibers have been calcined first at 500 °C in air (500Air) before to be treated for 1h at 500 °C under N_2 (500N_2), 1000°C in air (1000Air) or 1000 °C under N_2 (1000N_2), and their resistivities were estimated (see Table 1). Our investigations confirm the information from the literature. A treatment under N_2 atmosphere at 500 °C (500N_2: 0.9 ± 0.05 kΩ sq^{-1}) or a treatment at 1000°C in air (1000Air: 0.42 ± 0.01 kΩ sq^{-1}) led to a lower resistivity than the original sample (500Air: 4.5 ± 0.05 kΩ sq^{-1}). The lowest resistivity was finally obtained by combining these two conditions by treating the fibers at 1000°C under nitrogen atmosphere (1000N_2: 0.25 ± 0.01 kΩ sq^{-1}). The low magnification SEM picture is also included (Figure 3.1B) to confirm that no major change in the macroscopic morphology of the fiber mat happened after the thermal treatment. High magnification SEM pictures were also taken of these different samples (Figure 3.3). By comparison with the fibers only calcined in air at 500 °C (Figure 3.3A, Ø=130 ± 21 nm), the morphology of the fibers was not affected by the treatment at 500 °C under N_2 (Figure 3.3B, Ø=132 ± 21 nm), but the sintering at 1000 °C induced an increase in the roughness of the fibers and a slight decrease of their diameters (Figure 3.3C, Ø =125 ± 12 nm in air, Figure 3.3D, Ø =123 ± 12 nm under nitrogen).
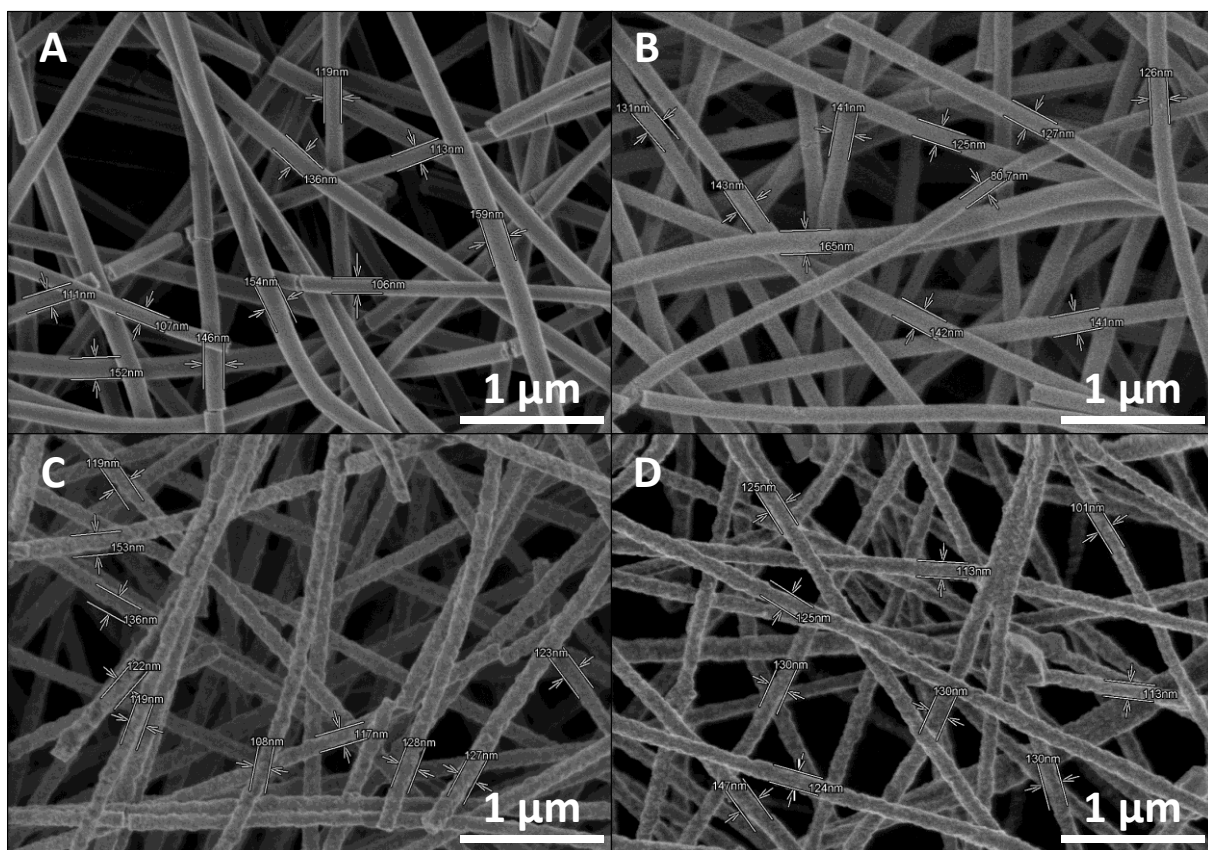
Figure 3.3. *Scanning electron microscopy of ITO nanofibers (A) 500Air (no thermal treatment), (B) 500N$_2$ (thermal treatment in 500 °C under nitrogen), (C) 1000Air (thermal treatment in 1000 °C in air) and (D) 1000N$_2$ (thermal treatment in 1000 °C under nitrogen). Fibers were electrospun at 10 kV for 20 min.*

The consequence of that treatment on electrochemistry was dramatic. Figure 3.2B reports the CV in the presence of dimethanolferrocene with the sample treated at 500 °C, and Figure 3.2C the response of those treated at 1000 °C. The electrochemical response after treatment at 500 °C under N$_2$ was slightly better than the sample simply calcined (500Air) as shown by the increase in the oxidation current up to 50 µA and by the displacement of the oxidation potential toward a lower value, at about 0.85 V (Figure 3.2B, curve b). However the electrochemical response was still irreversible and much worse than on ITO film. The electrochemical behavior was then largely improved upon treatment at 1000 °C, in air (Figure 3.2C, curve a) or under nitrogen (Figure 3.2C, curve b). Indeed, the electrochemical response became pseudo-reversible, characterized by peak potential differences of 0.335 V and 0.280 V for 1000Air and 1000N$_2$, respectively. The measured peak currents were similar for both electrodes, in the range of 80-90 µA, still slightly lower than for the commercial ITO film electrode.

Figure 3.4 shows the structural characterization of our samples performed by X-ray diffraction (XRD). A summary of data gathered on nanofiber layers treated in different conditions has been given in table 3.1 Signals for both indium oxide In_2O_3—JCPDS#01-089-4595—and tin oxide SnO_2—JCPDS#01-072-1147—have been identified, proving a successful transition of electrospun indium-tin-hydroxide@polyvinylpyrrolidone composite into pure indium tin oxide. Average crystallite size of In_2O_3 was increased significantly during the thermal treatment between 500 and 1000 °C in air from 10 nm to 21 nm. The treatment at 1000 °C under nitrogen allowed an additional growth of the crystallite size up to 29 nm, which is consistent with previous reports from the litterature.[158] Here, it is suggested that under nitrogen atmosphere ITO became less saturated with oxygen, allowing for more flexible reorientation of domains and growth of bigger crystallites. And it is assumed that a direct correlation exists between this crystallite size and both the resistivity and the electrochemical properties discussed before.

Table 3.1. Sheet resistance, fiber diameter, average crystallite size and dimethanolferrocene oxidation peak currents of 20 min deposited nanofiber layers after different thermal treatment. Sample 500Air did not undergo additional thermal treatment. Other samples, $500N_2$, 1000Air and $1000N_2$ were thermally treated accordingly in 500 °C under nitrogen, in 1000 °C in air and in 1000 °C under nitrogen. Peak currents for samples 500Air and $500N_2$ were only roughly estimated since the peaks were not well defined.

Sample	Sheet resistance (kΩ sq^{-1})	Fiber diameter (nm)[b]	Crystallite size (nm)[c]		Dimethanol-ferrocene ox. peak current (μA)	SnO_2:In_2O_3 ratio[c]
			In_2O_3	SnO_2		
500Air[a]	4.5 ± 0.05	130 ± 21	10.0 ± 0.2	76 ± 19	~25	10.1
$500N_2$[a]	0.9 ± 0.05	132 ± 22	10.5 ± 0.5	72 ± 16	~50	10.1
1000Air[a]	0.42 ± 0.01	125 ± 12	21 ± 1	86 ± 26	78	3.5
$1000N_2$[a]	0.25 ± 0.01	124 ± 12	29 ± 1	73 ± 16	85	2.7
1000Air*	-	-	23 ± 1	31 ± 4	-	0.26
$1000N_2$*	-	-	28 ± 2	54 ± 3	192	0.32

[a] Sample immobilized on tape. * Sample immobilized on glass with $SnCl_4$.

[b] Determined by SEM.

[c] Determined by XRD.

On the opposite, average crystallite size of SnO_2 was here only slightly affected by the conditions of thermal treatment and no clear trend was found. It is worth underlining that the relative intensities of SnO_2 diffraction peaks were either too big or too small, for example peak at 26.5° was very large while peak at 33.8° that should possess about 80% of the intensity of the former was barely visible (Figure 3.4A). Obviously, the average crystallite sizes of SnO_2 were dependent of (hkl) planes, for example the peak (110) at 26.5° evidenced a crystallite size of 110 nm, while the peak (200) at 37.9° led to a size of 60 nm. These data reveal a preferred orientation of the SnO_2 crystallites—along <110> direction. X-ray diffractogramms analysis also revealed that the apparent SnO_2/In_2O_3 ratio was strongly dependent on the thermal treatment. It yielded to 10.11 for 500Air and 500N_2, and 3.54 and 2.70 for 1000Air and 1000N_2, respectively. However, the chemical analysis performed by energy-dispersive X-ray spectroscopy show that the chemical composition of the same nanofiber was in the range expected from the ratio between tin and indium salts in the starting suspension (Sn/In = 0.16). In XRD experiments, the measured peak intensities depend on the orientation and morphology of crystallites. The unexpected results reported here are thus a consequence of the method used to prepare these samples. Pressing of the fiber mat to a scotch tape induced a preferential orientation of the nanofibers in the plane of the substrate.
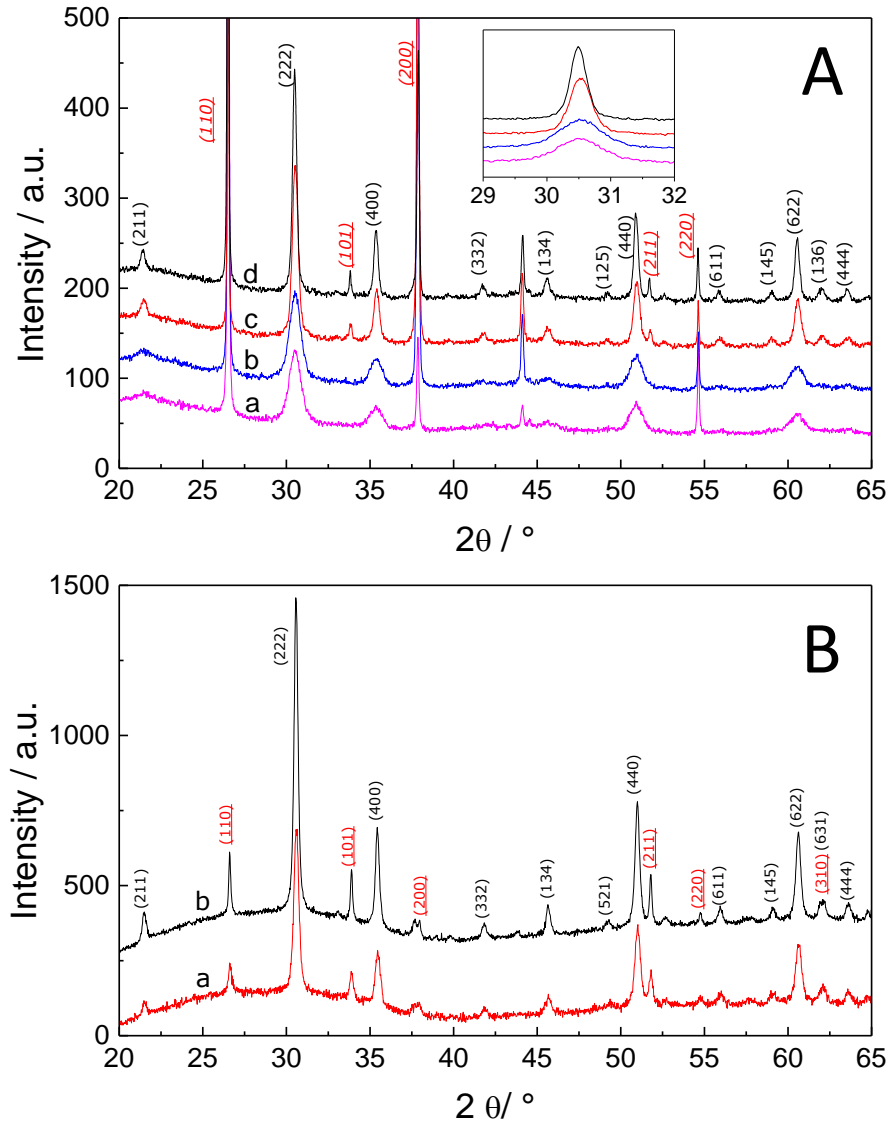
Figure 3.4. (A) X-ray diffractograms of ITO nanofibers immobilized with tape (a, pink) 500Air (no thermal treatment), (b, blue) 500N$_2$ (thermal treatment in 500 °C under nitrogen), (c, red) 1000Air (thermal treatment in 1000 °C in air) and (d, black) 1000N$_2$ (thermal treatment in 1000 °C under nitrogen). On all images SnO$_2$ peaks were labeled in red and In$_2$O$_3$ in black. In the inset a small portion of diffractogram presenting most intense peak of In$_2$O$_3$ is pictured. Inset shares x and y axis description with main graph. (B) X-ray diffractograms of ITO nanofibers immobilized with SnCl$_4$ (a, red) 1000Air (thermal treatment in 1000 °C in air) and (b, black) 1000N$_2$ (thermal treatment in 1000 °C under nitrogen). All fibers were electrospun at 10kV for 20 min.

3.2.4. Immobilization of the electrospun nanofibers with SnCl$_4$

Another method of immobilization of the nanofiber mats involves their gluing on a glass plate with a SnCl$_4$ ethanol solution[17] (Figure 3.4B). Unfortunately, this approach did not allow immobilizing samples 500Air and 500N$_2$ as they were rapidly dissolved by the immobilizing solution. It is possible that it happened due to very low grain size, around 10 nm for the main phase In$_2$O$_3$ (Table 1), making samples more soluble in contact with a solvent. Similar dependency of solubility on crystallinity has been already reported for a different class of materials.[159] Figure 3.5A shows a SEM picture of a sample prepared by this method. Despite the presence of an additional material on the fibers that was not observed before (compare Figure 3.5A with Figures 1.4D), that can be probably ascribed to the formation of tin hydroxides, the porosity of the nanofiber assembly did not seem to be dramatically affected.
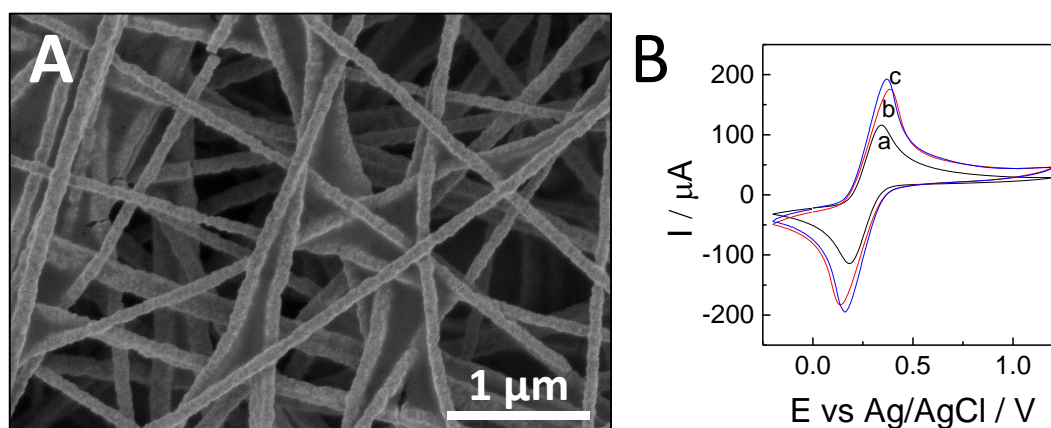
Figure 3.5. *(A) Scanning electron microscopy of ITO nanofibers immobilized with SnCl$_4$. (B) Cyclic voltammograms of 5 mM dimethanolferrocene with (a, black) regular flat ITO electrode, and with electrospun nanofibers at 10 kV for (b, red) 5 and (c, blue) 20 min. All these fibers were thermally treated at 1000 °C under nitrogen before analysis. Electrolyte was 0.1 M KCl in water and scan rate was 50 mV s^{-1}. Electrode area was equal to 12.6 mm^2.*

XRD was performed on samples immobilized with SnCl$_4$ (1000Air* and 1000N$_2$*, Figure 3.4B and Table 1). These measurements confirmed that a sample treated under nitrogen (1000N$_2$*, 28.3 nm) display bigger In$_2$O$_3$ crystallite size than a sample treated in air (1000Air*, 23.0 nm). SnO$_2$ crystallite sizes (31 and 54 nm for 1000Air* and 1000N$_2$*, respectively) were found smaller than for the previous series of experiment (between 72 and 86 nm). And the SnO$_2$:In$_2$O$_3$ ratio (0.26 and 0.32) were found very close to the theoretical one

(Sn/In =0.16). Thus, in these conditions the preferential orientation of the fiber observed before has been strongly attenuated.

The mode of immobilization had also a consequence on the electrochemistry of these nanofibers. Figure 3.5 reports the cyclic voltamperometry on commercial ITO electrode (curve a) and 5 (curve b) and 20 min (curve c) deposited ITO nanofibers that were immobilized with SnCl$_4$. These nanofibers were treated at 1000°C under nitrogen for 1 h before use. As reported in the previous section, redox process was pseudo-reversible at all electrodes. What is interesting is the increase of redox current for both 5 and 20 min electrospun nanofiber layers (peak currents 178 µA and 192 µA respectively) compared to flat ITO (peak current 126 µA) that occurs despite the process in theory being limited only by diffusion. The reason for that might be the relatively big thickness of our layers (between 12 and 35 µm) making the volume of solution accessible to electrochemistry bigger, and thus the quantity of electroactive species involved in the reaction higher. This behavior of reversible diffusion-limited probes on macroporous electrodes with high surface area has already been observed before.[160,161]

Clearly, the method involving gluing with SnCl$_4$ (Figure 3.5B) was superior to the immobilization on a tape (Figure 3.2 B & C) as it resulted in the absence of preferential orientation of the nanofibers and a higher electrochemical response. It is also possible that pressing the nanofibers onto a tape damaged some nanofibers leaving some parts of the electrode inactive. Therefore the experiments discussed in the following sections have been performed after immobilization of the nanofiber on a glass substrate using SnCl$_4$.

ITO nanofibers have been prepared by electrospinning a suspension of polyvivnylpyrrolidone and indium and tin salts. The treatment of these fibers at 1000 °C under nitrogen allows to get a conductive materials composed of indium and tin oxides. The fibers can be used for electrochemistry; the best electrochemical response being obtained when the fiber mats were immobilize on a glass surface with SnCl$_4$. Next sections will evaluate the interest of the ITO nanofibers for (1) electroanalysis, by studying the electrochemical detection of ascorbic acid and (2) for spectroelectrochemistry, by following the spectroelectrochemical response of Prussian blue.

3.2.5. Application to the electrochemical detection of ascorbic acid

Ascorbic acid is an important target in electroanalysis and the field of its electrochemical detection is still growing. The L-enantiomer is commonly referred to as vitamin C and it

interacts in many biochemical processes like synthesis of proteins, metabolism of folic acid, tyrosine and tryptophan and acts as a cofactor for several enzymes.[162] Contrarily to dimethanolferrocene, ascorbic acid is more difficult to detect electrochemically as shown in curve a of Figure 3.6A. The experiment has been performed on a commercial ITO film electrode. The electrochemical oxidation of ascorbic acid was poorly defined, with a peak potential at 0.89 V versus Ag/AgCl and a peak current of about 110 µA. This reaction was irreversible as no reduction signal was detected. The same experiment was then performed with fibers mats deposited for 5 (curve b, Figure 3.6A) and 20 min (curve c, Figure 3.6A). Two effects can be discussed. First, it has been observed that the peak current intensity was increasing dramatically when ITO nanofibers were used in place of the flat ITO electrode and that the current was increasing with the thickness of the fiber layer, 214 µA for fibers deposited for 5 min (12 µm) and 254 µA for the thickest material prepared by 20 min electrospinning (35 µm). The electrochemical detection of ascorbic acid was thus highly reliant on the surface of the electrode. These results confirm that indeed the electroactive surface area of ITO nanofiber layers was bigger than the flat ITO electrode and that it increased with thickness of the nanofiber layer.

Another interesting fact was that of improved oxidation potential of ascorbic acid from 0.89 V on flat ITO to 0.72 V (thin layer) and 0.55 V (thick layer). The higher the surface area, the lower the oxidation peak potential. The shape of the oxidation signal is also dramatically modified, from a rather irregular signal on flat electrode to a well-defined peak similar to the one observed before with dimethanolferrocene oxidation (Figure 3.5B), leading to oxidation currents in the same range for the same concentration (1 mM). The electrochemical detection was not limited anymore by the reactivity of the electrode as observed on flat ITO but was limited by the diffusion of the probes toward and inside the electrode material. As such, the electrode material we have prepared can be applied to electroanalytical determination of ascorbic acid. Figure 3.6B shows the electrochemical response of the thick ITO nanofiber electrode to growing concentrations of ascorbic acid. A sensitivity of 1.04 mA mM^{-1} cm^{-2} was determined (Inset of Figure 3.6B), which is much better than the sensitivity measured previously on high-surface area indium-tin oxide surfaces 0.2 mA mM^{-1} cm^{-2}.[163]
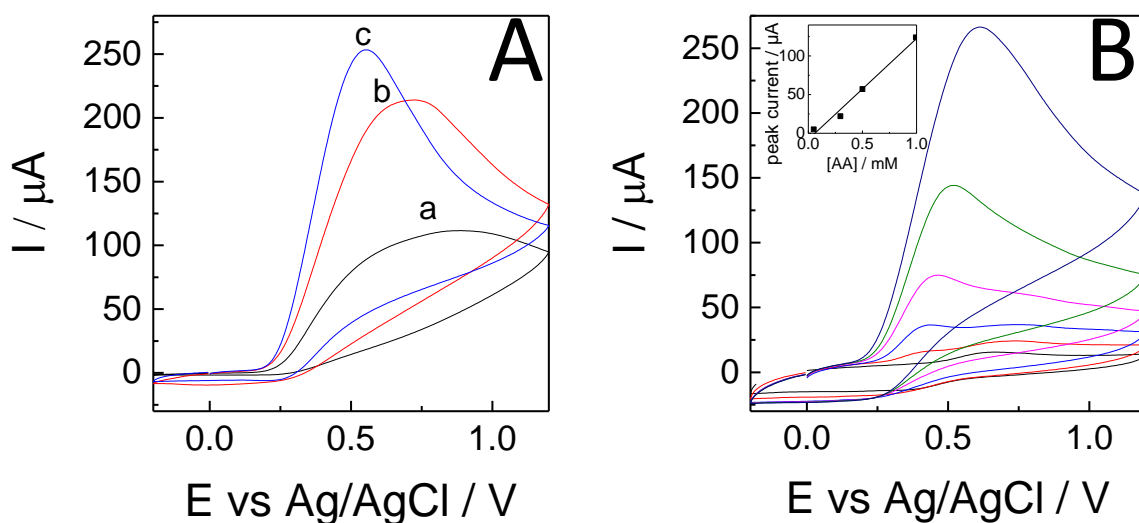
Figure 3.6. (A) Cyclic voltamperograms of 5 mM ascorbic acid in 0.1 M KCl in water with (a, black) regular flat ITO and nanofibers electrospun at 10 kV for (b, red) 5 and (c, blue) 20 min. (B) Cyclic voltammograms of ascorbic acid in rising concentrations: (black) 0 mM, (red) 0.05 mM, (blue) 0.3 mM, (pink) 0.5 mM, (green) 1 mM and (dark blue) 3 mM in 0.1M KCl in water on a nanofiber layer electrospun for 20 minutes at 10 kV and thermally treated at 1000 °C under nitrogen. Inset: corresponding calibration curve. The scan rate was 50 mV s^{-1} for all measurements. Electrode area was equal to 12.6 mm^2.

3.2.6. Application to spectroelectrochemistry

One interest of ITO concerns the development of transparent electrode. Directly after electrospinning, the nanofiber mats were not transparent and had a white color. They acquired a yellowish tint after 500 °C in air. This tint was then fully removed only after treatment at 1000 °C under nitrogen. However, these nanofibers display only poor transparency in air as shown in Figure 3.7, curve a. Only 6% and 1 % of light were transmitted at 800 nm and 400 nm, respectively. The transmittance of the glass substrate is plotted for comparison in curve c of Figure 3.7 that shows that more than 90 % of the light could be transmitted over the all visible spectrum in the absence of nanofibers.
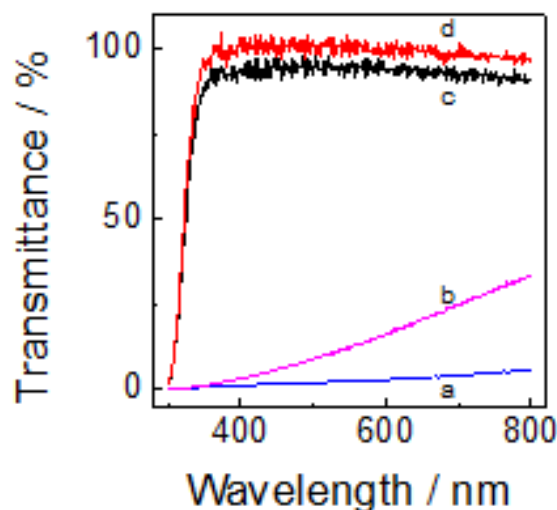
Figure 3.7. *Transmittance spectrum for (a&b) ITO nanofibers and (c&d) glass plate. Samples (a) and (c) were obtained in air in a dry state, while samples (b) and (d) were obtained in water. ITO nanofibers were deposited at 10 kV for 20 min (about 34 µm) and thermally treated at 1000 °C under nitrogen.*

The nanofibers deposited on glass substrate have been then tested in the presence of water. In this case the transparency was improved, reaching 35% at 800 nm and 3% at 400 nm (to be compared with more than 95% at 800 and 400 nm for the wet glass substrate). We believe that the enhanced transparency of the wetted samples comes from the low difference of refractive indices (*n*) between water and ITO nanofibers. It has been already noticed in literature that refractive index of ITO is dependent on its porosity[137] and that matching refractive indices of indium tin oxide with surrounding environment can reduce Fresnel reflection that is responsible for the loss of transparency.[164] Knowing that the value of *n* for air is close to 1 and 1.33 for water, one can conclude the resultant refractive index of the prepared ITO nanofiber is closer to 1.33 which is consistent with previous reports on ITO with high porosity (50-80%) displaying *n* of 1.2-1.4.[137] The ITO nanofiber layers can be thus used in spectroscopic studies in the visible light range. Considering that the fibers also display excellent electrochemical properties, it should be possible to combine the two properties for spectroelectrochemical measurements.

Prussian blue has been chosen for this demonstration.[165] For this experiment, the electrospun nanofiber mat was first immobilized on the flat ITO plates with using the $SnCl_4$. Prussian blue was then deposited electrochemically by applying 0.5 V to the electrode for 60 s

in a solution containing both $FeCl_3$ and $Fe(CN)_6^{3-}$. High-resolution SEM characterization performed after deposition of Prussian blue show that the modification is homogeneous and conformal (Figure 3.8A). The modified fibers are thicker (Ø ~ 180 nm) than the unmodified fibers (Figure 3.5A, Ø ~120). The thickness of this Prussian blue film was about 30 nm.
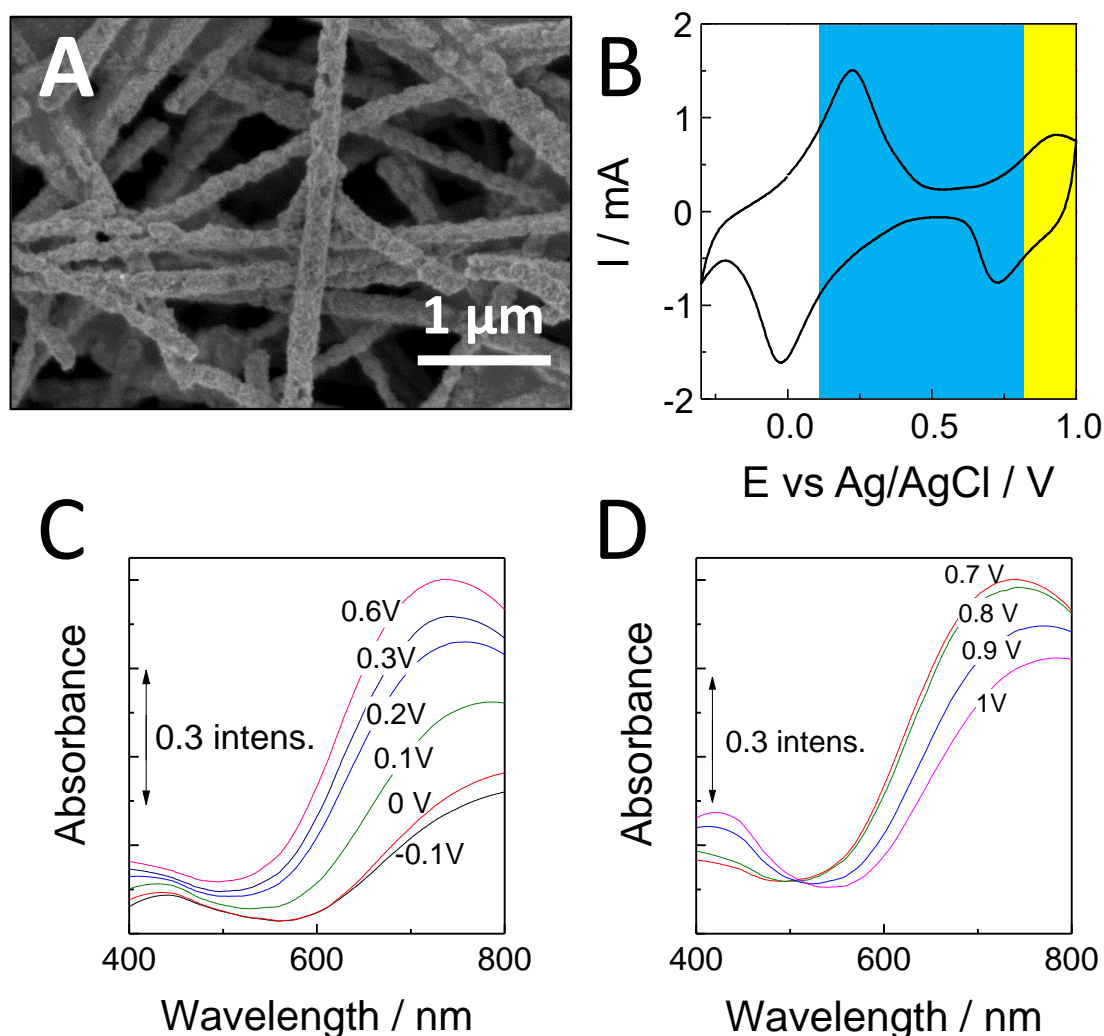
Figure 3.8. *(A) Scanning electron microscopy of ITO nanofibers after electrodeposition of Prussian blue. (B) Cyclic voltammogram of Prussian blue-covered ITO nanofibers in 0.1M KCl and 0.01 M HCl in water with approximate regions of existence of different Prussian blue forms marked (white, blue and yellow) done with scan rate of 50 mV s^{-1}. Absorbance spectra as a function of the applied potential measured with Prussian blue modified ITO nanofibers: (C) from -0.1 V to 0.6 V and (D) from 0.7 V to 1 V. The fibers were electrospun at 10 kV for 20 min and thermally treated at 1000 °C under nitrogen. Electrode area was approximately 60 mm^2.*

Spectroelectrochemical characterization was then performed in a solution of 0.1 M KCl and 0.01 M HCl. Figure 3.8B shows the cyclic voltamperogram measured at 50 mV s^{-1}. Two redox pairs were clearly observed at 0.1 V and 0.8 V, corresponding to the different redox state of Prussian blue by successive reduction and oxidation of the iron metal centers. Just after modification of the ITO nanofibers with Prussian blue, the open circuit potential of the electrode was about 0.6 V at which the Prussian blue has a major absorbance spectra peak at 720 nm (Figure 3.8C). The stepwise scanning of the potential from 0.6 to -0.1 V induced the diminishment of the absorbance as Prussian blue was transformed into the colorless form, Prussian white. The stepwise scanning of the electrode potential up to 1 V induced then another transition to Prussian yellow characterized by a decrease of absorbance at 720 nm and the appearance of a small peak at 420 nm (Figure 3.8D). These changes were reversible and repeatable. Spectroelectrochemical experiment has been successfully performed with electrospun ITO nanofibers.

3.3. Conclusions

Nanofibers with diameter ranging from 110 to 235 nm have been prepared by electrospinning a suspension of polyvivnylpyrrolidone and indium and tin salts. Their thermal treatment at 1000 °C under nitrogen led to conductive nanofiber mats composed of indium and tin oxides. The ITO nanofibers can be applied to electrochemistry as demonstrated with experiments performed in the presence of dimethanolferrocene. The nanofibers have been successfully applied to electroanalytical determination of ascorbic acid, with a sensitivity of 1.04 mA mM^{-1} cm^{-2}, and to spectroelectrochemistry using Prussian blue as a proof of concept.

Chapter 4. Indium tin oxide nanofilament layers and their potential applications in electrochemistry and spectroelectrochemistry

4.1. Introduction

Optically transparent electrodes (OTEs) are the subject of numerous researches in recent years. Large areas of industry have benefitted from developments in that field and led to commercial applications, most notably for the production of liquid crystal displays and touch-screens in smartphones.[20] Other emerging applications are organic light emitting diodes,[21] dye-sensitized solar cells,[22] and sensors based on spectroelectrochemical detection.[3,7]

Spectroelectrochemistry as the name suggests is the combination of an electrochemical experiment with a spectroscopic experiment, in most cases UV-Vis, IR, Raman spectroscopies or electron paramagnetic resonance and more rarely XRD or NMR.[1] Thanks to recent commercialization of affordable and portable UV-Vis spectrometers, coupling this spectroscopy with electrochemistry for spectroelectrochemical detection[134] is an interesting direction for the development of more selective chemical sensors, taking advantage of both electrochemical and spectroscopic selectivity in a single device.

As it stands now, indium tin oxide (ITO) is the most commonly used material for OTEs due to its excellent physical properties like high conductivity and transparency.[33] The technologies of producing ITO thin films are now well established.[166] Nowadays, the research needs are towards the development of new methods of producing robust porous transparent electrodes for photoconversion[16,141] and analytical applications.[94] The fabrication of mesoporous ITO layers with high surface areas[54,64,70] or macroporous ITO layers with very good diffusional access to the inner surface area of the pores has been described.[72,145,146] Macroporous electrode materials are preferred for some applications, including sensors, as it enables mass transport in even very thick layers (up to 900 μm in an example related to Li-ion secondary battery[167]), and can be further modified with a functional material to increase the active surface area or provide catalytic activity.[143] Different methods are reported for the preparation of porous ITO materials, e.g. infiltration[146], electrochemically assisted deposition[145], electrophoretic deposition[72] or electrospinning[27,108–111,114,115,117,147]. Electrospun materials are very attractive because a sensitive layer (e.g., a photosensitive or a preconcentration film) can

be deposited on the surface of nanofibers without clogging the large interconnections between pores, keeping the all surface area of the electrode accessible.

Pioneering reports on supported ITO nanofibers from electrospinning have dealt mainly with preparation and characterization of thin layers by direct deposition on the substrate of few layers of nanofibers (typically one to three), i.e., between 200 to 300 nm thickness.[108,115] The first integration of ITO nanofibers in a photovoltaic device has been described by Iskandar *et al.*,[111] and it appeared then clearly that a strategy should be developed to prevent delamination of the fibers from the substrate in order to efficiently utilize them. In that work, the authors proposed the precasting of the precursor solution on to the target substrate. Another strategy for immobilizing the nanofibers on the substrate was chosen by Jin *et al.* that resulted in much thicker films, i.e. more than 2.5 μm, by applying a layer of poly-ethylene glycol onto the electrospun nanofibers before their final calcination.[27] Both methods require using a conductive substrate (ITO or fluorine-doped tin oxide, FTO) and ITO nanofibers serve only as a kind of functionalizing layer. This limits their potential, notably because high-temperature treatment cannot be used to enhance the electronic properties of these indium tin oxide nanofibers.[23]

Ostermann *et al.* worked on similar material, antimony tin oxide, and because of those difficulties, they could conclude that it was impossible to obtain continuous oxide nanofibrous layers of significant thickness by direct deposition on the solid substrate, due to inevitable breaking of fibers and delamination of the layer.[17] For that reason, some of the early reports[109,110] as well as all of the later applications of ITO nanofibers have been performed using free-standing mats.[114,117,147] Unfortunately, the brittleness of those materials makes the procedure still quite difficult to enforce and using it as sensing layer or in large-scale applications remains challenging.

With those problems in mind, a protocol was devised to produce a robust macroporous indium tin oxide layer, by electrospinning the fibers on a fused silica substrate covered with polystyrene before their thermal treatment. This chapter describes in detail that original protocol and provides structural (SEM and XRD) and physicochemical (electrochemistry and transparency) characterizations of the resulting material. The porous ITO electrode has then been modified electrochemically with mesostructured methylated silica in order to increase the available surface area and applied to combined electrochemical and spectral detection of industrial dyes (methylene blue, Meldola's blue and methylene green).

4.2. Results and discussion

4.2.1. Electrospun material characterization

Right after the electrospinning procedure, the obtained material is a composite of indium tin hydroxide and polyvinylpyrrolidone (PVP) that is quite flexible, but it is neither conductive nor transparent. The layer is also readily solubilized by any polar solvent (mainly due to the solubilization of PVP, the stabilizing polymer). Calcination is needed to convert this composite material into indium tin oxide. The goal of the work presented in this chapter is to immobilize the electrospun ITO nanofibers in one step on a fused silica substrate. For that reason a polystyrene (PS) coating is used to bypass the problem of shrinking by providing a layer that liquefies at the adequate moment to avoid breaking of ITO during calcination. PS is drop-coated on the substrate. The thickness of this mediating layer is about 250 μm. The melting point of PS (ca. 250 °C depending on tacticities[168]) is lower than the onset of PVP decomposition (360 °C[109]). In this way, nanofibers are allowed to shrink without breaking and PS is burned out only at the end of the process (starting from ca. 410 °C[169]). All those steps happen sequentially upon heating up to 500°C with a temperature ramp of 100 °C h^{-1}. Figure 4.1A shows a photograph of the nanofibers deposited on fused silica, before their calcination.
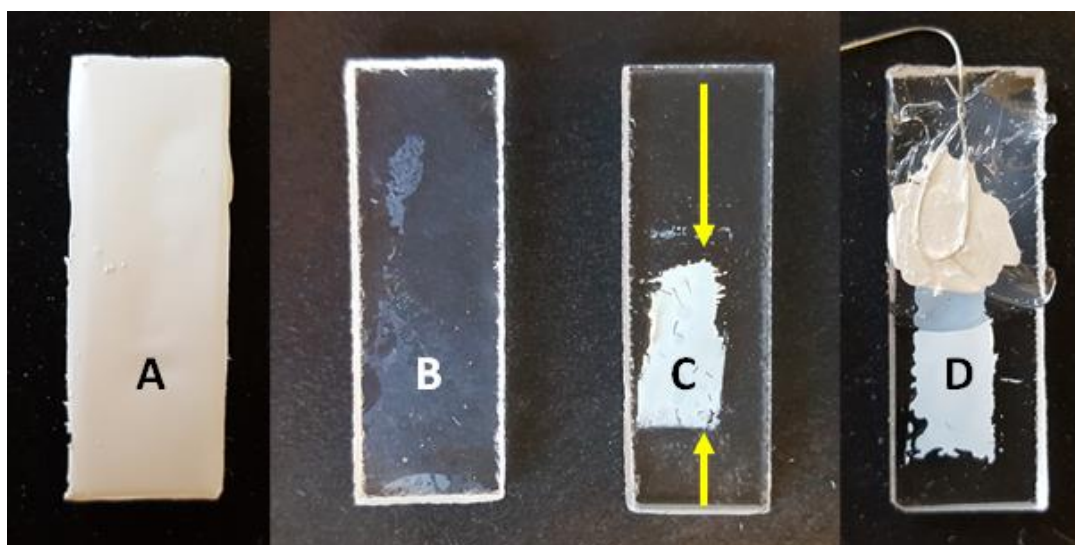
Figure 4.1. Photographs of (A) as-spun nanofibers on fused silica, (B&C) similar samples after calcination (B) without and (C) with using a mediating polystyrene film, (D) sample after insulation of the electrical connection. The yellow arrows indicate the important shrinkage observed during this calcination. Here, all samples are presented in a dry state.
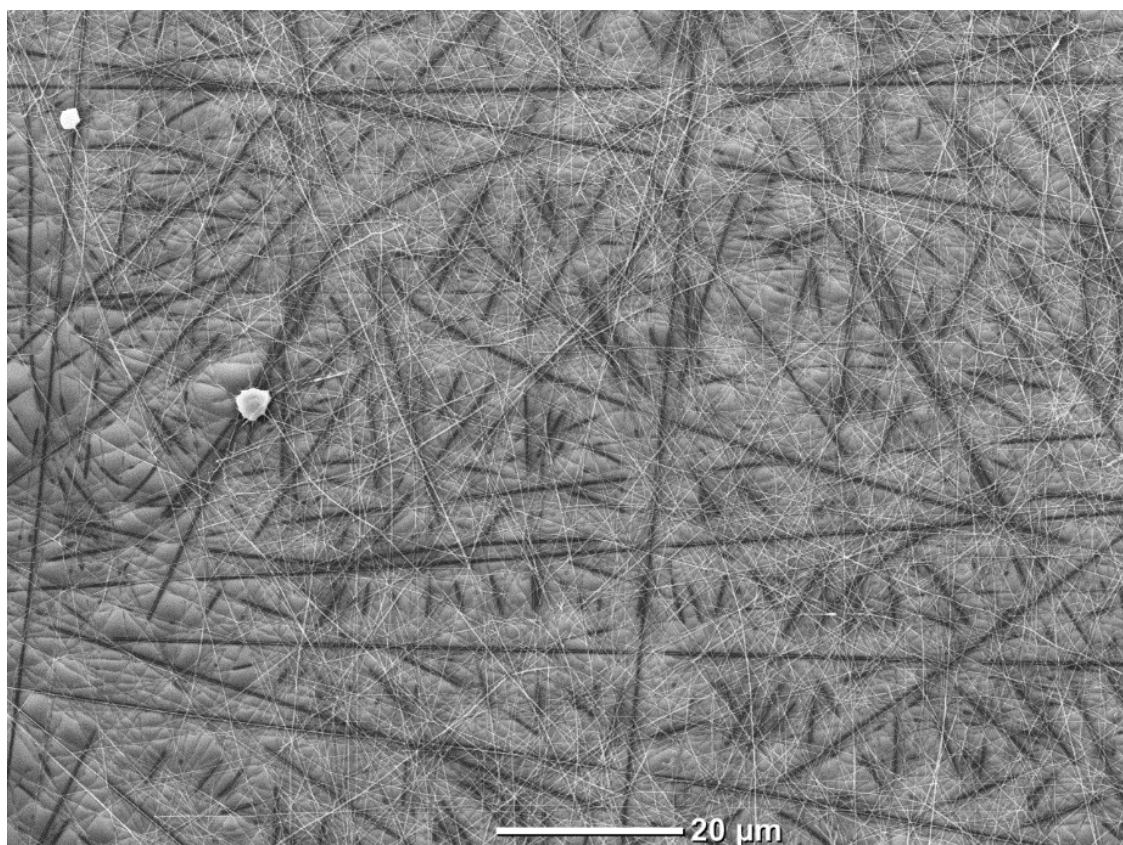
Figure 4.2. – *Scanning electron microscope image of calcinated ITO nanofibers prepared without mediating polystyrene film (this sample is shown in picture B of Figure 4.1).*

The entire surface of the substrate is covered. After calcination in the absence of the PS coating on the fused silica, only a few thin visible patches of thin and sparse deposits are observed (Figure 4.1B). A SEM picture of this sample is also reported in Figure 4.2 that confirms the limited number of fibers remaining on the fused silica surface. On the contrary, when calcination is performed in the presence of the PS coating, a thick layer is obtained, whose geometric surface area is decreased by a factor of about 4 (see Figure 4.1C), due to free shrinking of the ITO nanofibers on the substrate. SEM images (x1000 magnification) of electrospun nanofibers at different stages of processing are presented in Figure 4.3. As-spun material forms a neat structure composed of nanofibers, up to 30 µm long (Figure 4.3A), a drastic change in the morphology occurred during calcination at 500°C, as evidenced when we compare Figure 4.3A and 4.3B. The integrity of the layer is preserved with only small cracks observed. A denser layer is formed and it is no more possible at that magnification to distinguish individual nanofibers. Comparison of Figures 4.3B and 4.3C indicates that the macroscopic structure of the layer does not change significantly after an additional treatment at 1000°C in nitrogen. However, more details emerge on the SEM image, possibly due to

higher conductivity of the layer treated at high temperature (the electrode resistance is lowered from ca. ~30 kΩ*sq^{-1} after 500°C treatment to ca. ~200 Ω*sq^{-1} after 1000°C treatment). Small amount of bead-like structures (ca. 500 nm in diameter) are observed. The thickness of the layer, measured by profilometry, was about 2.5 µm (see Figure 4.4).
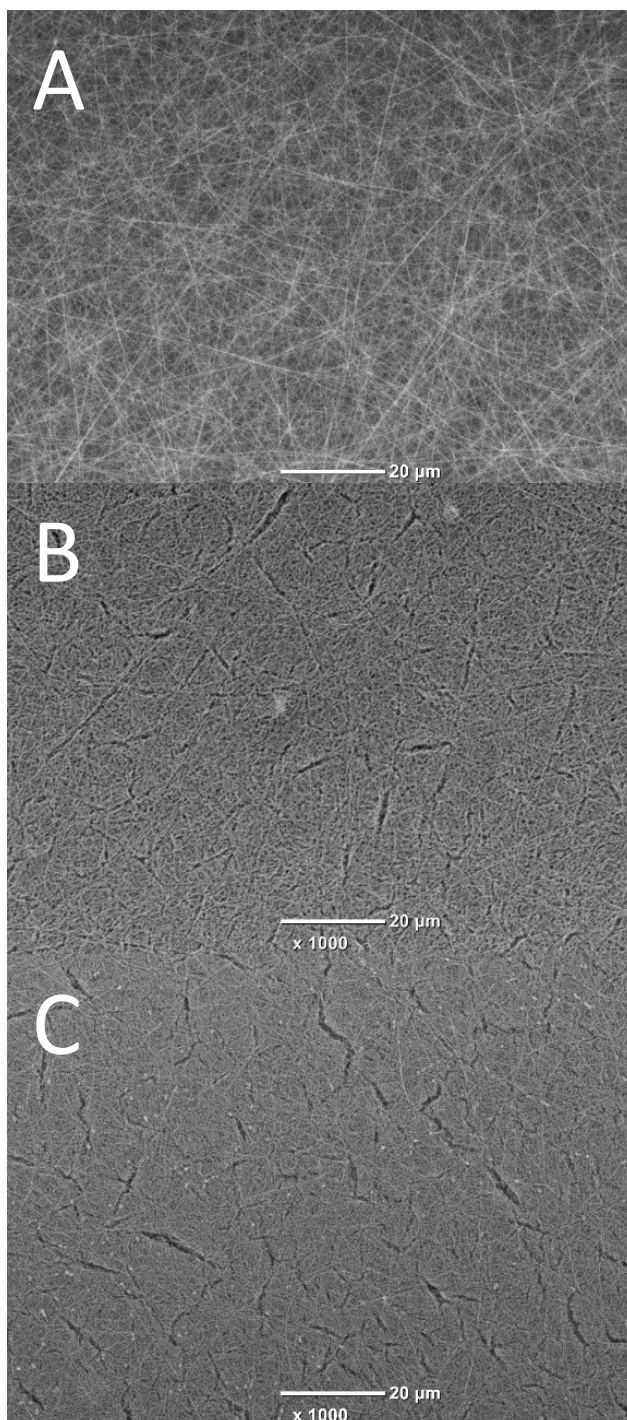
Figure 4.3. - *Scanning electron microscope images with magnification 1k of (A) as-spun nanofibers, and after heat treatment (B) at 500°C in air and (C) at 1000°C under nitrogen flow.*

69
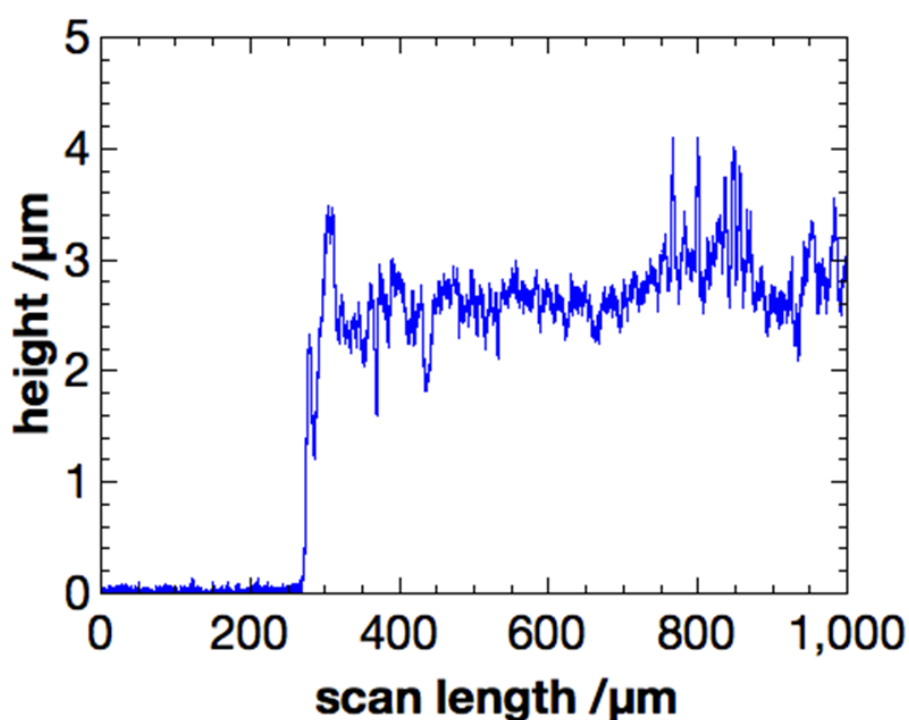
Figure 4.4. *– Profilometry scan of an ITO nanofilament film.*

In order to investigate structure of the deposited films on nanoscale and discuss their morphology in more detail, high resolution SEM images were made. Figures 4.5A&B show the nanofibers before heat treatment. Their surface is smooth and a multilayered structure is observed with limited interconnections between them. Diameters of those nanofibers range between 200 and 300 nm and spaces between them are on the order of few microns. Figures 4.5C&D report the SEM images of the material after treatment at 1000 °C under nitrogen with the same magnifications. As suggested before, the structure of the material has dramatically changed. The original nanofibers have been replaced by shorter nanofilaments 70-170 nm diameter with rough and irregular surfaces. The structure is now more compact, with many interconnections. The spaces between those nanofilaments is ranging from 100 to 500 nm excluding a few bigger cracks of 2 by 1 µm dimensions. Such a structure was not observed before, when the same heat treatment was performed on a free-standing mat characterized in Chapter 2. Here, a slow but not destructive vertical collapse of the nanofibers into a compact, macroporous, 3D structure is observed that must be a result of an interaction with polystyrene during calcination.
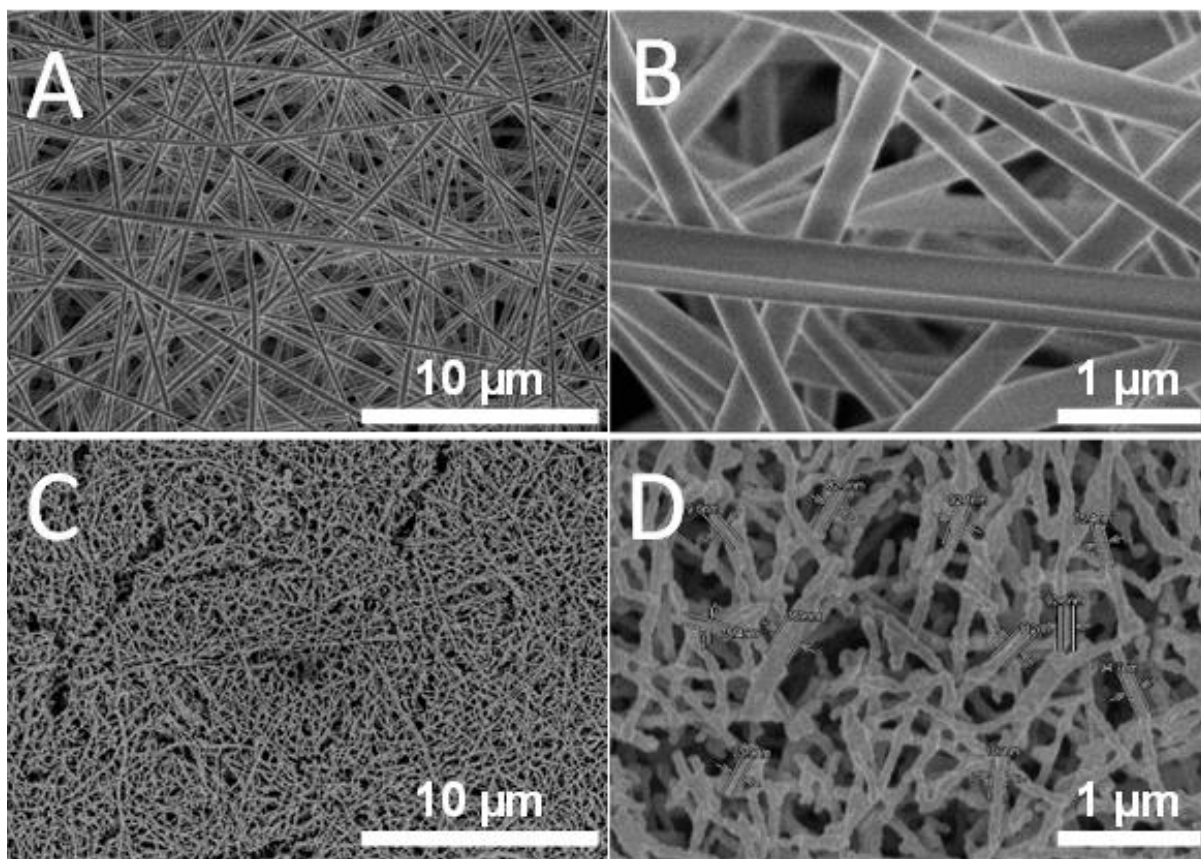
Figure 4.5. High resolution scanning electron microscope images of (A&B) as-spun nanofibers, and (C&D) nanofilaments obtained after additional heat treatment at 1000°C under nitrogen atmosphere.

It is not straightforward to determine what mechanism plays a leading role in this process. It might be that PVP dissolves into PS at high temperature in a pace that allows indium tin oxide domains to slowly reorganize. Another possible explanation might be that the whole electrospun layer is submerged and trapped inside PS coating during calcination, thus changing PVP behavior in regards to the temperature. If oxygen access to the PVP is cut, it could lead to a liquefaction and a layer reshaping instead of a burning out.

XRD analysis was performed at high angle (WAXS) (Figure 4.6) and it shows that all the visible diffraction peaks are attributable to indium tin oxide– JCPDS#01-089-4597, and none to tin oxide SnO_2. Furthermore indexing the observed diffraction peaks gives a cubic lattice parameter a=10.12(3) Å in agreement with the published value of indium tin oxide– JCPDS#01-089-4597 (cubic Ia$\overline{3}$, a=10.1247Å). The good crystallinity of the ITO phase was revealed by the sharpness of the peaks, using Scherrer equation where shape factor (K) = 0.9 gives an average crystallite size of about 38 nm which is a contributing factor in achieving higher conductivity. It is worth noting that the intensity of the observed peaks is similar with

71

those of the JCPDS published values, so the material is free of preferred orientations. The background noise, especially a wide peak between 15° and 30°, is due to the fused silica substrate.
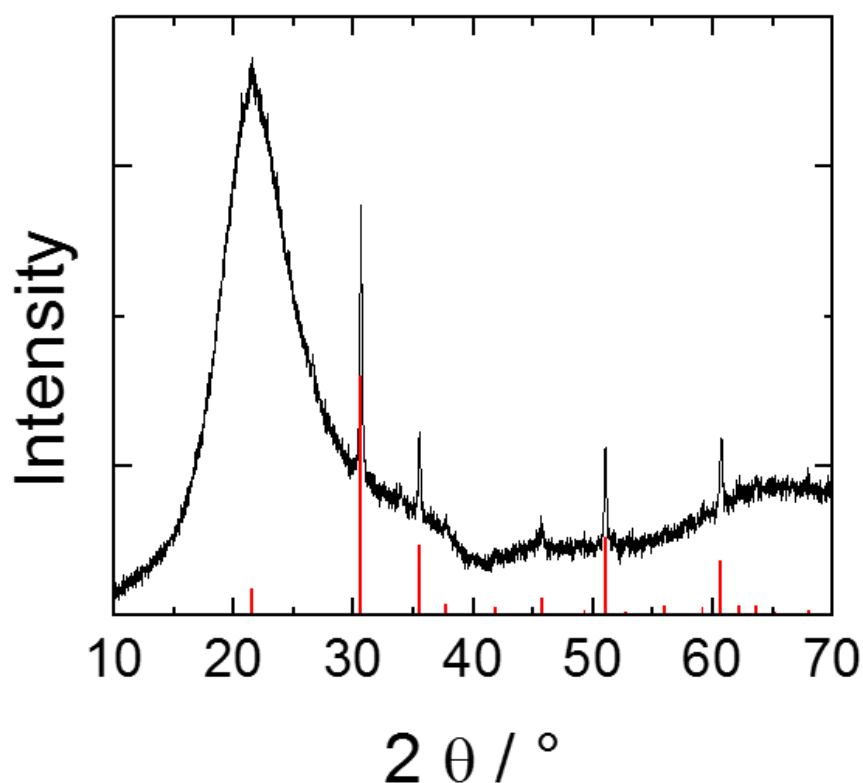
Figure 4.6. *X-ray diffractogram of indium tin oxide nanofilaments obtained after additional heat treatment at 1000°C under nitrogen atmosphere and theoretical diffraction peaks of indium tin oxide (red).*

Finally, the improved mechanical stability of ITO nanofilaments over previously deposited ITO nanofibers (Chapter 3) on the substrate is demonstrated by experiments which simulate the stress that samples would undergo during laboratory procedures (Fig. 4.7). It is clearly visible that the regular ITO nanofibers require extreme care in handling whereas here reported ITO nanofilaments are much easier to use and can clean under direct stream of water or other solvent.
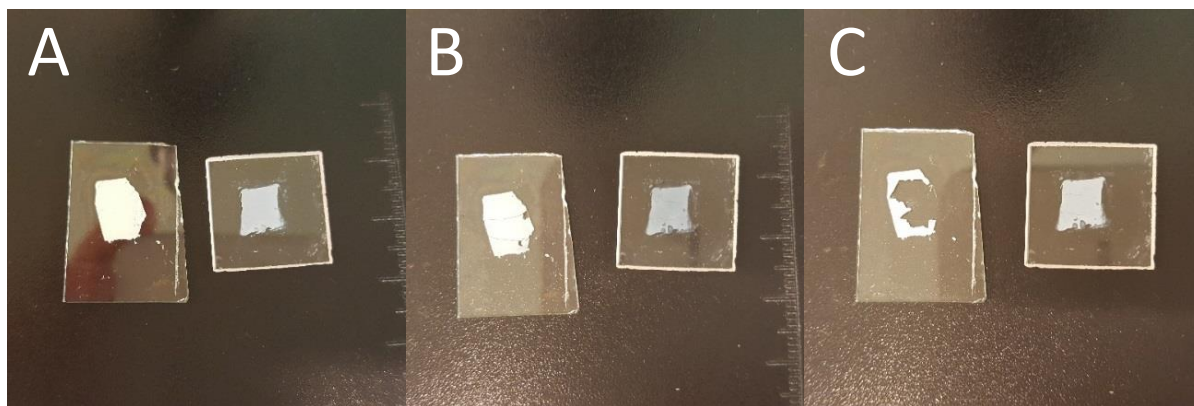
Figure 4.7 – Stability test for ITO nanofiber layers attached to a glass surface with SnCl₄ (left sample on all pictures) and ITO nanofilaments from this work (right sample). (A) Both electrodes in the dry state. (B) Mechanical scratches are made on both samples with a metallic needle. (C) Both electrodes are exposed to a direct stream of water.

4.2.2. Electrochemical properties of ITO nanofilaments

The electrochemical properties of the ITO nanofilaments were evaluated with ferrocenedimethanol (FDM) and ascorbic acid (AA) and compared with the properties of a flat ITO (Figure 4.8). Electrical contact was done as reported in Figure 4.1D and the analyzed surface was chosen in the center of the film, on a homogeneous area. With FDM, the difference between electrodes is small but still noticeable (Figure 4.8A). ITO nanofilaments allows slightly higher currents (28.8 µA vs 24.7 µA for ITO plate) and a lower peak separation (90 mV vs 140 mV for ITO plate). The improvement is more visible with AA that has charge-transfer limited oxidation currents on flat ITO (Figure 4.8B). On the porous electrode, the oxidation current is almost double (45 µA vs 25 µA for flat ITO) and the oxidation potential is shifted towards lower values by about 300 mV. The improvement observed with the porous electrode is attributed to the higher surface area of the ITO nanofilaments available for electron transfer reactions.
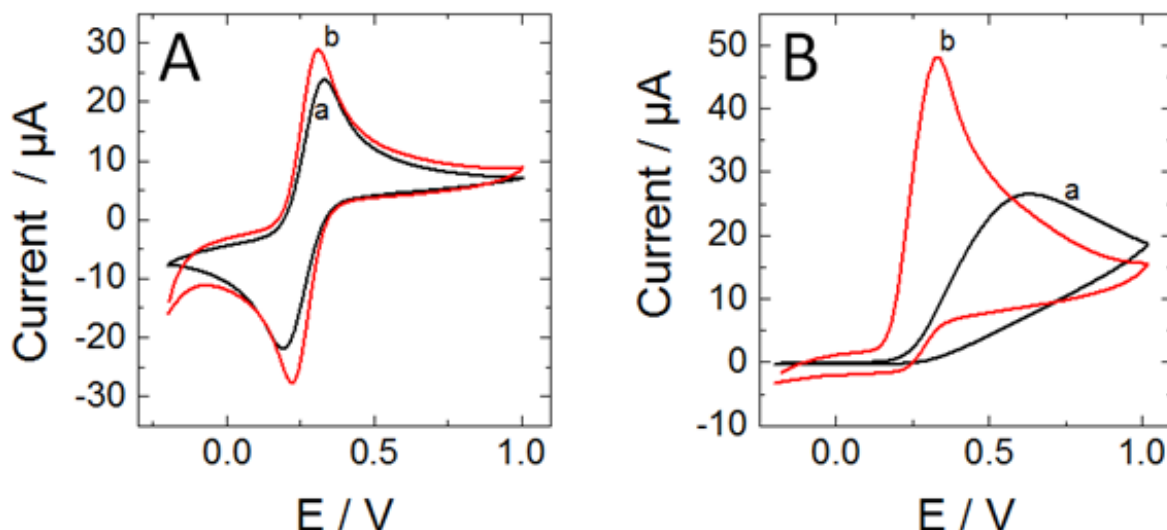
Figure 4.8. *Cyclic voltammograms of (A) 1 mM ferrocenedimethanol and (B) 1 mM ascorbic acid measured with (a) flat commercial ITO plate and (b) ITO nanofilaments. All CVs performed at 50 mV s^{-1} in 0.1M KCl water solution. The geometric surface area was 12.6 mm^2.*

The difference in enhancement of the detection currents observed between the two electrochemical probes is explained by their very different electrochemical properties. The charge transfer reaction involved in the oxidation of ascorbic acid is the limiting step due to low concentration of reactive sites on the ITO electrodes.[163] Increasing the active surface area can increase the amount of reactive sites per given geometric surface area and this in turn enhances redox currents. This is not the case with ferrocenedimethanol which belongs to a group of outer-sphere fast transfer electrochemical probes whose redox currents are diffusionally limited and thus not enhanced at all on thin macroporous electrodes[170] which is the situation we observe with the porous ITO nanofilaments prepared in this work.

4.2.3. Electrochemical deposition of methylated silica

The ITO nanofilaments deposited on fused silica are mechanically stable and provide a good electrode material that can be used for further electrochemical modification and application. This is demonstrated here with the electrodeposition of a methylated silica layer and the application of this functional electrode to spectroelectrochemical detection.

We have followed a protocol previously published describing the electrogeneration of methylated mesostructured silica thin films.[125] In our work, 30 molar % of the silane precursors were methyl-triethoxysilane, in order to introduce sufficient hydrophobicity on the electrode surface for promoting molecule adsorption. The silica films were deposited on the porous ITO electrode by electrolysis of the starting sol at -1.3 V for typically 20 s. XRD measurements collected at low angles (SAXS) show a series of five diffraction peaks characteristic of a lamellar phase (see Figure 4.9 and Table 4.1). The interlayer distance calculated from the position of the (00l) peaks is equal to 4.7 nm within a lamellar structure. This confirms the successful deposition of the mesostructured silica layer. HR-SEM image was also captured (Figure 4.10). The silica film is not so clearly visible, but charging effects that occurred (visible structures brighter and less sharp) during capturing of the image suggested a deposition of non-conductive film that would be consistent with the presence of the film. What is very important is that the access to the porous structure of the ITO nanofilaments is totally kept.
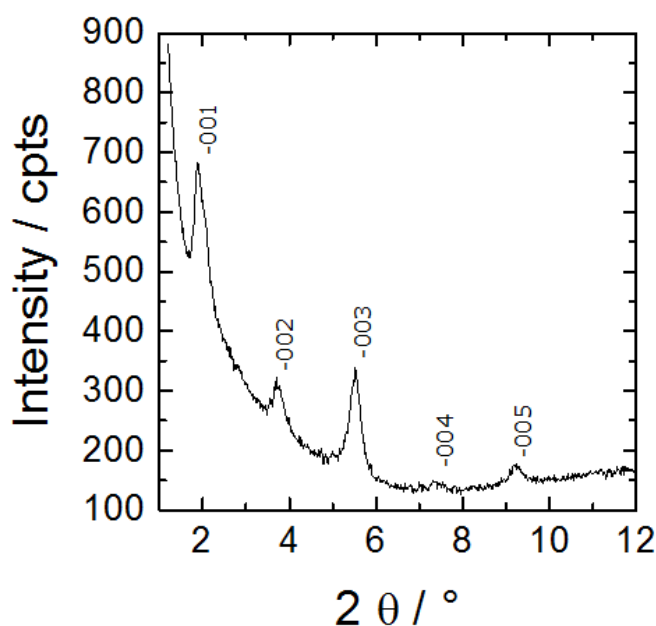
Figure 4.9 - Small-angle X-ray diffractogram of the methylated silica film electrodeposited for 20 s on ITO nanofilaments. The composition of the sol is given in the experimental section of the manuscript.

Table 4.1. – *Small angle X-ray diffractometry results for a mesostructured methylated silica layer electrodeposited on ITO nanofilaments.*

	(001)	(002)	(003)	(004)	(005)
2 theta / °	1.88	3.75	5.51	7.38	9.22
d (nm)	4.67	2.35	1.60	1.20	0.96
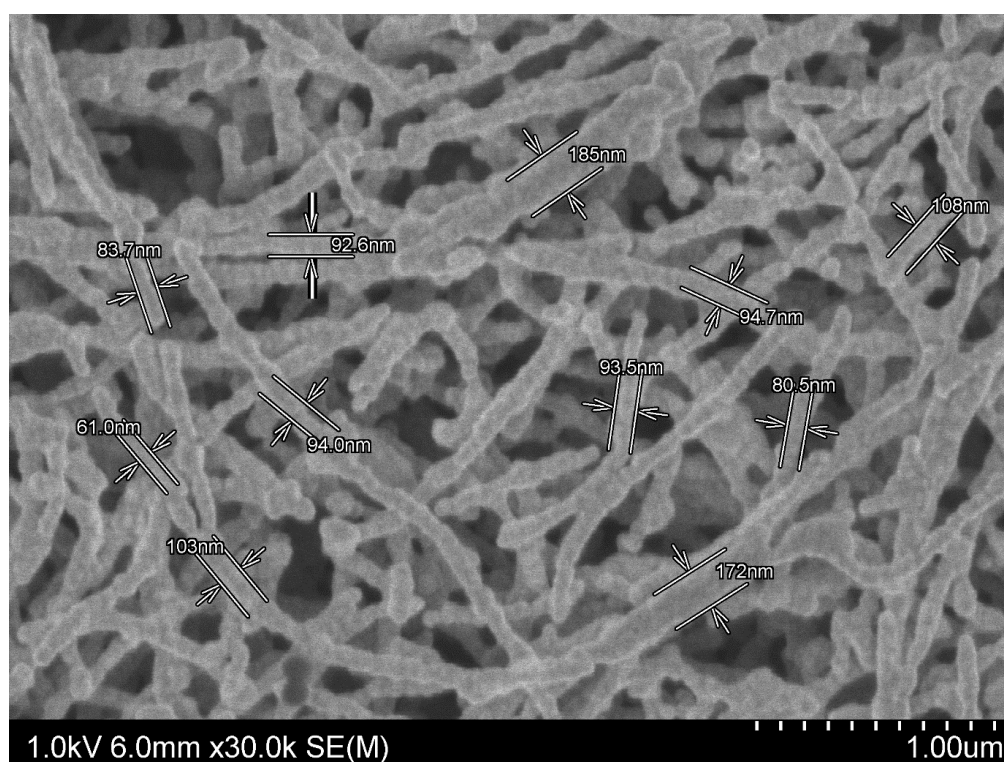
Figure 4.10 - *High resolution scanning electron microscope images of ITO nanofilaments (treated at 1000°C under nitrogen) covered with a methylated silica film electrodeposited for 20 s.*

Finally UV-Vis measurements were performed, the results are shown in Figure 4.11 Transparency was measured in wet state. The reason for that is that the penetration of the porous ITO by water reduces Fresnel reflection and increases transparency. That effect has been already reported in the literature.[164] In these conditions, the porous ITO electrode is transparent in the visible range, up to 70% at 800 nm (see curve a) which is a value over twice higher than ITO nanofibers prepared as free-standing mats from the chapter 3. At smaller

wavelengths, transparency decreases and the cutoff is around 350 nm. The deposition of the methylated silica film for 20 s at -1.3 V lowers the transparency only by a few percent in the whole visible range (see curve b).
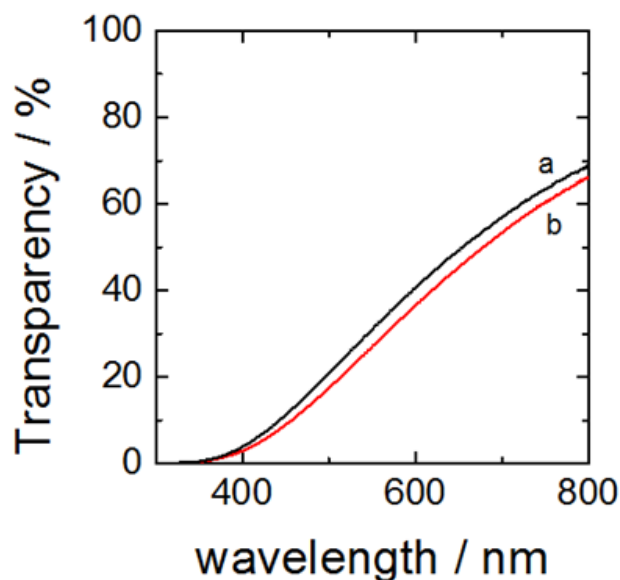
Figure 4.11. *Transparency in visible wavelengths region, black curve (a) – ITO nanofilaments, red curve (b) – ITO nanofilaments modified with a methylated silica film deposited electrochemically for 20 s.*

4.2.4. Electrochemical and spectral detection of industrial dyes

4.2.4.1. Methylene blue adsorption and its detection in high concentrations

One goal of this work is to compare analytical potential of flat ITO and porous ITO nanofilaments, before and after their functionalization with methylated silica both in cyclic voltammetry (Figure 4.12A) and in visible absorption spectroscopy (Figure 4.12B). For this purpose, methylene blue was chosen as analyte. The molecule is an industrial dye and is a common pollutant.[171,172] This dye can irritate the skin or eyes, inhalation can lead to conditions like methemoglobinemia or cyanosis and ingestion can cause varied gastrointestinal issues.[173]

We can first analyze the electrochemical responses observed in a solution containing 100 µM of methylene blue. Electrochemistry on regular ITO plate is very poor with currents below 1 µA (Figure 4.12A, curve a). A significant increase in currents is observed with ITO nanofilaments, reaching up to 5 µA (Figure 4.12A, curve b). In the next step an ITO plate was covered with methylated silica – in that case currents are only slightly bigger than the base

substrate itself, around 3 µA (Figure 4.12A, curve c). Finally methylated silica was deposited on ITO nanofilaments and the improvement of redox capabilities is quite remarkable with reduction current exceeding 30 µA (Figure 4.12A, curve d).

Visible absorption spectra were measured after 60 s adsorption in the same solution with 100 µM methylene blue. A similar progression of the response of the same four samples was observed. Starting with the ITO plate, a noticeable methylene blue spectral signature is observed with smaller peak at 612 nm and the higher peak at 667 nm reaching a value of absorbance A = 0.007 (Figure 4.12B, curve a). ITO nanofilaments allows only a slightly better absorbance A = 0.01 at 667 nm (Figure 4.12B, curve b). A net improvement is visible upon deposition of methylated silica on ITO plate with maximum absorbance at A = 0.027 at 667 nm (Figure 4.12B, curve c) and finally a great enhancement of the signal is obtained by deposition of methylated silica on ITO nanofilaments with A = 0.097 at 667 nm (Figure 4.12B, curve d). Electrochemical experiments with methylene blue as well as the previous ones with ascorbic acid are showing that the porous texture of ITO nanofilaments is useful as
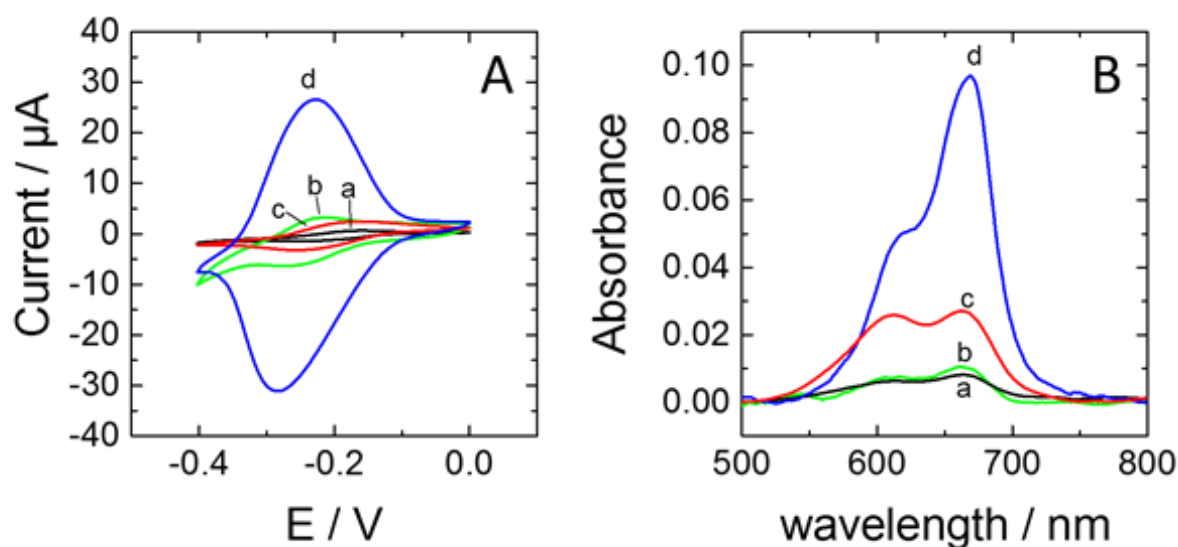
Figure 4.12. (A) Cyclic voltammograms of 100 µM methylene blue at 50 mV s^{-1} in 0.1M KCl. The geometric surface area was 12.6 mm^2. (B) Spectra of methylene blue adsorbed for 60 s from a 100 µM solution. In both cases black curve (a) - flat commercial ITO plate, green curve (b) – ITO nanofilaments, red curve (c) – ITO plate modified with a methylated silica film deposited electrochemically for 20 s, blue curve (d) – ITO nanofilaments modified with a methylated silica film deposited electrochemically for 20 s.

An improvement is visible in the detection of both molecules in comparison with flat ITO. On the opposite, the absorption spectrum measured with ITO nanofilaments is not significantly different from the spectrum recorded on flat ITO. This absorption increased only significantly in the presence of silica. This demonstrates that the methylated silica layer is responsible for the preconcentration of the dye.

The combination of the enhanced electrochemical response allowed by ITO nanofilaments and the preconcentration allowed by methylated silica leads to an increase over 30-fold in redox currents and almost 14-fold in visible absorption by comparison with the response of flat ITO. This demonstrates that functionalized ITO nanofilaments could be of interest for analytical chemistry. The enhanced response after the silica deposition is attributed mostly due to ionic interactions – methylene blue is expected to be a cation in water solutions and silica layers usually have a high density of negatively charged OH^- groups. Small contribution is also expected from methylated part of the silane precursor as it could attract hydrophobic parts of methylene blue.

4.2.4.2. Influence of thickness of silica layers and preconcentration time on methylene blue electrochemistry

Furthermore, it was found out that it is possible to increase the electrochemical signal up to 40 µA and improve the redox potential by depositing the silica layer for 60 s. Figure 4.13A portrays the comparison ITO plate and ITO nanofilaments modified with same silica layer. It was apparent that longer deposition resulted in thicker layers that are capable of stronger preconcentration. Another thing to consider was the time dependency on the signal. On Figure 4.13B there is a comparison with samples that were cycled for 120 times (32 minutes) and the signal had grown up to 120 µA which was a 3-fold increase over 1st scan and same effect was observed on ITO plate and ITO nanofilament layers modified with methylated silica. Unfortunately it happened at a cost of shifting the reduction – oxidation potentials into more negative regions and worsening the peak separation from around 100 to 150 mV. This was a considerable disadvantage for potential analytical application since a clearly defined and stable peak potential is necessary for distinguishing between different species. For that reason in further electrochemical studies only initial scans were used. On Fig. 4.14 there are plotted reduction current values for 1st and 120th cycles for methylated silica layers deposited on ITO nanofilaments for different time periods (20, 60, 120, 180 s). For 20 s deposited samples it is noticeable that increasing the time of preconcentration only slightly increased the peak current (from 32 µA to 38µA) and it could be explained that since that sample was expected

to be very thin the maximum capacity could be reached relatively quickly. Sample deposited for 60s presented a different story where current was massively improved (from 38 μA to 110 μA) as it was expected the structure was probably thicker and surface area was much higher. It is unclear though through what kind of mechanism the redox potentials have been worsened. It might be possible that upon adsorption on the surface methylene blue molecules underwent certain transition or perhaps even polymerization occurred. For even longer times of deposition the initial signal was very poor but it improved with time. This suggested that layer on nanofilaments was so thick that it prevented any redox activity from methylene blue from the bulk solution and the signal started to grow only after diffusion has filled the pores. Final conclusion was that the electrochemical signal was sensitive to the amount of deposited silica but because of problems with signal stability and potential shifting 20s deposition was deemed as the best compromise for the potential application.
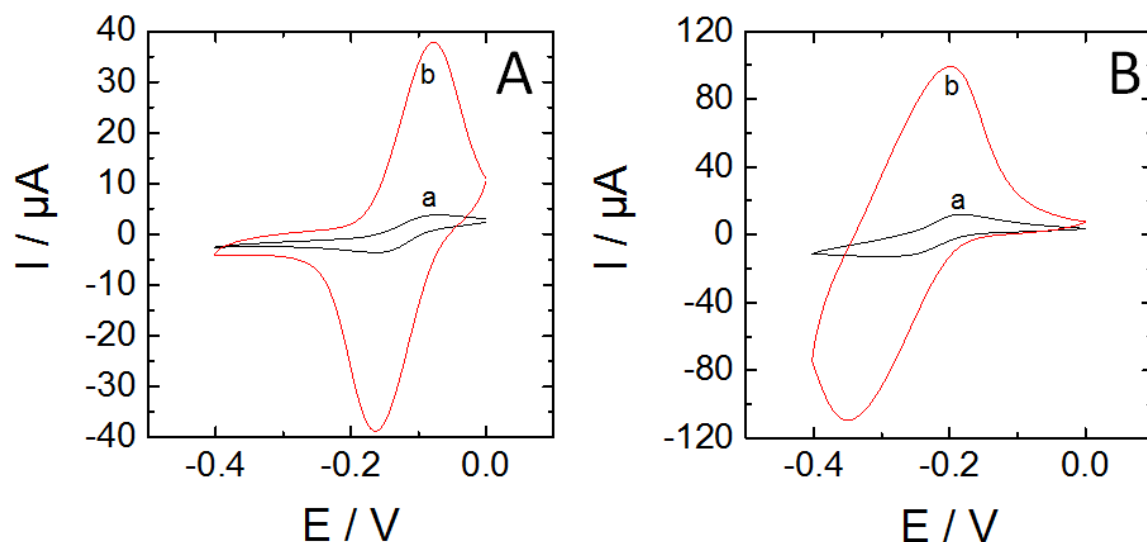
Figure 4.13. - Cyclic voltammograms of 100 μm methylene blue, (A) first cycles, (B) 120th cycle. In both cases black curve (a) – flat commercial ITO plate modified with mesoporous methylated silica for 60s, red curve (b) – ITO nanofilament layer modified with mesoporous methylated silica for 60s. All CVs performed at 50 mV/s in 0,1M KCl water solution.
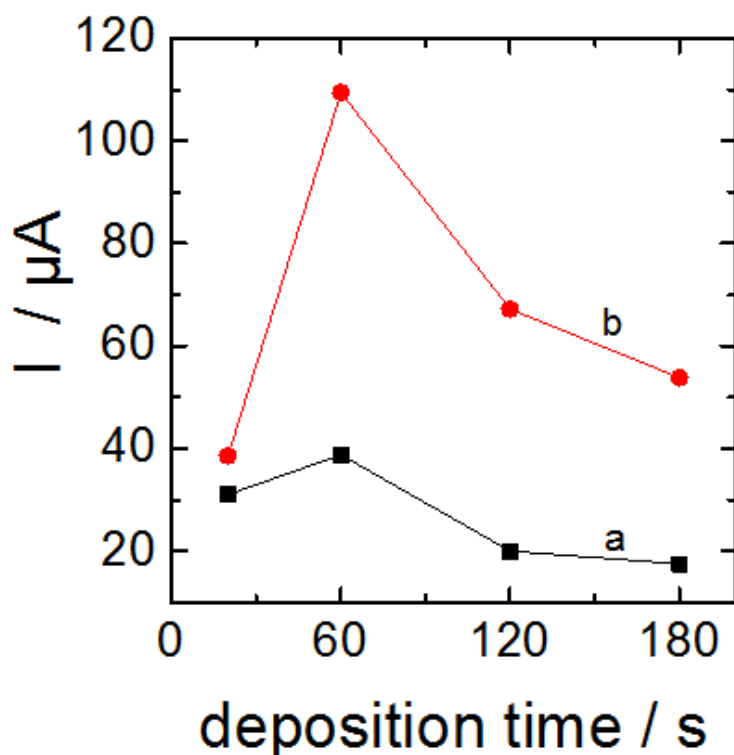
Figure 4.14. - *Dependence between times of deposition of mesoporous methylated silica layer on ITO nanofilaments and reduction current of 100 μm methylene blue, black curve (a) – 1st cycles, red curve (b) – 120th cycles.*

4.2.4.3. Application in combined spectral and electrochemical detection

Figure 4.15A portrays DPV reduction scans of methylene blue from 20 nM to 2 μM concentrations on ITO nanofilaments modified with mesoporous methylated silica deposited for 20 s and it is possible to notice a small shift of potentials with rising concentrations. Figure 4.15B reports similar measurements for flat ITO modified and it is apparent that currents achieved are much lower. The corresponding calibration curves from Figure 4.15C allow to estimate the sensitivity of the two sensors, 0.09 μA μM^{-1} for flat ITO plates (curve a) and ten times higher, 0.87 μA μM^{-1}, for ITO nanofilaments (curve b, note that the same date are presented in Figure 4.16 with logarithmical scales to show the linear response over two orders of magnitude from 20 nM to 2 μM). This linear range of detection from 20 nM to 2 μM is on par with previously reported electrochemical methods for the detection of methylene blue: 10 nM-1μM,[174,175] 1 μM-14 μM,[176] 200 nM-10 μM[177] or 1μM-1 mM.[178] The limit of detection (LOD) obtained from signal-to-noise ratio of 3:1 is 17 nM, close to the lowest

values from the literature,[174,175] much below the reported environmental levels of the dye (120-740 nM)[175] and much more below the level of phytotoxicity (15.6 μM).[179] Therefore, even prior to optimization for sensing applications such layers are already analytically relevant.
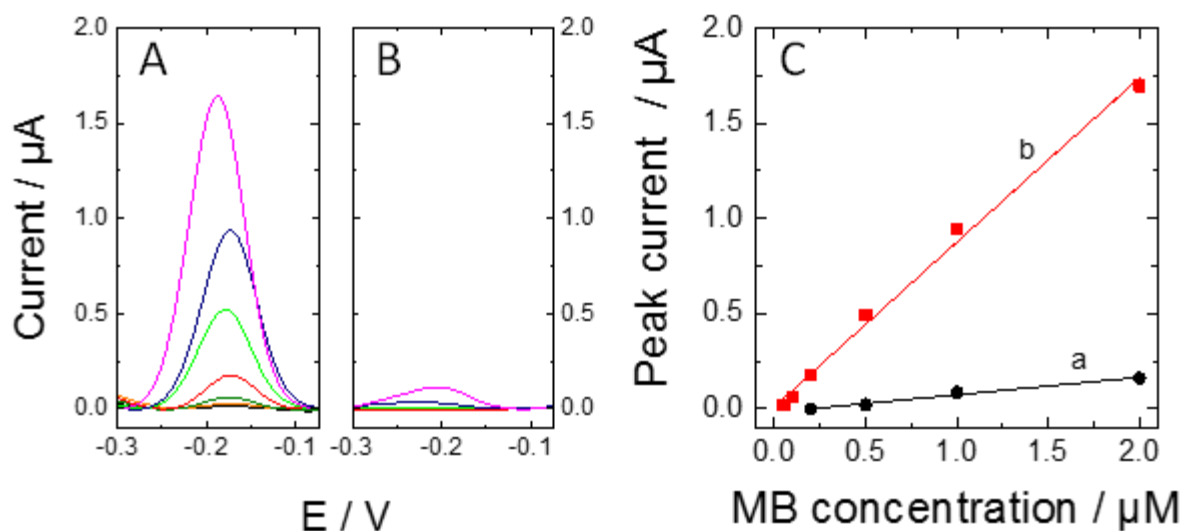
Figure 4.15. *(A) Differential pulse voltammetry – DPV– measurements of methylene blue on ITO nanofilaments modified with mesoporous methylated silica deposited for 20 s from 20 nM to 2 μM concentration and (B) on flat ITO modified in similar way from 200 nM to 2 μM. Measurements were performed in 0.1 M KCl solution with 5 min soaking in respective concentration of methylene blue beforehand. More details on analytical protocol are presented in experimental section. (B) DPV calibration curve of methylene blue detection where black points (a) represent ITO plate modified with a methylated silica film deposited electrochemically for 20 s and red points (b) ITO nanofilaments modified with a methylated silica film deposited electrochemically for 20 s with their respective linear trendlines.*
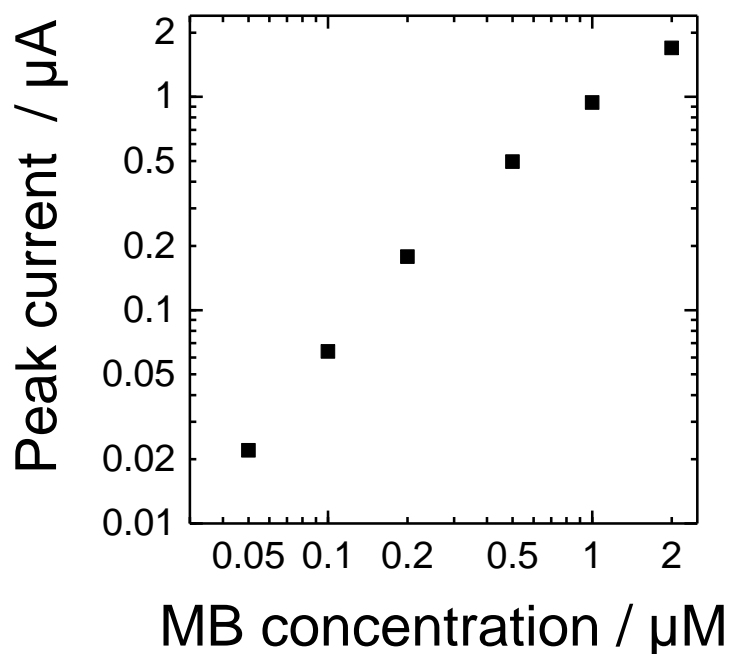
Figure 4.16. - *DPV calibration curve of methylene blue detection on ITO nanofilaments modified with a methylated silica film deposited electrochemically for 20 s in logarithmical scales*

However, one main issue in analytical chemistry is to achieve selectivity. We would like to illustrate this issue in the next section by comparative analysis of methylene blue with two additional dyes, i.e. methylene green, and Meldola's blue, and to draw the potential of spectroelectrochemistry when considering the problem. Figure 4.17A shows the cyclic voltammograms measured with this electrode in the presence of these dyes at 100 μM. Methylene blue response is recalled (curve a). The three molecules show similar signal intensity, but different redox potentials. Methylene green presents two pairs of redox peaks, with reduction reactions occurring at -0.03 V and -0.19 V (curve b) and Meldola's blue also has only one pair of redox peaks with the reduction located at -0.19 V (curve c). Some redox peaks are overlapping and deconvolution of these signals could be difficult in a mixture. Figure 4.17B presents the corresponding visible absorption spectra. Methylene blue (curve a) and methylene green (curve b) possess quite similar spectrum with two peaks at 667 and 612 nm, the only difference being that methylene green has a higher absorption between 400 and 600 nm. Meldola's blue (curve c) has much lower absorption with one absorption peak at 579.

The width of this later signal suggests that it is composed of three or more smaller peaks. Using only one of those two techniques, electrochemistry or spectroscopy, cannot provide conclusive and sufficient data to correctly qualify the molecules and quantify the concentrations in a mixture of these three exemplary components. On the other hand a combination of both techniques, associated with signal deconvolution could be useful for performing analysis in real samples.
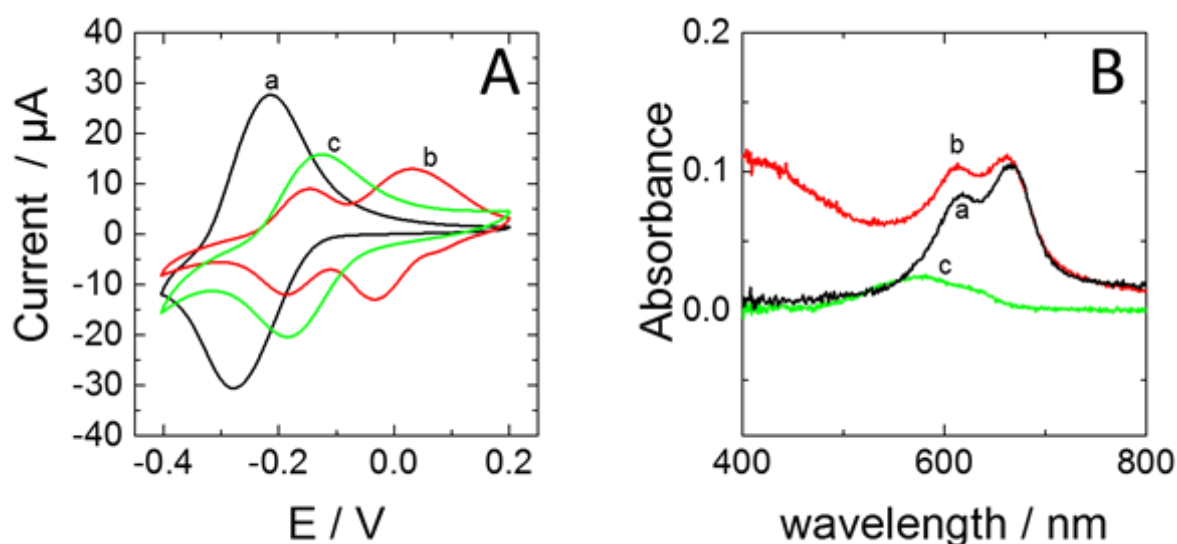
Figure 4.17. (A) Cyclic voltammograms of 100 µM methylene blue (black curve, a), 100 µM methylene green (red curve, b) and 100µm Meldola's blue (green curve, c) performed on ITO nanofilaments functionalized with a methylated silica film deposited electrochemically for 20 s. CVs were done at 50 mV s^{-1} in 0.1M KCl water solution. The geometric surface area was 12.6 mm2. (B) Spectra of methylene blue (black curve, a), methylene green (red curve, b) and Meldola's blue (green curve, c) adsorbed for 60 s from respective 100 µM solutions performed on ITO nanofilaments functionalized with a methylated silica film deposited electrochemically for 20 s.

In the final part, the spectroelectrochemical measurements were performed. First, spectra of the respective dyes before and after application of reducing voltage were measured. On the Figure 4.18 the results are presented and it is noticeable that reduction of the species results in bleaching and lowers the absorption peaks by at least 10 times. Understanding the behavior of the dyes under reducing potential allowed performing a spectroelectrochemical experiment involving two adsorbed dyes (methylene blue and Meldola's blue) at the same time. Considering weaker absorbance of Meldola's blue this dye was used in twice higher

concentration and so the final solution used for 5 min adsorption at silica-modified ITO nanofilaments was 50 µM of methylene blue and 100 µM of Meldola's blue. On such prepared samples cyclic voltammetry was performed and the results are presented on the Figure 4.19. As expected, two pairs of peaks for respective dyes are observed. During the
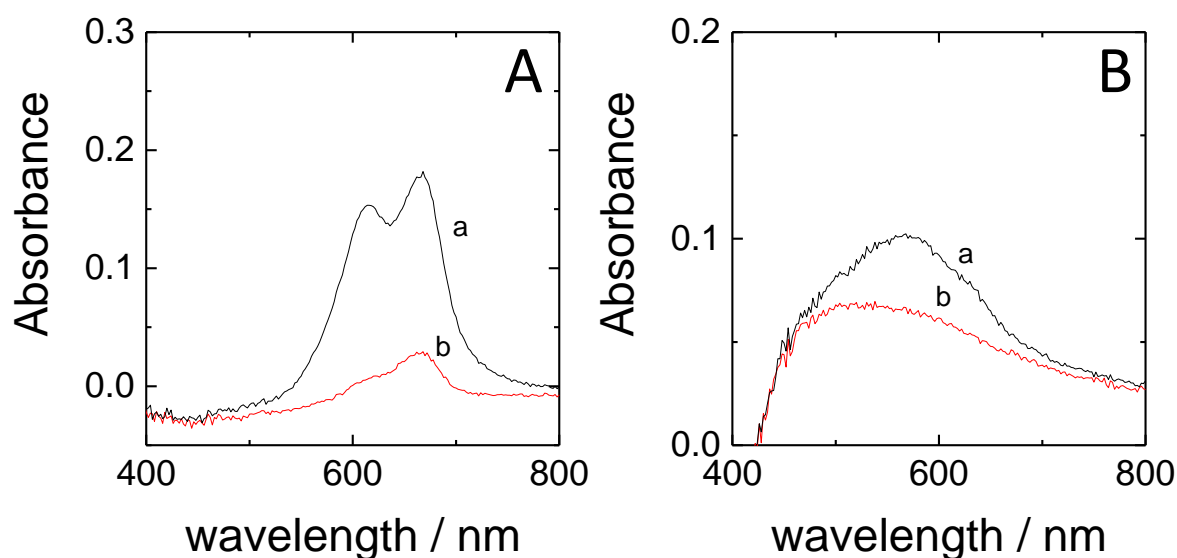
Figure 4.18. – *Absorbance spectra of adsorbed (A) methylene blue and (B) Meldola's blue from 100 µM solutions for 5 minutes on ITO nanofilaments modified with a methylated silica film deposited electrochemically for 20 s where (a – black) is oxidized and (b – red) electrochemically reduced form of the respective dye (-0.4 V for A and -0.3 V for B).*

electrochemical potential sweep the absorbance of the sample was also measured at 600 nm. Obtained electrochemical and spectral data were converted into a derivative voltabsorptogram portrayed on Figure 4.20 (The UV-Vis absorption measurement has been performed by monitoring the changes at 600 nm, with 10 points being measured over 1 second. Smoothing of the curve was performed in Origin software using Savitzky-Golay method over 100 points of window with no boundary conditions and polynomial order of 2.). Here, one can follow the changes of absorption with respect to the applied potential in a classic spectroelectrochemical measurement. It is apparent that the changes of absorption are following the electrochemical redox process to a high degree. Again, two pairs of peaks are visible, the smaller ones around -0.19 V belonging to Meldola's blue and bigger ones at -0.38 V belonging to methylene blue. With this final experiment the capability of performing a spectroelectrochemical measurement is proven. It shows the potential of functionalized ITO nanofilaments in

spectroelectrochemical sensing in more complex mixtures of compounds that have a spectrum in the visible light range.
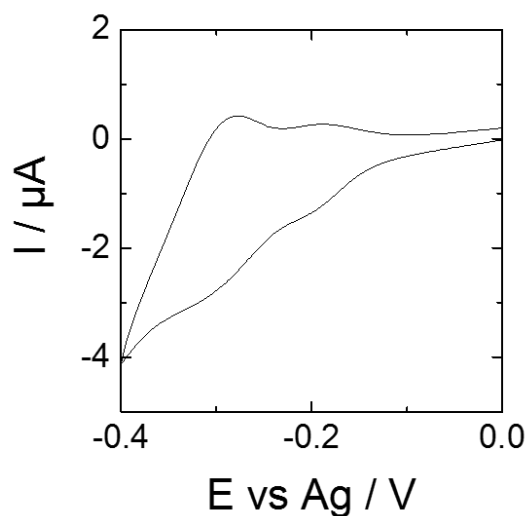
Figure 4.19. – A) Cyclic voltammogram of 50 µM methylene blue and 100 µM Meldola's blue adsorbed for 5 min performed on ITO nanofilaments functionalized with a methylated silica film deposited electrochemically for 20 s. CV was done at 10 mV s^{-1} in 0.1 M KCl water solution. The geometric surface area was ~8 mm^2.
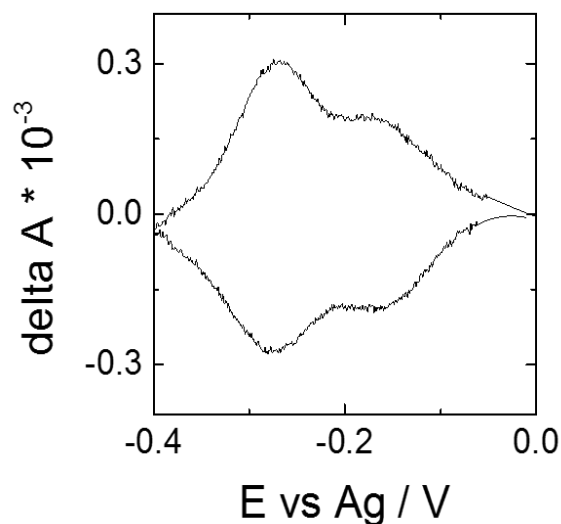
Figure 4.20. Derivative voltabsorptogram of 50 µM methylene blue and 100 µM Meldola's blue adsorbed for 5 min performed on ITO nanofilaments functionalized with a methylated silica film deposited electrochemically for 20 s. CV was done at 10 mV s^{-1} in 0.1 M KCl water solution.

4.3. Conclusions

Highly interconnected indium tin oxide nanofilaments have been obtained by electrospinning a precursor solution on a fused silica substrate and calcination. We were able to prevent the breaking of the nanofibers caused by the shrinkage of the material observed during calcination by using a simple polystyrene layer drop-coated on the substrate. A dramatic change was observed in the structure of the porous electrodes because of the interaction of the nanofibers with the polystyrene at high temperature. ITO nanofilaments possess greatly enhanced electrochemical properties compared to flat ITO and have transparency in the visible light region up to 70 % at 800 nm. The ITO nanofilaments deposited on fused silica are mechanically stable and provide a good electrode material that can be used for further electrochemical modifications and applications. This is demonstrated here with the electrodeposition of a mesostructured methylated silica layer and the application of this functional electrode to spectroelectrochemical detection of industrial dyes with linear range of detection for methylene blue between 20 nM and 2 μM with limit of detection at 16.9 nM. In the future, we want to evaluate the analysis of more complex mixtures with combined spectroscopic and electrochemical detections. One direction that is considered for improving the accuracy of the sensor is the electrodeposition of molecularly imprinted films, mesostructured or not, on ITO nanofilaments. This would allow to introduce an additional selectivity, during the adsorptive preconcentration step used before detection with electrochemistry and spectroscopy. Another direction is the use of the functionalized ITO nanofilaments for surface enhanced Raman spectroscopy (SERS), in combination with electrochemical detection. We think that other applications could also be considered for this material, e.g. solar cells.

Chapter 5. Application of indium tin oxide nanofilaments in electrochemiluminescence generation

5.1. Introduction

Elecrochemiluminescence (ECL) is a process in which the emission of photons is triggered by an electrochemical oxidation or reduction of the species on the electrode. The reaction can occur in several different ways, the most popular being the coreactant pathway.[180] ECL process has become an important component of many sensing devices, also commercial ones, due to high sensitivity of light sensors developed in recent years. It allows for quantification of a very small amount of photons which translates to low detection limits for many compounds like hemagglutinin of influenza virus, protein cancer biomarkers or antibodies.[12] It is also useful because of the possibility of controlling the reaction in required manner to e.g. confine the light emission to where the detector is located thus increasing the signal-to-noise ratio.[181] Because of such popularity there is an interest to improve the ECL-based detection methods even more, for example by using electrodes with porous surface. It is possible to enhance the ECL signal by two orders of magnitude at low reactant concentrations using silica mesochannels compared to bare ITO electrode.[182] Similar enhancement was achieved using electrospun PAN-co-PAA nanofibers.[183] One order of magnitude of improvement was achieved by covering the electrode with nanoporous TiO_2.[184] In another report, porous graphene enhanced ECL generation by two times over flat glassy carbone electrode.[185] Because of those developments there is an interest to use porous electrodes that are also transparent to improve the ECL generation even more as the transparency could allow the photons from deep-lying layers to reach the detector. As mentioned in the literature survey part, mesoporous ATO electrode was already used to improve the ECL generation by 132 times compared to flat electrode.[61] Following that idea, in this chapter we are using the porous and transparent ITO nanofilament electrode (see Chapter 4) to explore the possibilities of enhancing the ECL response of a common system of $Ru(bpy)_3^{2+}$ as luminophore and tripropylamine (TPrA) as coreactant dissolved in water. In this system both molecules are oxidized electrochemically for the light emission to occur. Detailed proposed mechanisms for the reaction were found in a work by Miao[181] and are presented on the Scheme 5.1. Furthermore, we study how surface modification with silica layers influences the process, first by adsorbtion of the $Ru(bpy)_3^{2+}$ on surface of methylated silica and finally with immobilized

Ru complex on silica through click-chemistry. This inquiry could perhaps give an idea about best ways to design ECL systems on porous and transparent substratessubstrates.
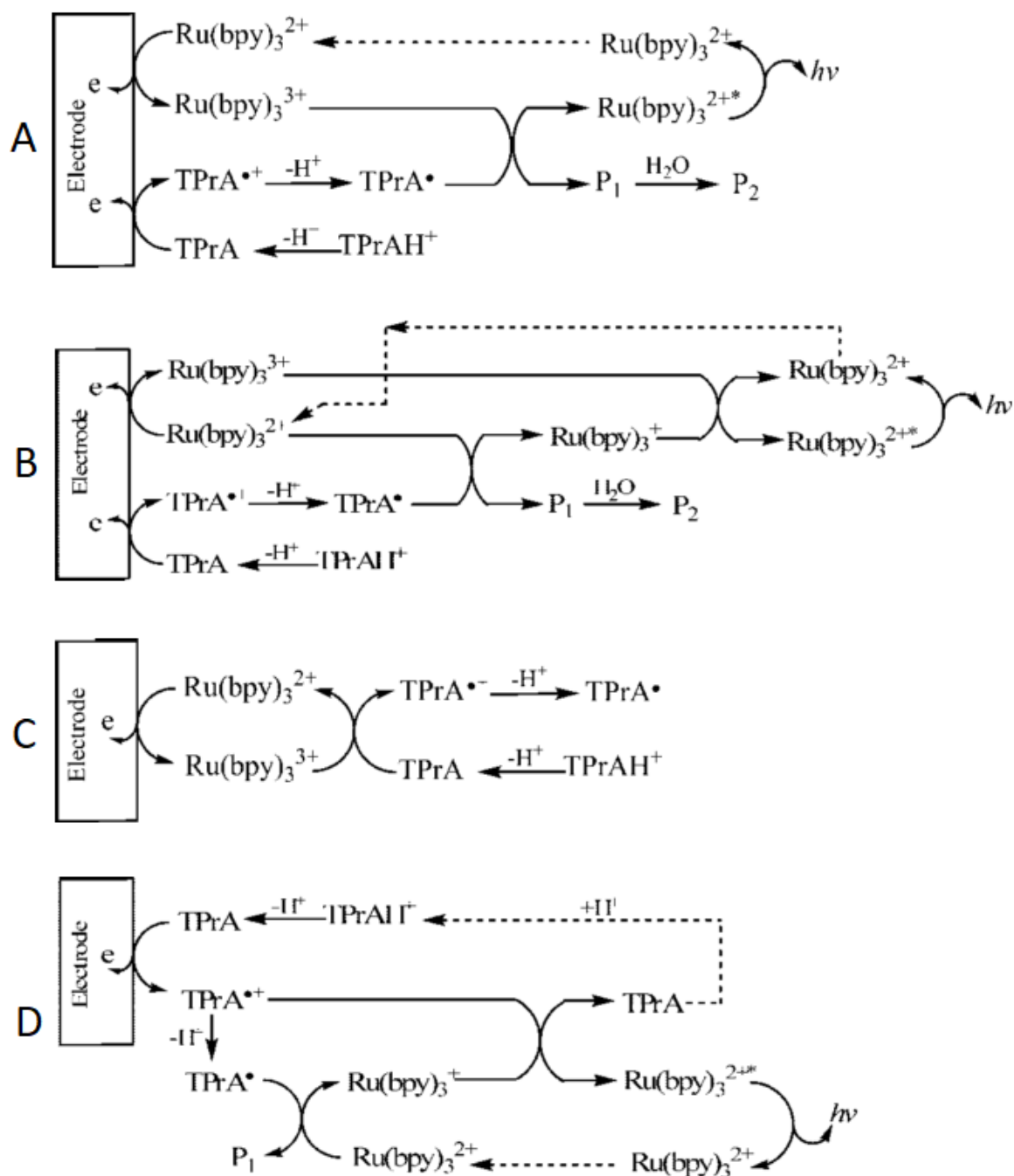
Scheme 5.1. ECL generation mechanisms in Ru(bpy)$_3$$^{2+}$ - TPrA system.[181]

5.2. Results and discussion

5.2.1. Electrochemiluminescence of dissolved $Ru(bpy)_3^{2+}$

In this section we use a widely-used Ruthenium luminescent complex, $Ru(bpy)_3^{2+}$ dissolved in the solution together with coreactant that was tripropylamine (TPrA). This system, when oxidized, produces electrochemiluminescence that can be measured. We would like to study how a porous structure of ITO nanofilaments would influence the electrochemical response and the intensity of generated ECL. The Figure 5.1 presents electrochemical response of Ru (II) complex in solution in concentration of 100 µM on both flat ITO and ITO nanofilaments without the addition of mediator. Visibly higher capacitance currents are present on porous ITO but the measured redox currents are only 40 % higher compared to flat electrodes (6.03 µA peak current vs 4.25 µA) which is slightly higher than expected for diffusionally limited redox process on macroporous ITO nanofilaments like in the case of ferrocenedimethanol oxidation-reduction (see Chapter 4 and Figure 4.8 A). In the Figure 5.2 is presented electrochemistry of electrochemiluminescent system ($Ru(bpy)_3^{2+}$ 100 µM+ TPrA 10 mM) on both flat ITO and ITO nanofilaments. Due to TPrA being in a 100 times higher concentration, its oxidation current dominates over the possible response from Ru (II) oxidation. And so, one can see that the oxidation currents are around 20 % higher for porous

Figure 5.1. Cyclic voltammograms performed in solution of 100 µM $Ru(bpy)_3^{2+}$ on (A) ITO plate and (B) ITO nanofilaments. CVs were done at 50 mV s^{-1} in 0.1M KCl water solution. The geometric surface area was 38.5 mm^2.

Figure 5.2. *Cyclic voltammograms performed in solution of 100 µM Ru(bpy)$_3^{2+}$ and 10 mM tripropylamine on (A) ITO plate and (B) ITO nanofilaments. CVs were done at 50 mV s^{-1} in 0.1M KCl water solution. The geometric surface area was 38.5 mm^2.*

ITO which is consistent with earlier findings for diffusionally limited probes. The oxidation potential is also shifted from 1.14 V for flat ITO to 1.04 V for ITO nanofilaments which is a 100 mV shift.

The Figure 5.3 presents the ECL response to those electrochemical experiments. The initial ECL intensity in the first cycle for ITO plate is 2.93*10^6 counts per second (cps) while for porous ITO it is 19.8*10^6 cps which is a 6.8 time increase. In both cases the luminescence signal decreases together with following electrochemical oxidation cycles as the concentration of TPrA is decreased near the electrode. In the last cycle the increase over flat electrode is slightly higher, at 7.7, so the ECL decay is slightly lower for porous electrode. Finally, it is possible to notice that the ECL has a second smaller peak during the back scan in both cases of flat and porous ITO. To study this in more detail a graph correlating voltage and ECL generation was prepared from available data and the results are presented on the the Figure 5.4. It is visible that the ECL generation is only starting after reaching the oxdiation potential of ruthenium around 1.0 V and peaks at 1.15 V. At the same time the ECL is diminished at too high potentials but it recovers in the backscan after coming close to tripropylamine oxidation potential. The drop of the ECL generation at higher potentials could come from the water oxidation leading to decrease in pH and to subsequent protonation of TPrA. In this form the coreactant does not form the radical necessary for ECL to occur. On the backscan,

potential is lowered and pH is equalized with the solution to neutral value but it is still high enough to oxidize TPrA, explaining the brief reappearance of ECL in form of a smaller peak and small hysteresis.

Figure 5.3. ECL response during cyclic voltammetry (from Figure 5.2) of 100 μM Ru(bpy)$_3^{2+}$ and 10 mM tripropylamine on (a) ITO plate and (b) ITO nanofilaments. The geometric surface area was 38.5 mm^2.

Figure 5.4. (a) Cyclic voltammogram of Ru(bpy)$_3^{2+}$ performed in solution of 100 μM Ru(bpy)$^{2+}$ and 10 mM tripropylamine on ITO nanofilaments and (b) corresponding ECL generation

5.2.2. Electrochemiluminescence of adsorbed Ru(bpy)$_3^{2+}$

In the next part we have studied if the immobilization via adsorption of the luminescent complex could be a viable method for achieving a stable ECL generation over several cycles. Here, flat ITO and ITO nanofilaments functionalized with methylated silica have been used for ECL generation. Ru (II) complex was adsorbed for 15 min in each case in appropriate concentration and then tested in a different coreactant (TPrA) concentration to study the potential improvement. Firstly, cyclic voltammetry experiments with adsorbed complex from 10 µM solution were performed in KCl 0.1 M (Figure 5.5). Much higher oxidation currents were observed for ITO nanofilaments (10.5 µA) than for ITO plate (5.8 µA). This suggests that more compound was adsorbed thanks to the higher surface area. Afterwards the cyclic voltammetry was performed in the presence of 10 mM TPrA. In the Figure 5.6 cyclic voltammograms for such measurements on flat and porous ITO are presented. Contrary to bare electrodes, here we see that oxidation of TPrA results in over twice bigger peak currents than on the flat electrode (325 vs 135 µA) and the oxidation potential is shifted on the porous electrode towards more positive values (1.1 V here for a complex adsorbed on silica vs 1.04 V for the bare) and remains similar on the flat one (1.1 V in both cases). On Figure 5.7 the corresponding ECL measurement is portrayed. In the first scan the ECL intensity for ITO nanofilaments was $21.1*10^6$ cps compared to $2.91*10^6$ cps on the flat electrode which is a 7.25 time increase. In the last cycle the increase was lower at 6.19.

Figure 5.5. *Cyclic voltammograms of Ru(bpy)$_3^{2+}$ adsorbed on methylated silica for 15 min from 10 µM in KCL 0.1 mM on (A) ITO plate and (B) ITO nanofilaments. CVs were done at 50 mV s^{-1} in 0.1M KCl water solution. The geometric surface area was 38.5 mm^2.*
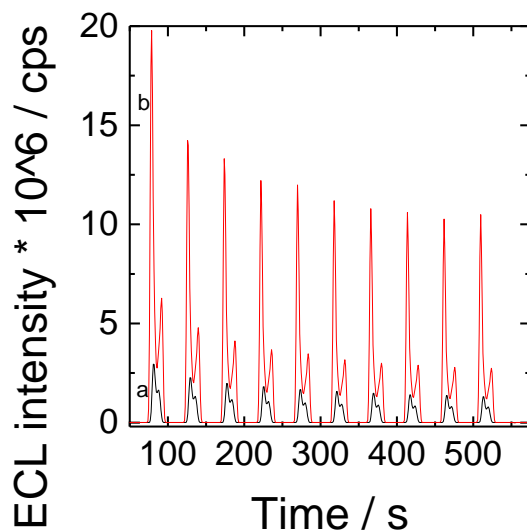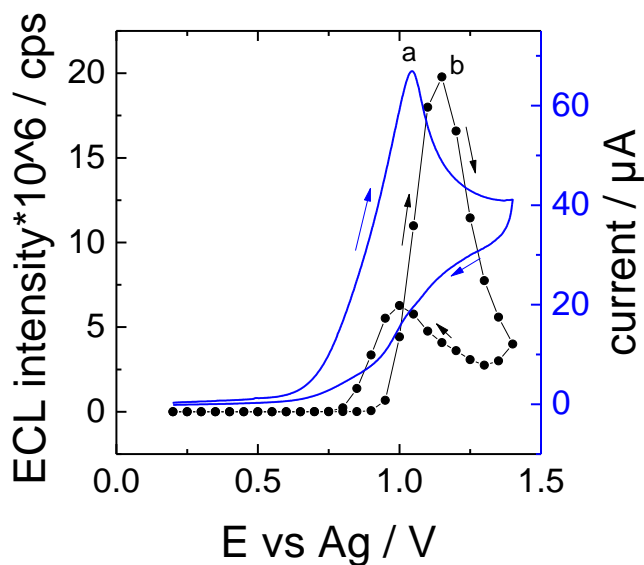
Figure 5.6. *Cyclic voltammograms of Ru(bpy)$_3^{2+}$ adsorbed on methylated silica for 15 min from 10 µM in solution of 10 mM TPrA on (A) ITO plate and (B) ITO nanofilaments. CVs were done at 50 mV s^{-1} in 0.1M KCl water solution. The geometric surface area was 38.5 mm^2.*

Figure 5.7. *ECL response during cyclic voltammetry (from Figure 5.4) of Ru(bpy)$_3^{2+}$ adsorbed on methylated silica for 15 min from 10 µM in solution of 10 mM TPrA on (a) ITO plate and (b) ITO nanofilaments. The geometric surface area was 38.5 mm^2.*

Similarly to previous case of all reactants dissolved and ECL measured on bare electrodes the increase of luminescence is higher than it would be expected from electrochemistry, although here it is noticeable that the addition of mesoporous methylated silica layer used for Ru complex adsorption impedes the TPrA oxidation. It is also possible to notice that the decay of the ECL over 10 continuous cycles is faster than with Ru complex dissolved in the solution, despite the same TPrA concentration of 10 mM. This suggests that there occurs a loss of the luminophore over time of the experiment. On Figure 5.8 is portrayed an electrochemical experiment as before but this time the concentration of Ru (II) complex preconcentration solution was 1 μM (that is 10 x lower). The increase in oxidation is slightly less than two times (209 vs 123 μA) with again, oxidation potential shifted on the flat electrode so much that there is no peak present while it remains similar on the porous one at 1.04 V.

Figure 5.8. *Cyclic voltammograms of Ru(bpy)$_3^{2+}$ adsorbed on methylated silica for 15 min from 1 μM in solution of 10 mM TPrA on (A) ITO plate and (B) ITO nanofilaments. CVs were done at 50 mV s^{-1} in 0.1M KCl water solution. The geometric surface area was 38.5 mm^2.*

Corresponding ECL generation cycles are presented on Figure 5.9. Starting ECL intensity on the porous electrode was $0.16*10^6$ cps and $0.05*10^6$ cps which is only slightly more than 3 time increase. In the last cycle the difference grows to 7.1 times. Some irregularities appear here. Firstly, the oxidation currents are clearly lower than in previous case despite TPrA concentration unchanged. According to Scheme 5.1 in this reaction the Ru (II) complex recycling occurs in certain conditions and this might have been a significant contributor increasing the currents. Here, the ECL intensity is two orders of magnitude lower, rather than expected one which is also surprising on its own and suggests that the amount of adsorbed

Ru (II) complex is lower and thus also does not contribute to oxidation currents in the same way.

Figure 5.9. ECL response during cyclic voltammetry (from Figure 5.6) of Ru(bpy)$_3$$^{2+}$ adsorbed on methylated silica for 15 min from 1 µM in solution of 10 mM TPrA on (a) ITO plate and (b) ITO nanofilaments. The geometric surface area was 38.5 mm^2.

Finally, the experiments with lower concentration of TPrA (1 mM) with Ru (II) adsorbed from 10 µM solution have been conducted. On Figure 5.10 there are presented the cyclic voltammograms. The oxidation currents are twice higher on porous electrodes (150 vs 75 µA) and again the shift of the peak is clearly visible (1.32 V for the flat electrode and 1.08 V for the porous). The ECL intensity portrayed on Figure 5.11 for the first cycle for porous ITO is $20.8*10^6$ cps and for flat $4.43*10^6$ cps which gives 4.7 times increase. In the 10th cycle this increase grows slightly to 5.23. The behavior of the system is consistent with previous measurements with the exception of initial ECL signal on porous electrode being very similar to the one when higher concentration of TPrA (10 mM) was used. Nevertheless across all the samples there is a 5-7 time increase in the ECL generation and the rate of decay over 10 cycles is comparable for both flat and porous electrodes when the concentration of Ru (II) complex during adsorption was 10 µM (75 % for 10 mM of TPrA and 83 % for 1 mM of TPrA). In case of adsorption of Ru(bpy)$_3$$^{2+}$ from 1 µM there is a large difference between porous electrode (50 % decay) and flat one (90 %).

Figure 5.10. *Cyclic voltammograms of Ru(bpy)$_3$$^{2+}$ adsorbed on methylated silica for 15 min from 10 µM in solution of 1 mM TPrA on (A) ITO plate and (B) ITO nanofilaments. CVs were done at 50 mV s^{-1} in 0.1M KCl water solution. The geometric surface area was 38.5 mm^2.*
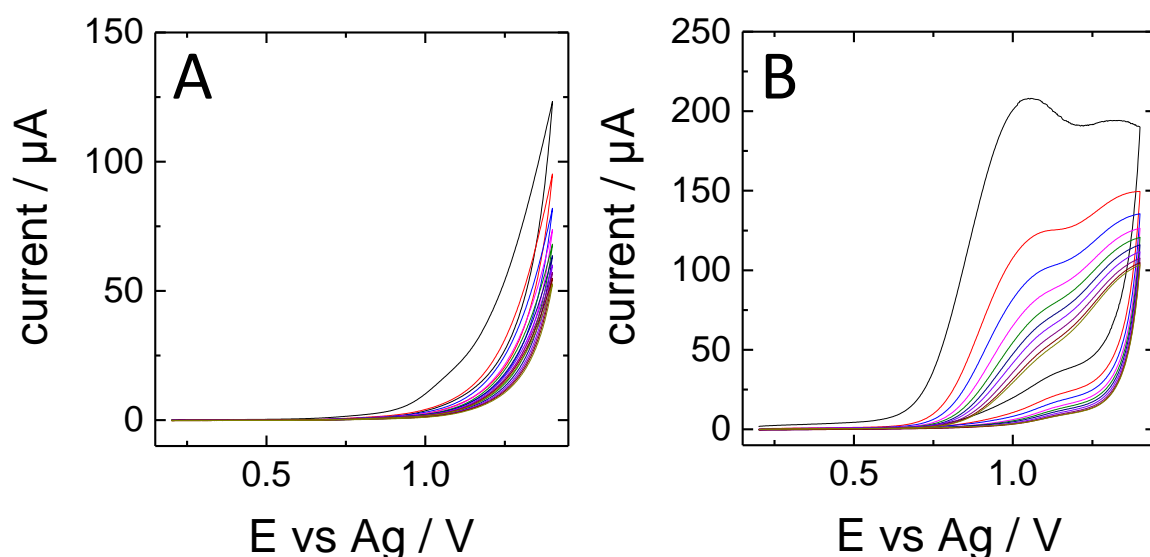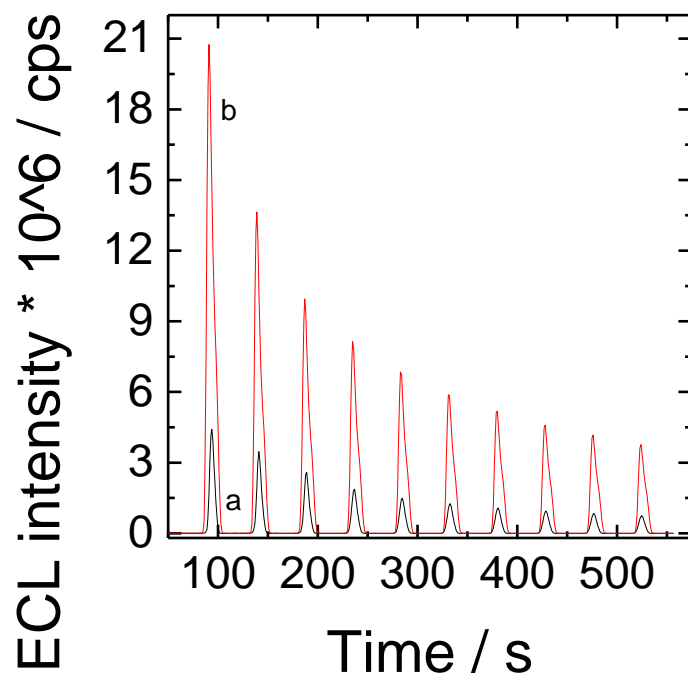

Figure 5.11. *ECL response during cyclic voltammetry (from Figure 5.8) of Ru(bpy)$_3$$^{2+}$ adsorbed on methylated silica for 15 min from 10 µM in solution of 1 mM TPrA on (a) ITO plate and (b) ITO nanofilaments. The geometric surface area was 38.5 mm^2.*

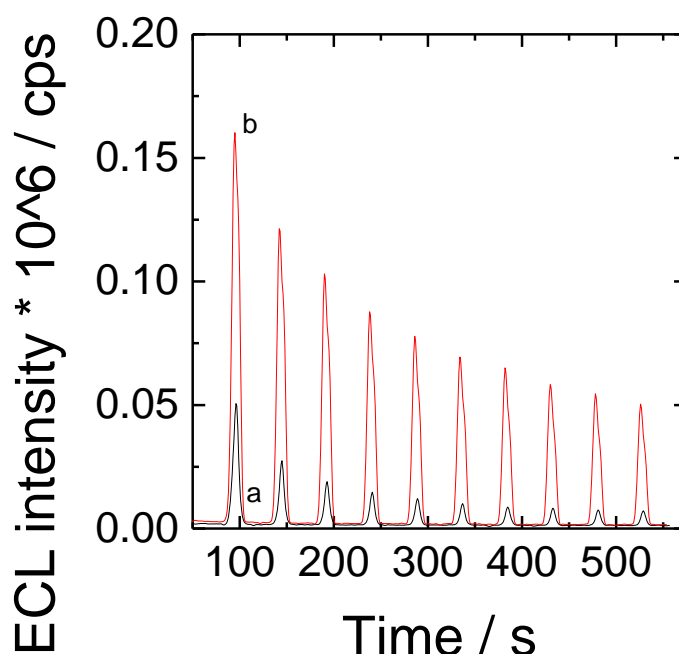Finally, as previously for flat ITO the graph of voltage vs ECL intensity was prepared and is presented on Figure 5.12. One can see that ECL starts from potential of 1.2 V, which is delayed compared to the peak oxidation potential of ruthenium, but rises continuously until 1.3 V of the backscan and only then starts to decrease. There is a small peak visible on the backscan at around 1V like in the case of unmodified nanofilament electrode but its size suggests that the water oxidation and pH drop is not as high as on bare ITO nanofilament electrode. It suggests that the presence of methylated silica layer is the cause which might be an unplanned benefit of such layer. A quite substantial hysteresis is also present which suggests that once the Ru (II) complex is oxidized it is not instantly used up but instead circulates several times participating in several acts of luminescence generation until the potential applied is too low for TPrA oxidation.

Figure 5.12. *(a) Cyclic voltammogram of Ru(bpy)$_3^{2+}$ adsorbed for 15 min from 10 μM solution performed in solution 10 mM tripropylamine on ITO nanofilaments and (b) corresponding ECL generation.*

To summarize, while it was proven that adsorption of Ru(bpy)$_3^{2+}$ on mesoporous methylated silica is possible and generates ECL, the rate of decay over 10 cycles suggests that the method is unreliable for long-time operations. Another way of immobilization is necessary to ensure the stable signal over longer time period.

5.2.3. Electrochemiluminescence of click-immobilized Ru(bpy)$_3^{2+}$

In the final part of ECL experiments we investigate the possibility of covalently binding the luminophore to the electrode surface to achieve the highest stability. For this reason a silica layer modified with an azide functional group was prepared both on flat and porous ITO. This part of work has been conducted in collaboration with Cheryl Karman. Such azide group allows to perform a functionalization with prepared derivative of Ru complex ([Ru(bpy)$_2$(bpy')](PF$_6$)$_2$ where bpy' stands for 4-[2-propyn-1-yloxy)methyl]-4'-methyl-2,2'-bipyridine by click Huisgen reaction. Thanks to such preparation method, electrochemiluminescent complex is covalently immobilized on the surface. On Figure 5.13 there is presented the electrochemical response of such films. One can see on flat ITO redox currents of around 2 µA whereas on porous ITO they reach up to 10 µA. This clearly shows that the amount of immobilized complex on porous electrode is at least 5 times higher than on

Figure 5.13. *Cyclic voltammograms of click-immobilized Ru(bpy)$_3^{2+}$ on (A) ITO plate and (B) ITO nanofilaments. CVs were done at 50 mV s^{-1} in 0.1M KCl water solution. The geometric surface area was 38.5 mm^2.*
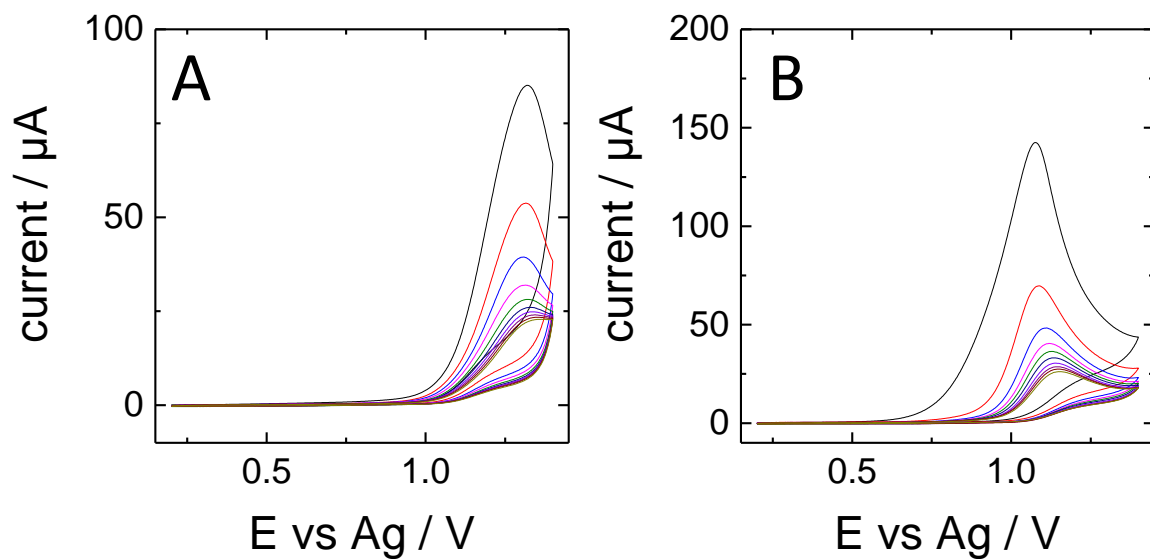
the flat one. Next, on Figure 5.14 there are presented electrochemical results of cycling in 1 mM solution of TPrA. Similarly to earlier experiments the potential is shifted around 100 mV towards less oxidizing for porous ITO (1.07 V vs 1.16 V) with peak currents being around 40 % higher. This additional increase compared to bare samples (from section 5.1.1) might be cause by additional preconcentration of TPrA by silica layer that is negatively charged. On the Figure 5.15 the ECL generation corresponding to cyclic voltammetry is presented. For flat

ITO the first peak is at $0.74*10^6$ cps and then it diminishes over 10 cycles to a plateau around $0.21*10^6$ cps. For porous ITO it starts at $4.57*10^6$ cps which is a 6 time increase, consistent with the amount of the increase of immobilized and electroactive Ru complex. But the ECL grows over next 4 cycles up to $5.96*10^6$ cps and only afterwards it starts to decrease and at 10th cycle it is still slightly higher than initially. This behavior is very unexpected and impossible to explain without a more detailed study. On Figure 5.16 similar cyclic voltammetry and ECL experiments are presented but for 10 mM concentration of TPrA. The initial peak currents for flat and porous ITO are respectively 274 and 280 µA which is a very small difference. On Figure 5.17 is portrayed the ECL response of both samples over 10 cycles. On the flat ITO the ECL starts at $3.65*10^6$ cps and plateaus at $0.38*10^6$ cps in the 10th cycle. For porous layers the first cycle emits ECL of $11.27*10^6$ cps which is about 3 times higher than flat electrode and then decreases to $6.25*10^6$ cps by the end. As mentioned, in cases of both 1 and 10 mM TPrA concentration there is bigger initial ECL emission, 6 and 3 times respectively. But more surprisingly it appears that ECL diminishes much more slowly with cycling on porous electrodes. Comparing 10th cycles, the ECL intensity in 1 mM of TPrA on ITO nanofilaments is 22 times higher than for flat ITO and for 10 mM TPrA it is 16 times higher.

Figure 5.14. *Cyclic voltammograms of click-immobilized Ru(bpy)$_3$$^{2+}$ and 1 mM TPrA on (A) ITO plate and (B) ITO nanofilaments. CVs were done at 50 mV s^{-1} in 0.1M KCl water solution. The geometric surface area was 38.5 mm^2.*
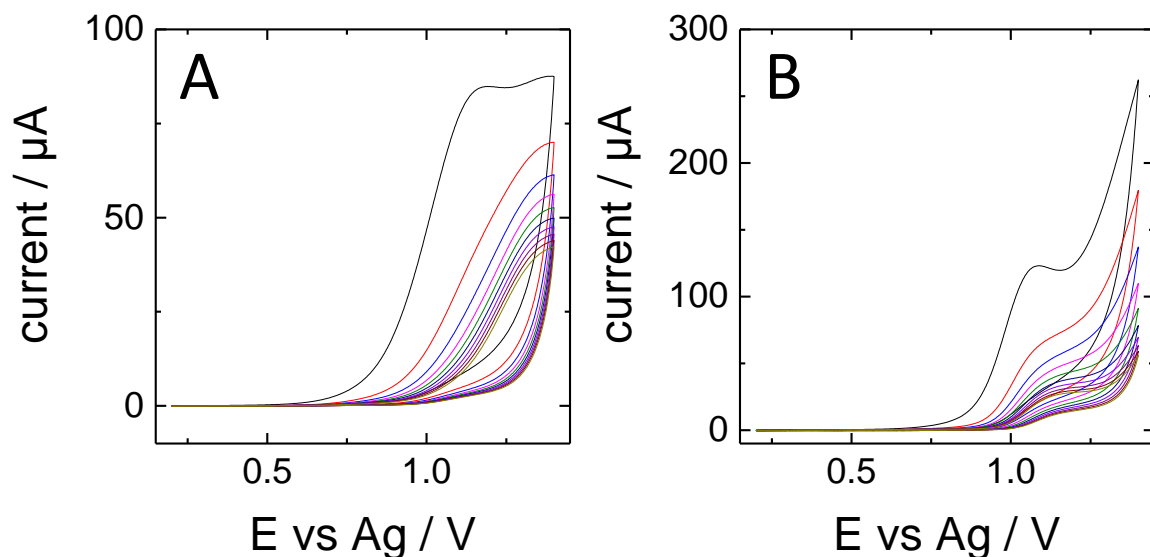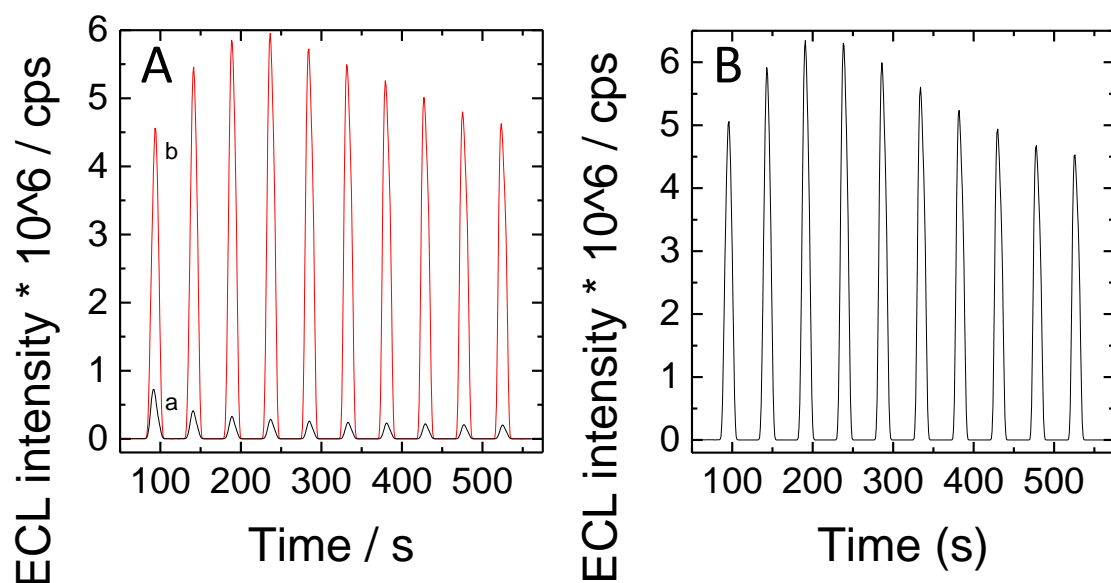
Figure 5.15. (A) ECL response during cyclic voltammetry (from Figure 5.8) of click-immobilized $Ru(bpy)_3^{2+}$ and 1 mM TPrA on (a) ITO plate and (b) ITO nanofilaments. (B) Repetition of (A)(b) after 15 minutes. The geometric surface area was 38.5 mm^2.
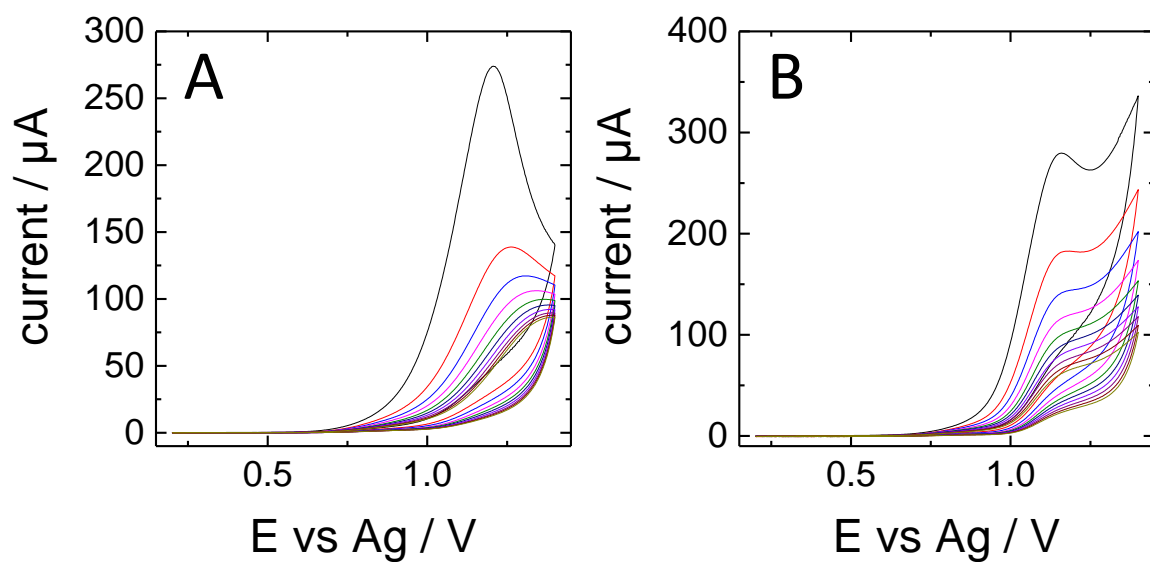
Figure 5.16. Cyclic voltammograms of click-immobilized $Ru(bpy)_3^{2+}$ and 10 mM TPrA on (A) ITO plate and (B) ITO nanofilaments. CVs were done at 50 mV s^{-1} in 0.1M KCl water solution. The geometric surface area was 38.5 mm^2.
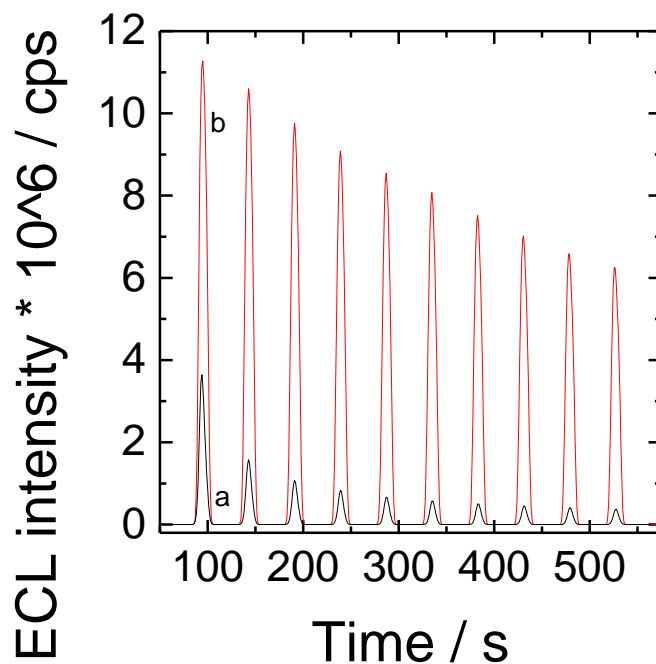
Figure 5.17. ECL response during cyclic voltammetry (from Figure 5.8) of click-immobilized Ru(bpy)$_3^{2+}$ and 10 mM TPrA on (a) ITO plate and (b) ITO nanofilaments. The geometric surface area was 38.5 mm^2.

We can also see that for the experiment with 10 mM of TPrA the rate of decay over 10 cycles is similar to that on reactants dissolved (Figure 5.3) which suggests that ruthenium is well-bound to the surface and the loss is very small and the decrease comes from dropping TPrA concentration rather than leakage of the luminophore. The effect is even more pronounced when the click-immobilized Ru (II) complex is compared with adsorbed one and 1 mM of TPrA is used. For covalently immobilized complex, there is almost no decay over 10 cycles, while on adsorbed one it goes down 6 times. This very much shows the superior stability of click-immobilized layers. Stability over longer periods of time is also compared in section 5.2.4. Figure 5.18 presents the correlation of voltage applied with ECL generation. Here, the onset of ECL starts at around 1.15 V which is later than ruthenium complex in the solution on unmodified nanofilaments (1.0 V) but earlier than the complex adsorbed on methylated silica (1.2 V). It rises continuously until the backscan approaches 1.3 V and then gradually diminishes. There is no peak visible during the back scan which suggests that there is no interference from the water oxidation. Finally, hysteresis of ECL is smaller than in case of adsorbed Ru complex, possibly because in this case luminophore is bound to the electrode and

thus circulates faster as the probability of reacting with TPrA radical generated on the electrode is higher.
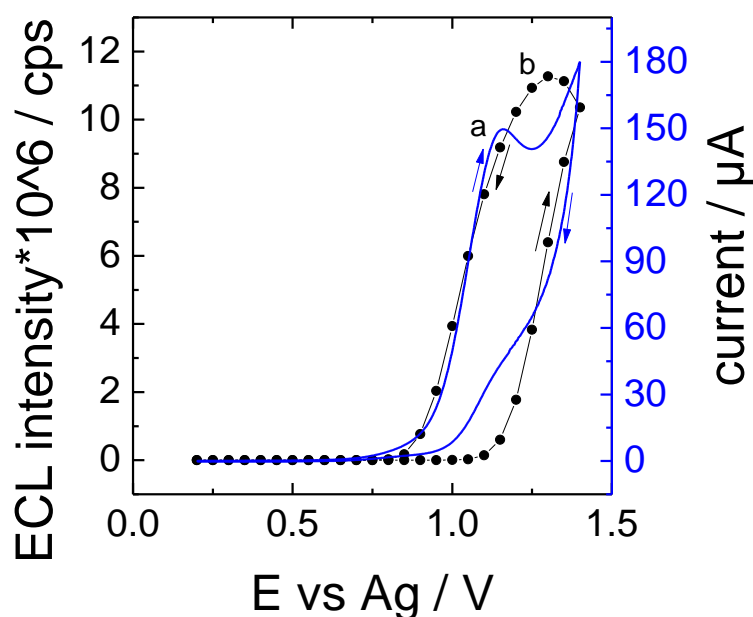
Figure 5.18. *(a) Cyclic voltammogram of click-immobilized Ru(bpy)$_3^{2+}$ in solution of 10 mM tripropylamine on ITO nanofilaments and (b) corresponding ECL generation.*

5.2.4. Stability comparison between adsorbed and covalently bound luminophore

Finally, to compare the stability of ECL response of complex adsorbed and click-immobilized over several cycles an additional measurement was performed. Here, to remove the influence of decreasing TPrA concentration over time, after each cycle the solution was briefly stirred to equalize the concentration at the electrode with the bulk solution. The results are presented on Figure 5.19. Here, each cycle was performed after 6 min stabilization period preceded by short stirring of the solution to equalize the TPrA concentration near the electrode with the bulk solution. It is noticeable that for the adsorbed complex, the ECL diminishes gradually with each cycle, suggesting that the complex is quickly desorbing with each cycle. On the contrary, the immobilized complex has a sharp decrease in activity in the 2nd cycle but then the response rises and stabilizes around 75 % of the original. This might suggest that the layer needs some preconditioning but in general is much more stable and the loss of the ruthenium complex is much smaller.
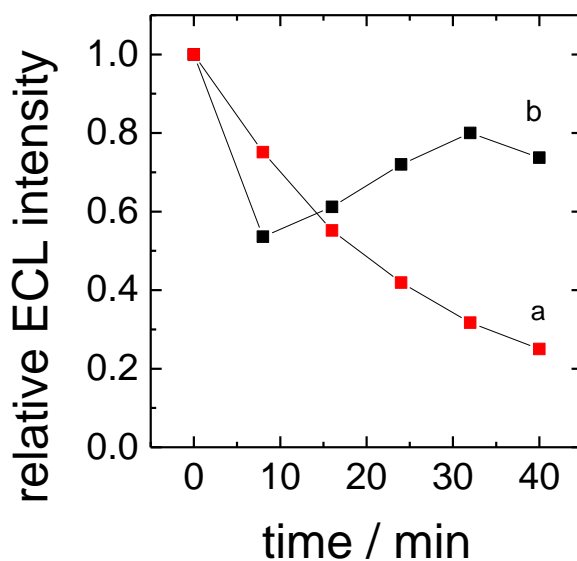
Figure 5.19. *Relative ECL intensity vs the cycle number with respect to the first cycle for (a) Ru(bpy)$_3$$^{2+}$ adsorbed on methylated silica from 10 µM solution for 15 min and (b) click-immobilized Ru(bpy)$_3$$^{2+}$, both measurements made in 10 mM TPrA.*

5.2.5. Possible explanations of the surprising phenomena

The unexpected enhancement of luminescence signal across all ECL experiments on porous electrodes, regardless of the source of Ru complex present in the system, cannot easily be explained by electrochemical measurements. It is especially visible in the first section where only slightly higher oxidation currents for both Ru (II) complex and TPrA mediator (40 and 20 % higher respectively) are registered. The ECL intensity increase is much higher than it could be expected from those measurements which when multiplied by each other would be about 68% (1,2*1,4=1,68). In practice the increase is 10 times bigger. In order to explain this, first of all, it needs to be established that of four proposed mechanisms of ECL generation in this system the dominant ones seem to be ones presented on Scheme 5.1 A and B, so ones where both the Ru (II) complex and TPrA need to be oxidized. Mechanism from Scheme 5.1 C might also contribute a small part but the concentration of the luminophore is probably too low for it to be significant. Mechanism D can be ruled out as it is clear that ECL generation does not occur at potentials too low for Ru (II) oxidation. Considering that, the possible explanation of higher ECL can be derived from those mechanisms. It is noticeable that in Ru(bpy)$_3$$^{2+}$ - TPrA system Ru(bpy)$_3$$^{2+}$ is regenerated after emitting the photon. This would mean that an initial increase of 40 % in oxidation currents of Ru (II) could be multiplied by

the presence of TPrA radical, leading to much higher ECL emission. Such an effect would be consistent with previous findings on ECL on macroporous nanofibrous electrodes.[183]

Another explanation is that if the desired reactant coming from TPrA oxidation that is TPrA* is generated deep within the porous network then it lowers the chance for the molecule to simply diffuse away from the electrode without reacting with the Ru complex like it could happen of flat ITO. Or, on the contrary, radical generated on top of the porous layer can diffuse inside of the pores rather than back into the solution. Finally, the much slower rate of decay of ECL signal over 10 cycles with click-immobilized Ru on porous electrodes compared to flat cannot be explained by electrochemical oxidation of TPrA itself since the electrochemical signal decay is comparable on both surfaces. This might be connected to general increase of ECL on porous substrate. Different modes of functionalization (with methylated or regular silica) can influence the diffusion parameters inside of the porous structure. Those additional layers can also ionically interact with the coreactant by attracting it and keeping it closer to Ruthenium (II).

5.3. Conclusions

To summarize, in this chapter an inquiry into ECL generation on ITO nanofilaments has been conducted and the improvement over flat electrode has been quantified. Firstly, bare electrodes were tested in the solution of $Ru(bpy)_3^{2+}$ as luminophore and TPrA as a coreactant. The emission intensity was found 7 times higher on the porous electrode. Next, the electrodes were covered with mesoporous methylated silica and the Ru complex was adsorbed on them. Depending on the concentration of the TPrA in the solution and the amount of adsorbed complex the improvement of the intensity was between 3 and 7 times. Furthermore, the Ru (II) complex was covalently bound to electrodes covered with silica through click-chemistry (in collaboration with Cheryl Karman). Depending on the concentration of TPrA, the signal enhancement was 3 to 6 times. Stability study was also performed and it was found that after 40 minutes the electrode with adsorbed Ru only maintained 25 % of its original ECL intensity while the electrode with covalently bound Ru (II) maintained 75 %. In each of the methods of ECL generation a slightly different dependence on the potential applied was found that points out to specific interactions of the silica layers with the ECL reactants and their precursors. It was also found out that in most cases during continuous cycling the porous layers had slower rate of decay compared to flat ones. This, together with the fact that in lower concentration of TPrA the improvement was also higher, suggests that the porous electrodes are less sensitive to the depletion of TPrA near the electrode. Combining those

conclusions together, one can postulate that porous ITO nanofilament electrodes could be useful in improving the signal in ECL-based sensors or reducing the needed amount of TPrA for proper functioning.

General conclusions and outlook

During the course of this PhD project an electrospun macroporous ITO electrode has been prepared by adapting available literature protocols. Firstly, a free-standing version was prepared. Here, nanofibers with diameter ranging from 110 to 235 nm have been obtained depending on the voltage applied. The thickness of the layer could also be adjusted by time of deposition. It was found that after calcination 500 °C an additional heat treatment at 1000 °C under nitrogen could increase conductivity by better sintering of the material (more interconnections) and introducing of the oxygen vacancies. The electrochemical properties were also improved as evidenced by redox reversibility of ferrocenedimethanol. Those electrospun mats were then characterized by X-ray diffractometry and scanning electron microscopy and later applied in electrochemical sensing of ascorbic acid with Sensitivity of 1.04 mA mM^{-1} cm^{-2}. Tests using Prussian blue have demonstrated the spectroelectrochemical capabilities of such prepared electrodes. Overall, the material possessed promising qualities but due to its inherent brittleness further manipulations and functionalization were difficult. To overcome this issue a revised deposition protocol was developed to fuse the layers with solid substrate. By introducing the polysterene film on the substrate delamination coming from calcination shrinkage was avoided and highly interconnected indium tin oxide nanofilaments have been obtained. They had a very different morphology compared to nanofibers, as the interaction with polysterene layer also caused the film to be more compact without losing the excellent electrochemical properties. Transparency in the visible light region up to 70 % upon submersion in water was also achieved. Those ITO nanofilaments deposited on fused silica were mechanically stable and provided a good electrode material that could be used for further electrochemical modifications and applications like the electrodeposition of a mesostructured methylated silica layer. After such functionalization the electrode was applied to spectroelectrochemical detection of industrial dyes with linear range of detection for methylene blue between 20 nM and 2 µM with limit of detection at 16.9 nM. A dynamic spectroelectrochemical measurement of adsorbed dye mixture was also made using the electrode which shows the potential of application in sensing in complex medium. Finally the electrochemiluminescence generation capabilities tested through three different systems show large improvement over the flat surface, up to 7 times depending on the concentrations of the reactants. It was also confirmed that covalently bound Ru complex is more stable over longer period of time than the adsorbed one.

Considering the improvement of analytical signals in spectroelectrochemical and ECL measurements by macroporous ITO electrodes it is worth exploring in the future a possibility of applying them in commercial sensors. However, certain drawbacks are obvious and need to be overcome in order to do that. One of those is lack of transparency in UV part of the spectrum that is characteristic to almost all of the TCOs. This excludes from detection a lot of molecules that do not possess absorption in the visible range and limits the sensing to colorful complexes or proteins. To overcome this issue another type of spectroscopy could be used like FT-IR. Surface enhanced Raman spectroscopy could also be an interesting direction as the exciting beam is in the visible light range and could penetrate the porous structure. Possibly the most interesting sensing application would be in systems that use ECL as a mechanism of detection. Sensors based on this effect already have very high sensitivity as the singular electrochemical redox act can result in emission of multiple photons per analyte through the circulation of the luminophore (eg. $Ru(bpy)_3^{2+}$ or luminol). First tests have shown that ITO nanofilament electrodes are capable of magnifying such signal even more, and the enhancement is particularly visible at lower concentrations of the coreactant. This provides another benefit as it could reduce the cost of the sensor and makes it safer because the most commonly used coreactant, tripropylamine, is a compound toxic to humans.

Conclusions générales et perspectives

Au cours de ces travaux de thèse, une électrode macroporeuse d'ITO a été préparée par électrofilage en adaptant les protocoles disponibles dans la littérature. Un premier type d'électrodes auto-supportées a été préparée. Ces électrodes sont constituées de nanofibres de diamètre dépendant de la tension appliquée (de 110 à 235 nm). La variation du temps de dépôt quant à lui permet de contrôler l'épaisseur de la couche de nanofibres. Une calcination de la couche électrofilée à 500°C est nécessaire afin d'obtenir les nanofibres d'ITO. Cependant un traitement thermique supplémentaire à 1000 ° C sous azote permet d'augmenter la conductivité en améliorant le frittage du matériau (plus d'interconnexions) et introduisant des sites vacants en oxygène. Ce traitement à 1000°C permet également d'améliorer les propriétés électrochimiques, comme en témoigne la réversibilité redox du ferrocèneméthanol. Ces couches électrofilées ont ensuite été caractérisées par diffraction des rayons X et microscopie électronique à balayage avant d'être utilisée pour la détection électrochimique de l'acide ascorbique avec une sensibilité de 1,04 mA mM^{-1} cm^{-2}.

Les tests réalisés avec le bleu de Prusse ont démontré les capacités spectroélectrochimiques de telles électrodes. Dans l'ensemble, les électrodes à base de nanofibres d'ITO possédaient des caractéristiques prometteuses. Cependant en raison de leur fragilité inhérente, d'autres manipulations et fonctionnalisations furent difficiles. Pour contourner cette difficulté, un protocole de dépôt a été développé afin d'obtenir une meilleure adhérence des couches électrofilées sur un substrat solide. L'utilisation d'un film de polystyrène sur le substrat a permis d'éviter le délaminage lors de la calcination du dépôt. Cette approche a conduit à la formation de nanofilaments fortement interconnectés d'oxyde d'indium dopé à l'étain. L'interaction avec la couche de polystyrène induit une morphologie du dépôt très différente de celle des nanofibres rendant le film plus compact sans perdre les excellentes propriétés électrochimiques. La transmittance dans la région de la lumière visible peut atteindre 70% lors de la submersion de l'échantillon dans l'eau. Les nanofilaments d'ITO déposés sur un verre de silice fondue sont mécaniquement stables et fournissent un bon matériau d'électrode pouvant être modifié pour d'autres applications électrochimiques. Cette stabilité mécanique a permis l'électrodépôt d'une couche de silice méthylée et mésostructurée. Après une telle fonctionnalisation, ce type d'électrodes fut utilisé pour la détection spectroélectrochimique de colorants industriels avec une plage linéaire de détection pour le bleu de méthylène allant de 20 nM à 2 μM avec une limite de détection de 16,9 nM. Une mesure spectroélectrochimique dynamique utilisant ce type d'électrode a également été réalisée sur un mélange de colorants

adsorbés. Les résultats obtenus montrent le potentiel d'application dans la détection en milieu complexe de tels systèmes. Enfin, en comparaison à une électrode plane d'ITO, les systèmes utilisant des nanofilaments d'ITO présentent une forte amélioration de la capacité de génération d'électrochimiluminescence (jusqu'à 7 fois en fonction des concentrations en réactifs). Il a également été confirmé que la stabilisation par liaison covalente du complexe Ru est robuste sur une période de temps plus longue que celle obtenue pour le complexe adsorbé.

Compte tenu de l'amélioration des signaux analytiques pour les mesures spectroélectrochimiques et ECL par des électrodes ITO macroporeuses, il convient d'explorer à l'avenir les possibilités d'applications dans des capteurs médicaux ou environmentaux. Cependant, avant de le faire, certains inconvénients évidents doivent être surmontés. L'un d'entre eux est le manque de transparence dans la partie UV du spectre qui est caractéristique de la quasi-totalité des TCO. Cela exclut de détecter beaucoup de molécules qui ne possèdent pas d'absorption dans la gamme visible et limitent la détection à celle des complexes et/ou protéines colorés. Pour contourner cette difficulté, un autre type de spectroscopie pourrait être utilisé comme la spectroscopie FT-IR. La spectroscopie Raman de surface exaltée pourrait également être une direction intéressante car le faisceau incident est dans la région spectrale de la lumière visible et pourrait pénétrer dans la structure poreuse. L'application de systèmes utilisant l'ECL comme mécanisme de détection pourrait être la plus intéressante. Les capteurs basés sur cet effet ont déjà une sensibilité très élevée car la réaction électrochimique peut entraîner l'émission de photons multiples par analyte par la circulation du luminophore (par exemple $Ru(bpy)_3^{2+}$ ou luminol). Les premiers tests ont montré que les électrodes à base de nanofilaments d'ITO sont capables d'augmenter significativement ce signal, et cette amélioration est particulièrement visible pour des concentrations plus faibles en co-réactif.

Bibliography

(1)   Kaim, W.; Fiedler, J. Spectroelectrochemistry: The Best of Two Worlds. *Chem. Soc. Rev.* **2009**, *38* (12), 3373–3382.

(2)   Zhan, R.; Song, S.; Liu, Y.; Dong, S. Mechanisms of Methylene Blue Electrode Processes Studied by in Situ Electron Paramagnetic Resonance and Ultraviolet-Visible Spectroelectrochemistry. *J. Chem. Soc. Faraday Trans.* **1990**, *86* (18), 3125–3127.

(3)   Shi, Y.; Slaterbeck, A. F.; Seliskar, C. J.; Heineman, W. R. Spectroelectrochemical Sensing Based on Multimode Selectivity Simultaneously Achievable in a Single Device. 1. Demonstration of Concept with Ferricyanide. *Anal. Chem.* **1997**, *69* (18), 3679–3686.

(4)   Topoglidis, E.; Astuti, Y.; Duriaux, F.; Grätzel, M.; Durrant, J. R. Direct Electrochemistry and Nitric Oxide Interaction of Heme Proteins Adsorbed on Nanocrystalline Tin Oxide Electrodes. *Langmuir* **2003**, *19* (17), 6894–6900.

(5)   Mažeikien, R.; Niaura, G.; Malinauskas, A. Electrocatalytic Reduction of Hydrogen Peroxide at Prussian Blue Modified Electrode: An in Situ Raman Spectroelectrochemical Study. *J. Electroanal. Chem.* **2011**, *660* (1), 140–146.

(6)   Smieja, J. M.; Kubiak, C. P. Re(bipy-tBu)(CO)3Cl-Improved Catalytic Activity for Reduction of Carbon Dioxide: IR-Spectroelectrochemical and Mechanistic Studies. *Inorg. Chem.* **2010**, *49* (20), 9283–9289.

(7)   Garoz-Ruiz, J.; Heras, A.; Palmero, S.; Colina, A. Development of a Novel Bidimensional Spectroelectrochemistry Cell Using Transfer Single-Walled Carbon Nanotubes Films as Optically Transparent Electrodes. *Anal. Chem.* **2015**, *87* (12), 6233–6239.

(8)   Garoz-Ruiz, J.; Izquierdo, D.; Colina, A.; Palmero, S.; Heras, A. Optical Fiber Spectroelectrochemical Device for Detection of Catechol at Press-Transferred Single-Walled Carbon Nanotubes Electrodes. *Anal. Bioanal. Chem.* **2013**, *405* (11), 3593–3602.

(9)   Ibañez, D.; Santidrian, A.; Heras, A.; Kalbáč, M.; Colina, A. Study of Adenine and Guanine Oxidation Mechanism by Surface-Enhanced Raman Spectroelectrochemistry. *J. Phys. Chem. C* **2015**, *119* (15), 8191–8198.

(10)   Krejčik, M.; Daněk, M.; Hartl, F. Simple Construction of an Infrared Optically Transparent Thin-Layer Electrochemical Cell. Applications to the Redox Reactions of Ferrocene, Mn2(CO)10 and Mn(CO)3(3,5-Di-T-Butyl-Catecholate)-. *J. Electroanal. Chem.* **1991**, *317* (1–2), 179–187.

(11)   Wu, J.-W.; Mei, W.-J.; Yan, Z.-H.; Liu, J.-C.; Li, H. In Situ Spectroelectrochemical Monitoring during the Electrocatalytic Oxidation of Guanine on [Ru(bpy)2(MPyTMPP)Cl]+/ITO Electrode. *J. Electroanal. Chem.* **2013**, *697*, 21–27.

(12)   Hu, L.; Xu, G. Applications and Trends in Electrochemiluminescence. *Chem. Soc. Rev.* **2010**, *39* (8), 3275–3304.

(13)   Müller, V.; Rathousky, J.; Fattakhova-Rohlfing, D. Covalent Immobilization of Redox Protein within the Mesopores of Transparent Conducting Electrodes. *Electrochim. Acta* **2014**, *116*, 1–8.

(14) Goebbert, C.; Bisht, H.; Al-Dahoudi, N.; Nonninger, R.; Aegerter, M. A.; Schmidt, H. Wet Chemical Deposition of Crystalline, Redispersable ATO and ITO Nanoparticles. *J. Sol-Gel Sci. Technol.* **2000**, *19* (1–3), 201–204.

(15) Fattakhova-Rohlfing, D.; Brezesinski, T.; Rathouský, J.; Feldhoff, A.; Oekermann, T.; Wark, M.; Smarsly, B. Transparent Conducting Films of Indium Tin Oxide with 3D Mesopore Architecture. *Adv. Mater.* **2006**, *18* (22), 2980–2983.

(16) Leem, J. W.; Yu, J. S. Glancing Angle Deposited ITO Films for Efficiency Enhancement of a-Si:H/μc-Si:H Tandem Thin Film Solar Cells. *Opt. Express* **2011**, *19 Suppl 3*, A258–A268.

(17) Ostermann, R.; Zieba, R.; Rudolph, M.; Schlettwein, D.; Smarsly, B. M. Electrospun Antimony Doped Tin Oxide (ATO) Nanofibers as a Versatile Conducting Matrix. *Chem. Commun. (Camb).* **2011**, *47* (44), 12119–12121.

(18) Kang, J. H.; Ryu, J. H.; Kim, H. K.; Kim, H. Y.; Han, N.; Lee, M. S.; Park, Y. J.; Uthirakumar, P.; Lysak, V. V.; Hong, C. H. Enhancement of Light Output Power in GaN-Based Light-Emitting Diodes Using Indium Tin Oxide Films with Nanoporous Structures. *Thin Solid Films* **2011**, *520* (1), 437–441.

(19) Walcarius, A.; Sibottier, E.; Etienne, M.; Ghanbaja, J. Electrochemically Assisted Self-Assembly of Mesoporous Silica Thin Films. *Nat. Mater.* **2007**, *6* (8), 602–608.

(20) Hecht, D. S.; Hu, L.; Irvin, G. Emerging Transparent Electrodes Based on Thin Films of Carbon Nanotubes, Graphene, and Metallic Nanostructures. *Adv. Mater.* **2011**, *23* (13), 1482–1513.

(21) Cao, W.; Li, J.; Chen, H.; Xue, J. Transparent Electrodes for Organic Optoelectronic Devices: A Review. *J. Photonics Energy* **2014**, *4* (1), 40990.

(22) Lee, J.-K.; Yang, M. Progress in Light Harvesting and Charge Injection of Dye-Sensitized Solar Cells. *Mater. Sci. Eng. B* **2011**, *176* (15), 1142–1160.

(23) Gross, M.; Winnacker, A.; Wellmann, P. J. Electrical, Optical and Morphological Properties of Nanoparticle Indium–tin–oxide Layers. *Thin Solid Films* **2007**, *515* (24), 8567–8572.

(24) Buonsanti, R.; Pick, T. E.; Krins, N.; Richardson, T. J.; Helms, B. A.; Milliron, D. J. Assembly of Ligand-Stripped Nanocrystals into Precisely Controlled Mesoporous Architectures. *Nano Lett.* **2012**, *12* (7), 3872–3877.

(25) Dickey, M. D.; Weiss, E. A.; Smythe, E. J.; Chiechi, R. C.; Capasso, F.; Whitesides, G. M. Fabrication of Arrays of Metal and Metal Oxide Nanotubes by Shadow Evaporation. *ACS Nano* **2008**, *2* (4), 800–808.

(26) Xie, L.; Shao, Y.; Xiao, X.; Zhang, L.; Bi, X.; Zhang, S. Fabrication of Indium-Tin-Oxide Thin-Film Transistor Using Anodization. *Proc. AM-FPD 2014 - 21st Int. Work. Act. Flatpanel Displays Devices TFT Technol. FPD Mater.* **2014**, *1*, 101–103.

(27) Jin, M.-J.; Ma, T.; Ling, T.; Qiao, S.-Z.; Du, X.-W. Three-Dimensional Networks of ITO/CdS Coaxial Nanofibers for Photovoltaic Applications. *J. Mater. Chem.* **2012**, *22* (26), 13057–13063.

(28) Chappel, S.; Grinis, L.; Ofir, A.; Zaban, A. Extending the Current Collector into the Nanoporous Matrix of Dye Sensitized Electrodes. *J. Phys. Chem. B* **2005**, *109* (5), 1643–1647.

(29)   Kato, M.; Cardona, T.; Rutherford, a W.; Reisner, E. Photoelectrochemical Water Oxidation with Photosystem II Integrated in a Mesoporous Indium Tin Oxide Electrode. *J. Am. Chem. Soc.* **2012**, *134*, 8332–8335.

(30)   Sadeh, A.; Sladkevich, S.; Gelman, F.; Prikhodchenko, P.; Baumberg, I.; Berezin, O.; Lev, O. Sol- Gel-Derived Composite Antimony-Doped, Tin Oxide-Coated Clay-Silicate Semitransparent and Conductive Electrodes. *Anal. Chem.* **2007**, *79* (14), 5188–5195.

(31)   Chappel, S.; Chen, S.-G.; Zaban, A. TiO 2 -Coated Nanoporous SnO 2 Electrodes for Dye-Sensitized Solar Cells. *Langmuir* **2002**, *18* (8), 3336–3342.

(32)   Hosono, H.; Ohta, H.; Orita, M.; Ueda, K.; Hirano, M. Frontier of Transparent Conductive Oxide Thin Films. *Vacuum* **2002**, *66* (3–4), 419–425.

(33)   Ellmer, K. Past Achievements and Future Challenges in the Development of Optically Transparent Electrodes. *Nat. Photonics* **2012**, *6* (12), 808–816.

(34)   Gokulakrishnan, V.; Parthiban, S.; Jeganathan, K.; Ramamurthi, K. Investigations on the Structural, Optical and Electrical Properties of Nb-Doped SnO2 Thin Films. *J. Mater. Sci.* **2011**, *46* (16), 5553–5558.

(35)   Minami, T.; Nanto, H.; Takata, S. Highly Conductive and Transparent Aluminum Doped Zinc Oxide Thin Films Prepared by RF Magnetron Sputtering. *Jap. J. Appl. Phys.* **1984**, *23* (Part 2, No. 1), L280.

(36)   Hu, J.; Gordon, R. G. Chemical Vapor Deposition of Highly Transparent and Conductive Boron Doped Zinc Oxide Thin Films. *MRS Proc.* **1992**, *242*, 743.

(37)   Niedziolka, J.; Szot, K.; Marken, F.; Opallo, M. A Porous ITO Nanoparticles Modified Electrode for the Redox Liquid Immobilization. *Electroanalysis* **2007**, *19* (2–3), 155–160.

(38)   Ederth, J.; Heszler, P.; Hultåker, A.; Niklasson, G. .; Granqvist, C. . Indium Tin Oxide Films Made from Nanoparticles: Models for the Optical and Electrical Properties. *Thin Solid Films* **2003**, *445* (2), 199–206.

(39)   Hoertz, P. G.; Chen, Z.; Kent, C. A.; Meyer, T. J. Application of High Surface Area Tin-Doped Indium Oxide Nanoparticle Films as Transparent Conducting Electrodes. *Inorg. Chem.* **2010**, *49* (18), 8179–8181.

(40)   Kőrösi, L.; Papp, S.; Beke, S.; Pécz, B.; Horváth, R.; Petrik, P.; Agócs, E.; Dékány, I. Highly Transparent ITO Thin Films on Photosensitive Glass: Sol–gel Synthesis, Structure, Morphology and Optical Properties. *Appl. Phys. A* **2012**, *107* (2), 385–392.

(41)   Liu, S.; Ding, W.; Gu, Y.; Chai, W. Effect of Sb Doping on the Microstructure and Optoelectrical Properties of Sb-Doped SnO 2 Films Prepared by Spin Coating. *Phys. Scr.* **2012**, *85* (6), 65601.

(42)   Bubenhofer, S. B.; Schumacher, C. M.; Koehler, F. M.; Luechinger, N. A.; Sotiriou, G. A.; Grass, R. N.; Stark, W. J. Electrical Resistivity of Assembled Transparent Inorganic Oxide Nanoparticle Thin Layers: Influence of Silica, Insulating Impurities, and Surfactant Layer Thickness. *ACS Appl. Mater. Interfaces* **2012**, *4* (5), 2664–2671.

(43)   Guo, J.; She, C.; Lian, T. Ultrafast Electron Transfer between Molecule Adsorbate and Antimony Doped Tin Oxide (ATO) Nanoparticles. *J. Phys. Chem. B* **2005**, *109* (15), 7095–7102.

(44) Kato, M.; Cardona, T.; Rutherford, A. W.; Reisner, E. Covalent Immobilization of Oriented Photosystem II on a Nanostructured Electrode for Solar Water Oxidation. *J. Am. Chem. Soc.* **2013**, *135* (29), 10610–10613.

(45) Gonzalez-Arribas, E.; Aleksejeva, O.; Bobrowski, T.; Toscano, M. D.; Gorton, L.; Schuhmann, W.; Shleev, S. Solar Biosupercapacitor. *Electrochem. commun.* **2017**, *74*, 9–13.

(46) Tao, R.; Tomita, T.; Wong, R. A.; Waki, K. Electrochemical and Structural Analysis of Al-Doped ZnO Nanorod Arrays in Dye-Sensitized Solar Cells. *J. Power Sources* **2012**, *214*, 159–165.

(47) Chen, H.; Zhu, L.; Li, W.; Liu, H. A Three-Dimensional Electrode for Photoelectrochemical Cell: TiO2 Coated ITO Mesoporous Film. *Mater. Lett.* **2010**, *64* (6), 781–784.

(48) Chen, H.; Zhu, L.; Li, W.; Liu, H. Synthesis and Photoelectrochemical Behavior of CdS Quantum Dots-Sensitized Indium-Tin-Oxide Mesoporous Film. *Curr. Appl. Phys.* **2012**, *12* (1), 129–133.

(49) Huang, Z.; He, M.; Yu, M.; Click, K.; Beauchamp, D.; Wu, Y. Dye-Controlled Interfacial Electron Transfer for High-Current Indium Tin Oxide Photocathodes. *Angew. Chemie Int. Ed.* **2015**, *54* (23), 6857–6861.

(50) Yang, Z.; Gao, S.; Li, T.; Liu, F. Q.; Ren, Y.; Xu, T. Enhanced Electron Extraction from Template-Free 3D Nanoparticulate Transparent Conducting Oxide (TCO) Electrodes for Dye-Sensitized Solar Cells. *ACS Appl. Mater. Interfaces* **2012**, *4* (8), 4419–4427.

(51) Farnum, B. H.; Morseth, Z. A.; Lapides, A. M.; Rieth, A. J.; Hoertz, P. G.; Brennaman, M. K.; Papanikolas, J. M.; Meyer, T. J. Photoinduced Interfacial Electron Transfer within a Mesoporous Transparent Conducting Oxide Film. *J. Am. Chem. Soc.* **2014**, *136* (6), 2208–2211.

(52) Xiao, M.; Huang, F.; Xiang, W.; Cheng, Y. B.; Spiccia, L. Enhanced Charge Collection in Dye-Sensitized Solar Cells Utilizing Collector-Shell Electrodes. *J. Power Sources* **2015**, *277*, 343–349.

(53) Forman, A. J.; Chen, Z.; Chakthranont, P.; Jaramillo, T. F. High Surface Area Transparent Conducting Oxide Electrodes with a Customizable Device Architecture. *Chem. Mater.* **2014**, *26* (2), 958–964.

(54) Pohl, A.; Dunn, B. Mesoporous Indium Tin Oxide (ITO) Films. *Thin Solid Films* **2006**, *515* (2), 790–792.

(55) Zhang, X.; Wu, W.; Tian, T.; Man, Y.; Wang, J. Deposition of Transparent Conductive Mesoporous Indium Tin Oxide Thin Films by a Dip Coating Process. *Mater. Res. Bull.* **2008**, *43* (4), 1016–1022.

(56) Fattakhova-Rohlfing, D.; Brezesinski, T.; Smarsly, B.; Rathouský, J. Template-Assisted Preparation of Films of Transparent Conductive Indium Tin Oxide. *Superlattices Microstruct.* **2008**, *44* (4–5), 686–692.

(57) Frasca, S.; von Graberg, T.; Feng, J. J.; Thomas, A.; Smarsly, B. M.; Weidinger, I. M.; Scheller, F. W.; Hildebrandt, P.; Wollenberger, U. Mesoporous Indium Tin Oxide as a Novel Platform for Bioelectronics. *ChemCatChem* **2010**, *2* (7), 839–845.

(58) Graberg, T. Von; Hartmann, P.; Rein, A.; Gross, S.; Seelandt, B.; Röger, C.; Zieba, R.; Traut, A.; Wark, M.; Janek, J.; Smarsly, B. M. Mesoporous Tin-Doped Indium Oxide Thin Films: Effect of Mesostructure on Electrical Conductivity. *Sci. Technol. Adv. Mater.* **2011**, *12* (2), 25005.

(59) Hamd, W.; Chavarot-Kerlidou, M.; Fize, J.; Muller, G.; Leyris, A.; Matheron, M.; Courtin, E.; Fontecave, M.; Sanchez, C.; Artero, V.; Laberty-Robert, C. Dye-Sensitized Nanostructured Crystalline Mesoporous Tin-Doped Indium Oxide Films with Tunable Thickness for Photoelectrochemical Applications. *J. Mater. Chem. A* **2013**, *1* (28), 8217–8225.

(60) Wang, Y.; Brezesinski, T.; Antonietti, M.; Smarsly, B. Ordered Mesoporous Sb-, Nb-, and Ta-Doped SnO2 Thin Films with Adjustable Doping Levels and High Electrical Conductivity. *ACS Nano* **2009**, *3* (6), 1373–1378.

(61) Hou, K.; Puzzo, D. D.; Helander, M. G. C.; Lo, S. S.; Bonifacio, L. D.; Wang, W.; Lu, Z. H.; Scholes, G. D.; Ozin, G. A. G. A. Dye-Anchored Mesoporous Antimony-Doped Tin Oxide Electrochemiluminescence Cell. *Adv. Mater.* **2009**, *21* (24), 2492–2496.

(62) Ueno, N.; Dwijaya, B.; Uchida, Y.; Egashira, Y.; Nishiyama, N. Synthesis of Mesoporous ZnO, AZO, and BZO Transparent Conducting Films Using Nonionic Triblock Copolymer as Template. *Mater. Lett.* **2013**, *100*, 111–114.

(63) Suzuki, N.; Kamachi, Y.; Chiang, Y.-D.; Wu, K. C.-W.; Ishihara, S.; Sato, K.; Fukata, N.; Matsuura, M.; Maekawa, K.; Tanabe, H.; Ariga, K.; Yamauchi, Y. Synthesis of Mesoporous Antimony-Doped Tin Oxide (ATO) Thin Films and Investigation of Their Electrical Conductivity. *CrystEngComm* **2013**, *15* (22), 4404.

(64) Aksu, Y.; Frasca, S.; Wollenberger, U.; Driess, M.; Thomas, A. A Molecular Precursor Approach to Tunable Porous Tin-Rich Indium Tin Oxide with Durable High Electrical Conductivity for Bioelectronic Devices. *Chem. Mater.* **2011**, *23* (7), 1798–1804.

(65) Volosin, A. M.; Sharma, S.; Traverse, C.; Newman, N.; Seo, D.-K. One-Pot Synthesis of Highly Mesoporous Antimony-Doped Tin Oxide from Interpenetrating Inorganic/organic Networks. *J. Mater. Chem.* **2011**, *21* (35), 13232.

(66) Sharma, S.; Volosin, A.; Schmitt, D.; Seo, D.-K. S. Preparation and Electrochemical Properties of Nanoporous Transparent Antimony-Doped Tin Oxide (ATO) Coatings. *J. Mater. Chem. A* **2013**, 699–706.

(67) Kwan, P.; Schmitt, D.; Volosin, A. M.; McIntosh, C. L.; Seo, D.-K.; Jones, A. K. Spectroelectrochemistry of Cytochrome c and Azurin Immobilized in Nanoporous Antimony-Doped Tin Oxide. *Chem. Commun.* **2011**, *47* (45), 12367–12369.

(68) Carey, A. M.; Zhang, H.; Mieritz, D.; Volosin, A.; Gardiner, A. T.; Cogdell, R. J.; Yan, H.; Seo, D. K.; Lin, S.; Woodbury, N. W. Photocurrent Generation by Photosynthetic Purple Bacterial Reaction Centers Interfaced with a Porous Antimony-Doped Tin Oxide (ATO) Electrode. *ACS Appl. Mater. Interfaces* **2016**, *8* (38), 25104–25110.

(69) Müller, V.; Rasp, M.; Rathouský, J.; Schütz, B.; Niederberger, M.; Fattakhova-Rohlfing, D. Transparent Conducting Films of Antimony-Doped Tin Oxide with Uniform Mesostructure Assembled from Preformed Nanocrystals. *Small* **2010**, *6* (5), 633–637.

(70) Liu, Y.; Štefanić, G.; Rathouský, J.; Hayden, O.; Bein, T.; Fattakhova-Rohlfing, D. Assembly of Mesoporous Indium Tin Oxide Electrodes from Nano-Hydroxide

Building Blocks. *Chem. Sci.* **2012**, *3* (7), 2367–2374.

(71) Peters, K.; Lokupitiya, H. N.; Sarauli, D.; Labs, M.; Pribil, M.; Rathouský, J.; Kuhn, A.; Leister, D.; Stefik, M.; Fattakhova-Rohlfing, D. Nanostructured Antimony-Doped Tin Oxide Layers with Tunable Pore Architectures as Versatile Transparent Current Collectors for Biophotovoltaics. *Adv. Funct. Mater.* **2016**, *26* (37), 6682–6692.

(72) Wang, H.-W.; Ting, C.-F.; Hung, M.-K.; Chiou, C.-H.; Liu, Y.-L.; Liu, Z.; Ratinac, K. R.; Ringer, S. P. Three-Dimensional Electrodes for Dye-Sensitized Solar Cells: Synthesis of Indium-Tin-Oxide Nanowire Arrays and ITO/TiO2 Core-Shell Nanowire Arrays by Electrophoretic Deposition. *Nanotechnology* **2009**, *20* (5), 55601.

(73) Arsenault, E.; Soheilnia, N.; Ozin, G. A. Periodic Macroporous Nanocrystalline Antimony-Doped Tin Oxide Electrode. *ACS Nano* **2011**, *5* (4), 2984–2988.

(74) Yang, Z.; Gao, S.; Li, W.; Vlasko-Vlasov, V.; Welp, U.; Kwok, W.-K.; Xu, T. Three-Dimensional Photonic Crystal Fluorinated Tin Oxide (FTO) Electrodes: Synthesis and Optical and Electrical Properties. *ACS Appl. Mater. Interfaces* **2011**, *3* (4), 1101–1108.

(75) Jiang, Q.; Liu, F.; Li, T.; Xu, T. Fast and Low Voltage-Driven Solid-State Electrochromics Using 3-D Conductive FTO Nanobead Electrodes. *J. Mater. Chem. C* **2014**, *2* (4), 618–621.

(76) Moir, J.; Soheilnia, N.; O'Brien, P.; Jelle, A.; Grozea, C. M.; Faulkner, D.; Helander, M. G.; Ozin, G. A. Enhanced Hematite Water Electrolysis Using a 3D Antimony-Doped Tin Oxide Electrode. *ACS Nano* **2013**, *7* (5), 4261–4274.

(77) Liu, Y.; Peters, K.; Mandlmeier, B.; Müller, A.; Fominykh, K.; Rathousky, J.; Scheu, C.; Fattakhova-Rohlfing, D. Macroporous Indium Tin Oxide Electrode Layers as Conducting Substrates for Immobilization of Bulky Electroactive Guests. *Electrochim. Acta* **2014**, *140*, 108–115.

(78) Peters, K.; Zeller, P.; Stefanic, G.; Skoromets, V.; Němec, H.; Kužel, P.; Fattakhova-Rohlfing, D. Water-Dispersible Small Monodisperse Electrically Conducting Antimony Doped Tin Oxide Nanoparticles. *Chem. Mater.* **2015**, *27* (3), 1090–1099.

(79) Mersch, D.; Lee, C. Y.; Zhang, J. Z.; Brinkert, K.; Fontecilla-Camps, J. C.; Rutherford, A. W.; Reisner, E. Wiring of Photosystem II to Hydrogenase for Photoelectrochemical Water Splitting. *J. Am. Chem. Soc.* **2015**, *137* (26), 8541–8549.

(80) Stieger, K. R.; Feifel, S. C.; Lokstein, H.; Hejazi, M.; Zouni, A.; Lisdat, F. Biohybrid Architectures for Efficient Light-to-Current Conversion Based on Photosystem I within Scalable 3D Mesoporous Electrodes. *J. Mater. Chem. A* **2016**, *4*, 17009–17017.

(81) Sokol, K.; Mersch, D.; Hartmann, V.; Zhang, J. Z.; Nowaczyk, M. M.; Roegner, M.; Ruff, A.; Schuhmann, W.; Plumere, N.; Reisner, E. Rational Wiring of Photosystem II to Hierarchical Indium Tin Oxide Electrodes Using Redox Polymers. *Energy Environ. Sci.* **2016**, *16* (12), 1027–1033.

(82) Naghavi, N. On the Electrochromic Properties of Antimony–tin Oxide Thin Films Deposited by Pulsed Laser Deposition. *Solid State Ionics* **2003**, *156* (3–4), 463–474.

(83) Gondoni, P.; Mazzolini, P.; Russo, V.; Petrozza, A.; Srivastava, A. K.; Li Bassi, A.; Casari, C. S. Enhancing Light Harvesting by Hierarchical Functionally Graded Transparent Conducting Al-Doped ZnO Nano- and Mesoarchitectures. *Sol. Energy Mater. Sol. Cells* **2014**, *128*, 248–253.

(84) Gondoni, P.; Mazzolini, P.; Russo, V.; Diani, M.; Amati, M.; Gregoratti, L.; De Renzi, V.; Gazzadi, G. C.; Martí-Rujas, J.; Li Bassi, A.; Casari, C. S. Tuning Electrical Properties of Hierarchically Assembled Al-Doped ZnO Nanoforests by Room Temperature Pulsed Laser Deposition. *Thin Solid Films* **2015**, *594*, 12–17.

(85) Gondoni, P.; Ghidelli, M.; Di Fonzo, F.; Carminati, M.; Russo, V.; Li Bassi, A.; Casari, C. S. Structure-Dependent Optical and Electrical Transport Properties of Nanostructured Al-Doped ZnO. *Nanotechnology* **2012**, *23* (36), 365706.

(86) Garvey, T. R.; Farnum, B. H.; Lopez, R. Pulsed Laser Deposited Porous Nano-Carpets of Indium Tin Oxide and Their Use as Charge Collectors in Core–shell Structures for Dye Sensitized Solar Cells. *Nanoscale* **2015**, *7* (6), 2400–2408.

(87) Joanni, E.; Savu, R.; de Sousa Góes, M.; Bueno, P. R.; de Freitas, J. N.; Nogueira, A. F.; Longo, E.; Varela, J. A. Dye-Sensitized Solar Cell Architecture Based on Indium-Tin Oxide Nanowires Coated with Titanium Dioxide. *Scr. Mater.* **2007**, *57* (3), 277–280.

(88) Yun, J.; Park, Y. H.; Bae, T.-S.; Lee, S.; Lee, G.-H. Fabrication of a Completely Transparent and Highly Flexible ITO Nanoparticle Electrode at Room Temperature. *ACS Appl. Mater. Interfaces* **2013**, *5* (1), 164–172.

(89) Wang, W.; Bae, T.-S.; Park, Y. H.; Kim, D. H.; Lee, S.; Min, G.; Lee, G.-H.; Song, M.; Yun, J. Highly Efficient and Bendable Organic Solar Cells Using a Three-Dimensional Transparent Conducting Electrode. *Nanoscale* **2014**, *6* (12), 6911–6924.

(90) Malek, G. A.; Aytug, T.; Liu, Q.; Wu, J. Plasmonic Three-Dimensional Transparent Conductor Based on Al-Doped Zinc Oxide-Coated Nanostructured Glass Using Atomic Layer Deposition. *ACS Appl. Mater. Interfaces* **2015**, *7* (16), 8556–8561.

(91) Noh, J. H.; Han, H. S.; Lee, S.; Kim, J. Y.; Hong, K. S.; Han, G. S.; Shin, H.; Jung, H. S. Nanowire-Based Three-Dimensional Transparent Conducting Oxide Electrodes for Extremely Fast Charge Collection. *Adv. Energy Mater.* **2011**, *1* (5), 829–835.

(92) Han, H. S.; Han, G. S.; Kim, J. S.; Kim, D. H.; Hong, J. S.; Caliskan, S.; Jung, H. S.; Cho, I. S.; Lee, J. K. Indium-Tin-Oxide Nanowire Array Based CdSe/CdS/TiO2 One-Dimensional Heterojunction Photoelectrode for Enhanced Solar Hydrogen Production. *ACS Sustain. Chem. Eng.* **2016**, *4* (3), 1161–1168.

(93) Krause, K. M.; Taschuk, M. T.; Harris, K. D.; Rider, D. A.; Wakefield, N. G.; Sit, J. C.; Buriak, J. M.; Thommes, M.; Brett, M. J. Surface Area Characterization of Obliquely Deposited Metal Oxide Nanostructured Thin Films. *Langmuir* **2010**, *26* (6), 4368–4376.

(94) Renault, C.; Harris, K. D.; Brett, M. J.; Balland, V.; Limoges, B. Time-Resolved UV-Visible Spectroelectrochemistry Using Transparent 3D-Mesoporous Nanocrystalline ITO Electrodes. *Chem. Commun.* **2011**, *47* (6), 1863–1865.

(95) Renault, C.; Andrieux, C. P.; Tucker, R. T.; Brett, M. J.; Balland, V.; Limoges, B. Unraveling the Mechanism of Catalytic Reduction of O 2 by Microperoxidase-11 Adsorbed within a Transparent 3D-Nanoporous ITO Film. *J. Am. Chem. Soc.* **2012**, *134* (15), 6834–6845.

(96) Schaming, D.; Renault, C.; Tucker, R. T.; Lau-Truong, S.; Aubard, J.; Brett, M. J.; Balland, V.; Limoges, B. Spectroelectrochemical Characterization of Small Hemoproteins Adsorbed within Nanostructured Mesoporous ITO Electrodes. *Langmuir*

2012, *28* (39), 14065–14072.

(97) Sood, A. W.; Poxson, D. J.; Mont, F. W.; Chhajed, S.; Cho, J.; Schubert, E. F.; Welser, R. E.; Dhar, N. K.; Sood, A. K. Experimental and Theoretical Study of the Optical and Electrical Properties of Nanostructured Indium Tin Oxide Fabricated by Oblique-Angle Deposition. *J. Nanosci. Nanotechnol.* **2012**, *12* (5), 3950–3953.

(98) Forget, A.; Tucker, R. T.; Brett, M. J.; Limoges, B.; Balland, V. Tuning the Reactivity of Nanostructured Indium Tin Oxide Electrodes toward Chemisorption. *Chem. Commun.* **2015**, *51* (32), 6944–6947.

(99) Hong, H.; Kim, S.; Kim, D. Improvement of Light Extraction for a Target Wavelength in InGaN/GaN LEDs with an Indium Tin Oxide Dual Layer by Oblique Angle Deposition. *Appl. Phys. Express* **2016**.

(100) Lin, H.; Jin, T.; Dmytruk, A.; Saito, M.; Yazawa, T. Preparation of a Porous ITO Electrode. *J. Photochem. Photobiol. A Chem.* **2004**, *164* (1–3), 173–177.

(101) Tétreault, N.; Arsenault, É.; Heiniger, L.-P.; Soheilnia, N.; Brillet, J.; Moehl, T.; Zakeeruddin, S.; Ozin, G. A.; Grätzel, M. High-Efficiency Dye-Sensitized Solar Cell with Three-Dimensional Photoanode. *Nano Lett.* **2011**, *11* (11), 4579–4584.

(102) Riha, S. C.; DeVries Vermeer, M. J.; Pellin, M. J.; Hupp, J. T.; Martinson, A. B. F. Hematite-Based Photo-Oxidation of Water Using Transparent Distributed Current Collectors. *ACS Appl. Mater. Interfaces* **2013**, *5* (2), 360–367.

(103) Stefik, M.; Cornuz, M.; Mathews, N.; Hisatomi, T.; Mhaisalkar, S.; Grätzel, M. Transparent, Conducting Nb:SnO 2 for Host–Guest Photoelectrochemistry. *Nano Lett.* **2012**, *12* (10), 5431–5435.

(104) Hernández, S.; Tortello, M.; Sacco, A.; Quaglio, M.; Meyer, T.; Bianco, S.; Saracco, G.; Pirri, C. F.; Tresso, E. New Transparent Laser-Drilled Fluorine-Doped Tin Oxide Covered Quartz Electrodes for Photo-Electrochemical Water Splitting. *Electrochim. Acta* **2014**, *131*, 184–194.

(105) Dhamodharan, P.; Manoharan, C.; Bououdina, M.; Venkadachalapathy, R.; Ramalingam, S. Al-Doped ZnO Thin Films Grown onto ITO Substrates as Photoanode in Dye Sensitized Solar Cell. *Sol. Energy* **2017**, *141*, 127–144.

(106) Lee, K.-T.; Lu, S.-Y. Porous FTO Thin Layers Created with a Facile One-Step Sn4+-Based Anodic Deposition Process and Their Potential Applications in Ion Sensing. *J. Mater. Chem.* **2012**, *22* (32), 16259.

(107) Wang, F.; Subbaiyan, N. K.; Wang, Q.; Rochford, C.; Xu, G.; Lu, R.; Elliot, A.; D'Souza, F.; Hui, R.; Wu, J. Development of Nanopatterned Fluorine-Doped Tin Oxide Electrodes for Dye-Sensitized Solar Cells with Improved Light Trapping. *ACS Appl. Mater. Interfaces* **2012**, *4* (3), 1565–1572.

(108) Lin, D.; Wu, H.; Zhang, R.; Pan, W. Preparation and Electrical Properties of Electrospun Tin-Doped Indium Oxide Nanowires. *Nanotechnology* **2007**, *18* (46), 465301.

(109) Lee, Y.-I.; Lee, K.-J.; Kim, K. D.; Kim, H. T.; Chang, Y.-W.; Kang, S.-C.; Choa, Y.-H. Synthesis and Electrical Property of Indium Tin Oxide Nanofibers Using Electrospinning Method. *J. Nanosci. Nanotechnol.* **2007**, *7* (11), 3910–3913.

(110) Munir, M. M.; Iskandar, F.; Yun, K. M.; Okuyama, K.; Abdullah, M. Optical and

Electrical Properties of Indium Tin Oxide Nanofibers Prepared by Electrospinning. *Nanotechnology* **2008**, *19* (14), 145603.

(111) Iskandar, F.; Suryamas, A. B.; Kawabe, M.; Munir, M. M.; Okuyama, K.; Tarao, T.; Nishitani, T. Indium Tin Oxide Nanofiber Film Electrode for High Performance Dye Sensitized Solar Cells. *Jpn. J. Appl. Phys.* **2010**, *49* (1 Part 1), 9–12.

(112) León-Brito, N.; Melendez, A.; Ramos, I.; Pinto, N. J.; Santiago-Aviles, J. J. Electrical Properties of Electrospun Sb-Doped Tin Oxide Nanofibers. *J. Phys. Conf. Ser.* **2007**, *61*, 683–687.

(113) Pan, W.; He, X.; Chen, Y. Preparation and Characterization of Polyacrylonitrile / Antimony Doped Tin Oxide Composite Nanofibers by Electrospinning Method. *Optoelectron. Adv. Mater. - Rapid Commun.* **2010**, *4* (3), 390–394.

(114) Wu, X.; Wang, Y.; Yang, B. Effects of Sn Doping on the Morphology, Structure, and Electrical Property of In2O3 Nanofiber Networks. *Appl. Phys. A* **2014**, *117* (2), 781–786.

(115) Wu, H.; Hu, L.; Carney, T.; Ruan, Z.; Kong, D.; Yu, Z.; Yao, Y.; Cha, J. J.; Zhu, J.; Fan, S.; Cui, Y. Low Reflectivity and High Flexibility of Tin-Doped Indium Oxide Nanofiber Transparent Electrodes. *J. Am. Chem. Soc.* **2011**, *133* (1), 27–29.

(116) Feng, Y.; Hou, W.; Zhang, X.; Lv, P.; Li, Y.; Feng, W. Highly Sensitive Reversible Light-Driven Switches Using Electrospun Porous Aluminum-Doped Zinc Oxide Nanofibers. *J. Phys. Chem. C* **2011**, *115* (10), 3956–3961.

(117) Dunkel, C.; Wark, M.; Oekermann, T.; Ostermann, R.; Smarsly, B. M. Electrodeposition of Zinc Oxide on Transparent Conducting Metal Oxide Nanofibers and Its Performance in Dye Sensitized Solar Cells. *Electrochim. Acta* **2013**, *90*, 375–381.

(118) Wu, Z.; Chen, Z.; Du, X.; Logan, J. M.; Sippel, J.; Nikolou, M.; Kamaras, K.; Reynolds, J. R.; Tanner, D. B.; Hebard, A. F.; Rinzler, A. G. Transparent, Conductive Carbon Nanotube Films. *Science* **2004**, *305* (5688), 1273–1276.

(119) Malavé Osuna, R.; Hernández, V.; López Navarrete, J. T.; Kauppinen, E. I.; Ruiz, V. Ultrafast and High-Contrast Electrochromism on Bendable Transparent Carbon Nanotube Electrodes. *J. Phys. Chem. Lett.* **2010**, *1* (9), 1367–1371.

(120) Nishihara, H.; Kwon, T.; Fukura, Y.; Nakayama, W.; Hoshikawa, Y.; Iwamura, S.; Nishiyama, N.; Itoh, T.; Kyotani, T. Fabrication of a Highly Conductive Ordered Porous Electrode by Carbon-Coating of a Continuous Mesoporous Silica Film. *Chem. Mater.* **2011**, *23* (13), 3144–3151.

(121) Jung, H. Y.; Karimi, M. B.; Hahm, M. G.; Ajayan, P. M.; Jung, Y. J. Transparent, Flexible Supercapacitors from Nano-Engineered Carbon Films. *Sci. Rep.* **2012**, *2*, 1–5.

(122) Wang, Y. S.; Li, S. M.; Hsiao, S. T.; Liao, W. H.; Yang, S. Y.; Tien, H. W.; Ma, C. C. M.; Hu, C. C. Thickness-Self-Controlled Synthesis of Porous Transparent Polyaniline-Reduced Graphene Oxide Composites towards Advanced Bifacial Dye-Sensitized Solar Cells. *J. Power Sources* **2014**, *260*, 326–337.

(123) Li, N.; Yang, G. G.; Sun, Y.; Song, H.; Cui, H.; Yang, G. G.; Wang, C. Free-Standing and Transparent Graphene Membrane of Polyhedron Box-Shaped Basic Building Units Directly Grown Using a NaCl Template for Flexible Transparent and Stretchable Solid-State Supercapacitors. *Nano Lett.* **2015**, *15* (5), 3195–3203.

(124) Li, N.; Huang, X.; Zhang, H.; Li, Y.; Wang, C. Transparent and Self-Supporting Graphene Films with Wrinkled- Graphene-Wall-Assembled Opening Polyhedron Building Blocks for High Performance Flexible/Transparent Supercapacitors. *ACS Appl. Mater. Interfaces* **2017**, *9* (11), 9763–9771.

(125) Guillemin, Y.; Etienne, M.; Aubert, E.; Walcarius, A. Electrogeneration of Highly Methylated Mesoporous Silica Thin Films with Vertically-Aligned Mesochannels and Electrochemical Monitoring of Mass Transport Issues. *J. Mater. Chem.* **2010**, *20*, 6799.

(126) Walcarius, A.; Nasraoui, R.; Wang, Z.; Qu, F.; Urbanova, V.; Etienne, M.; Göllü, M.; Demir, A. S.; Gajdzik, J.; Hempelmann, R. Factors Affecting the Electrochemical Regeneration of NADH by (2,2'-bipyridyl) (Pentamethylcyclopentadienyl)-Rhodium Complexes: Impact on Their Immobilization onto Electrode Surfaces. *Bioelectrochemistry* **2011**, *82* (1), 46–54.

(127) Menzel, N.; Ortel, E.; Kraehnert, R.; Strasser, P. Electrocatalysis Using Porous Nanostructured Materials. *Chemphyschem* **2012**, *13* (6), 1385–1394.

(128) Walcarius, A. Template-Directed Porous Electrodes in Electroanalysis. *Anal. Bioanal. Chem.* **2010**, *396* (1), 261–272.

(129) Zhang, Y.; Feng, H.; Wu, X.; Wang, L.; Zhang, A.; Xia, T.; Dong, H.; Li, X.; Zhang, L. Progress of Electrochemical Capacitor Electrode Materials: A Review. *Int. J. Hydrogen Energy* **2009**, *34* (11), 4889–4899.

(130) Walcarius, A. Electrocatalysis, Sensors and Biosensors in Analytical Chemistry Based on Ordered Mesoporous and Macroporous Carbon-Modified Electrodes. *Trends Anal. Chem.* **2012**, *38*, 79–97.

(131) Etienne, M.; Zhang, L.; Vilà, N.; Walcarius, A. Mesoporous Materials-Based Electrochemical Enzymatic Biosensors. *Electroanalysis* **2015**, *27* (9), 2028–2054.

(132) Topoglidis, E.; Campbell, C. J.; Cass, A. E. G.; Durrant, J. R. Factors That Affect Protein Adsorption on Nanostructured Titania Films . A Novel Spectroelectrochemical Application to Sensing. *Langmuir* **2001**, No. 13, 7899–7906.

(133) Frasca, S.; Richter, C.; von Graberg, T.; Smarsly, B. M.; Wollenberger, U. Electrochemical Switchable Protein-Based Optical Device. *Eng. Life Sci.* **2011**, *11* (6), 554–558.

(134) León, L.; Maraver, J. J.; Carbajo, J.; Mozo, J. D. Simple and Multi-Configurational Flow-Cell Detector for UV–vis Spectroelectrochemical Measurements in Commercial Instruments. *Sensors Actuators B Chem.* **2013**, *186*, 263–269.

(135) Kim, H.; Piqué, A.; Horwitz, J. S.; Mattoussi, H.; Murata, H.; Kafafi, Z. H.; Chrisey, D. B. Indium Tin Oxide Thin Films for Organic Light-Emitting Devices. *Appl. Phys. Lett.* **1999**, *74* (23), 3444–3446.

(136) Kim, J. S.; Granström, M.; Friend, R. H.; Johansson, N.; Salaneck, W. R.; Daik, R.; Feast, W. J.; Cacialli, F. Indium–tin Oxide Treatments for Single- and Double-Layer Polymeric Light-Emitting Diodes: The Relation between the Anode Physical, Chemical, and Morphological Properties and the Device Performance. *J. Appl. Phys.* **1998**, *84* (12), 6859–6869.

(137) Kim, J. K. K.; Chhajed, S.; Schubert, M. F. F.; Schubert, E. F. F.; Fischer, A. J. J.; Crawford, M. H. H.; Cho, J.; Kim, H.; Sone, C. Light-Extraction Enhancement of GaInN Light-Emitting Diodes by Graded-Refractive-Index Indium Tin Oxide Anti-

Reflection Contact. *Adv. Mater.* **2008**, *20* (4), 801–804.

(138) Choi, H.-J.; Yoon, S.-G.; Lee, J.-H.; Lee, J.-Y. Crystallized Indium-Tin Oxide (ITO) Thin Films Grown at Low Temperature onto Flexible Polymer Substrates. *ECS J. Solid State Sci. Technol.* **2012**, *1* (5), Q106–Q109.

(139) Harris, K. D.; van Popta, A. C.; Sit, J. C.; Broer, D. J.; Brett, M. J. A Birefringent and Transparent Electrical Conductor. *Adv. Funct. Mater.* **2008**, *18* (15), 2147–2153.

(140) Zuev, D. a.; Lotin, a. a.; Novodvorsky, O. a.; Lebedev, F. V.; Khramova, O. D.; Petuhov, I. a.; Putilin, P. N.; Shatohin, a. N.; Rumyanzeva, M. N.; Gaskov, a. M. Pulsed Laser Deposition of ITO Thin Films and Their Characteristics. *Semiconductors* **2012**, *46* (3), 410–413.

(141) Chen, H.; Zhu, L.; Liu, H.; Li, W. ITO Porous Film-Supported Metal Sulfide Counter Electrodes for High-Performance Quantum-Dot-Sensitized Solar Cells. *J. Phys. Chem. C* **2013**, *117* (8), 3739–3746.

(142) Sun, X.; Shi, Y.; Ji, H.; Li, X.; Cai, S.; Zheng, C. Nanocasting Synthesis of Ordered Mesoporous Indium Tin Oxide (ITO) Materials with Controllable Particle Size and High Thermal Stability. *J. Alloys Compd.* **2012**, *545*, 5–11.

(143) Walcarius, A.; Minteer, S. D.; Wang, J.; Lin, Y.; Merkoçi, A. Nanomaterials for Bio-Functionalized Electrodes: Recent Trends. *J. Mater. Chem. B* **2013**, *1* (38), 4878–4908.

(144) Xiong, W.; Qu, Q.; Liu, S. Self-Assembly of Ultra-Small Gold Nanoparticles on an Indium Tin Oxide Electrode for the Enzyme-Free Detection of Hydrogen Peroxide. *Microchim. Acta* **2014**, *181* (9–10), 983–989.

(145) Kovtyukhova, N. I.; Mallouk, T. E. Conductive Indium-Tin Oxide Nanowire and Nanotube Arrays Made by Electrochemically Assisted Deposition in Template Membranes: Switching between Wire and Tube Growth Modes by Surface Chemical Modification of the Template. *Nanoscale* **2011**, *3* (4), 1541–1552.

(146) Zhang, X. X.; Man, Y.; Wang, J.; Liu, C.; Wu, W. Synthesis of 3D Ordered Macroporous Indium Tin Oxide Using Polymer Colloidal Crystal Template. *Sci. China Ser. E Technol. Sci.* **2006**, *49* (5), 537–546.

(147) Qi, Q.; Zou, Y.-C.; Fan, M.-H.; Liu, Y.-P.; Gao, S.; Wang, P.-P.; He, Y.; Wang, D.-J.; Li, G.-D. Trimethylamine Sensors with Enhanced Anti-Humidity Ability Fabricated from La0.7Sr0.3FeO3 Coated In2O3–SnO2 Composite Nanofibers. *Sensors Actuators B Chem.* **2014**, *203*, 111–117.

(148) Tao, L.; Xiwen, D. Enhanced Interfacial Adhesion of Nanofibers with Conductive Glass Substrate for Photovoltaic Application. *paper.edu.cn* **2013**, 1–9.

(149) Demir, M. M.; Yilgor, I.; Yilgor, E.; Erman, B. Electrospinning of Polyurethane Fibers. *Polymer (Guildf).* **2002**, *43*, 3303–3309.

(150) Holzmeister, A.; Rudisile, M.; Greiner, A.; Wendorff, J. H. Structurally and Chemically Heterogeneous Nanofibrous Nonwovens via Electrospinning. *Eur. Polym. J.* **2007**, *43* (12), 4859–4867.

(151) Deitzel, J. .; Kleinmeyer, J.; Harris, D.; Beck Tan, N. . The Effect of Processing Variables on the Morphology of Electrospun Nanofibers and Textiles. *Polymer (Guildf).* **2001**, *42* (1), 261–272.

(152) Yördem, O. S. O. S.; Papila, M.; Menceloğlu, Y. Z.; Menceloğlu, Y. Z. Effects of

Electrospinning Parameters on Polyacrylonitrile Nanofiber Diameter: An Investigation by Response Surface Methodology. *Mater. Des.* **2008**, *29* (1), 34–44.

(153) Basu, S.; Agrawal, A. K.; Jassal, M. Concept of Minimum Electrospinning Voltage in Electrospinning of Polyacrylonitrile N,N-Dimethylformamide System. *J. Appl. Polym. Sci.* **2011**, *122*, 856–866.

(154) Theron, S. a.; Zussman, E.; Yarin, a. L. Experimental Investigation of the Governing Parameters in the Electrospinning of Polymer Solutions. *Polymer (Guildf).* **2004**, *45* (6), 2017–2030.

(155) Kim, J.; Kang, J.; Jeong, U.; Kim, H.; Lee, H. Catalytic, Conductive, and Transparent Platinum Nanofiber Webs for FTO-Free Dye-Sensitized Solar Cells. *ACS Appl. Mater. Interfaces* **2013**, *5* (8), 3176–3181.

(156) Ba, J.; Fattakhova-Rohlfing, D.; Feldhoff, A.; Brezesinski, T.; Djerdj, I.; Wark, M.; Niederberger, M. Nonaqueous Synthesis of Uniform Indium Tin Oxide Nanocrystals and Their Electrical Conductivity in Dependence of the Tin Oxide Concentration. *Chem. Mater.* **2006**, *18*, 2848–2854.

(157) Ito, D.; Masuko, K.; Weintraub, B. a.; McKenzie, L. C.; Hutchison, J. E. Convenient Preparation of ITO Nanoparticles Inks for Transparent Conductive Thin Films. *J. Nanoparticle Res.* **2012**, *14* (12), 1274.

(158) Samiee, L.; Beitollahi, A.; Vinu, A. Effect of Calcination Atmosphere on the Structure and Photocatalytic Properties of Titania Mesoporous Powder. *Res. Chem. Intermed.* **2012**, *38* (7), 1467–1482.

(159) Baig, A. A.; Fox, J. L.; Young, R. A.; Wang, Z.; Hsu, J.; Higuchi, W. I.; Chhettry, A.; Zhuang, H.; Otsuka, M. Relationships Among Carbonated Apatite Solubility, Crystallite Size, and Microstrain Parameters. *Calcif. Tissue Int.* **1999**, *64* (5), 437–449.

(160) Jia, F.; Yu, C.; Ai, Z.; Zhang, L. Fabrication of Nanoporous Gold Film Electrodes with Ultrahigh Surface Area and Electrochemical Activity. *Chem. Mater.* **2007**, No. 19, 3648–3653.

(161) Shin, C.; Shin, W.; Hong, H.-G. Electrochemical Fabrication and Electrocatalytic Characteristics Studies of Gold Nanopillar Array Electrode (AuNPE) for Development of a Novel Electrochemical Sensor. *Electrochim. Acta* **2007**, *53* (2), 720–728.

(162) Skrovankova, S.; Mlcek, J.; Sochor, J.; Baron, M.; Kynicky, J.; Jurikova, T. Determination of Ascorbic Acid by Electrochemical Techniques and Other Methods. *Int. J. Electrochem. Sci.* **2015**, *10*, 2421–2431.

(163) Wei, M.-Y.; Huang, R.; Guo, L.-H. High Catalytic Activity of Indium Tin Oxide Nanoparticle Modified Electrode towards Electro-Oxidation of Ascorbic Acid. *J. Electroanal. Chem.* **2012**, *664*, 156–160.

(164) Yan, X.; Mont, F. W.; Poxson, D. J.; Schubert, M. F.; Kim, J. K.; Cho, J.; Schubert, E. F. Refractive-Index-Matched Indium–Tin-Oxide Electrodes for Liquid Crystal Displays. *Jpn. J. Appl. Phys.* **2009**, *48* (12), 120203.

(165) Vicente, F.; Roig, A.; Navarro, J.; Garcia, J. J.; Vicente, F. VOLTAMMETRIC STUDY ON THE STABILITY OF DEPOSITED PRUSSIAN BLUE FILMS AGAINST. *Electrochim. Acta* **1994**, *39* (3), 437–442.

(166) Sandana, V. E.; Rogers, D. J.; Teherani, F. H.; Bove, P.; Razeghi, M.; Chevreuse, D.

Graphene versus Oxides for Transparent Electrode Applications. *Conf. Oxide-Based Mater. Devices IV* **2013**, *8626*, 1–9.

(167) Lee, K. T.; Lytle, J. C.; Ergang, N. S.; Oh, S. M.; Stein, A. Synthesis and Rate Performance of Monolithic Macroporous Carbon Electrodes for Lithium-Ion Secondary Batteries. *Adv. Funct. Mater.* **2005**, *15* (4), 547–556.

(168) Woo, E. M.; Lee, M. L.; Sun, Y. S. Interactions between Polystyrenes of Different Tacticities and Thermal Evidence for Miscibility. *Polymer (Guildf).* **2000**, *41* (3), 883–890.

(169) Wang, Z. M.; Chung, T. C.; Gilman, J. W.; Manias, E. Melt-Processable Syndiotactic Polystyrene / Montmorillonite. *J. Polym. Sci. Part B Polym. Phys.* **2003**, *41*, 3173–3187.

(170) Szamocki, R.; Reculusa, S.; Ravaine, S.; Bartlett, P. N.; Kuhn, A.; Hempelmann, R. Tailored Mesostructuring and Biofunctionalization of Gold for Increased Electroactivity. *Angew. Chem. Int. Ed.* **2006**, *45* (8), 1317–1321.

(171) Sohrabnezhad, S.; Pourahmad, A.; Radaee, E. Photocatalytic Degradation of Basic Blue 9 by CoS Nanoparticles Supported on AlMCM-41 Material as a Catalyst. *J. Hazard. Mater.* **2009**, *170* (1), 184–190.

(172) Upendar, G.; Dutta, S.; Chakraborty, J.; Bhattacharyya, P. Removal of Methylene Blue Dye Using Immobilized Bacillus Subtilis in Batch & Column Reactor. *Mater. Today Proc.* **2016**, *3* (10), 3467–3472.

(173) Senthilkumaar, S.; Varadarajan, P. R.; Porkodi, K.; Subbhuraam, C. V. Adsorption of Methylene Blue onto Jute Fiber Carbon: Kinetics and Equilibrium Studies. *J. Colloid Interface Sci.* **2005**, *284* (1), 78–82.

(174) He, Y.; Ding, L.; Su, B. Vertically Ordered Silica Mesochannels as Preconcentration Materials for the Electrochemical Detection of Methylene Blue. *Sci. China Chem.* **2015**, *58* (10), 1593–1599.

(175) Hassan, S. S.; Nafady, A.; Sirajuddin; Solangi, A. R.; Kalhoro, M. S.; Abro, M. I.; Sherazi, S. T. H. Ultra-Trace Level Electrochemical Sensor for Methylene Blue Dye Based on Nafion Stabilized Ibuprofen Derived Gold Nanoparticles. *Sensors Actuators, B Chem.* **2015**, *208*, 320–326.

(176) Tonlé, I. K.; Ngameni, E.; Tcheumi, H. L.; Tchiéda, V.; Carteret, C.; Walcarius, A. Sorption of Methylene Blue on an Organoclay Bearing Thiol Groups and Application to Electrochemical Sensing of the Dye. *Talanta* **2008**, *74* (4), 489–497.

(177) Li, J.; Zhao, F.; Zhao, J.; Zeng, B. Adsorptive and Stripping Behavior of Methylene Blue at Gold Electrodes in the Presence of Cationic Gemini Surfactants. *Electrochim. Acta* **2005**, *51* (2), 297–303.

(178) Wen, M. L.; Zhao, Y. Bin; Chen, X.; Wang, C. Y. Potentiometric Sensor for Methylene Blue Based on Methylene Blue – Silicotungstate Ion Association and Its Pharmaceutical Applications. *J. Pharm. Biomed. Anal.* **1999**, *18*, 957–961.

(179) Yu, X. Z.; Feng, Y. X.; Yue, D. M.; Science, E. Phytotoxicity of Methylene Blue to Rice Seedlings. *Glob. J. Environ. Sci. Manag.* **2015**, *1* (3), 199–204.

(180) Bertoncello, P.; Forster, R. J. Nanostructured Materials for Electrochemiluminescence (ECL)-Based Detection Methods: Recent Advances and Future Perspectives. *Biosens.*

Bioelectron. **2009**, *24* (11), 3191–3200.

(181) Miao, W. Electrogenerated Chemiluminescence and Its Biorelated Applications. *Chem. Rev.* **2008**, *108* (7), 2506–2553.

(182) Zhou, Z.; Guo, W.; Xu, L.; Yang, Q.; Su, B. Two Orders-of-Magnitude Enhancement in the Electrochemiluminescence of by Vertically Ordered Silica Mesochannels. *Anal. Chim. Acta* **2015**, *886*, 48–55.

(183) Shan, D.; Qian, B.; Ding, S. N.; Zhu, W.; Cosnier, S.; Xue, H. G. Enhanced Solid-State Electrochemiluminescence of tris(2,2′-Bipyridyl) ruthenium(II) Incorporated into Electrospun Nanofibrous Mat. *Anal. Chem.* **2010**, *82* (13), 5892–5896.

(184) Kado, T.; Takenouchi, M.; Okamoto, S.; Takashima, W.; Kaneto, K.; Hayase, S. Enhanced Electrochemiluminescence by Use of Nanoporous TiO2 Electrodes: Electrochemiluminescence Devices Operated with Alternating Current. *Japanese J. Appl. Physics, Part 1 Regul. Pap. Short Notes Rev. Pap.* **2005**, *44* (11), 8161–8164.

(185) Lin, J.; Wu, H.; Lu, L.; Sun, Z.; Zhang, Y.; Dang, F.; Qian, L. Porous Graphene Containing Immobilized Ru(II) Tris-Bipyridyl for Use in Electrochemiluminescence Sensing of Tripropylamine. *Microchim. Acta* **2016**, No. Ii, 1–7.

(186) Miao, W.; Choi, J.-P.; Bard, A. J. Electrogenerated Chemiluminescence 69: The Tris(2,2'-bipyridine)ruthenium(II), (Ru(bpy) 3 2+)/Tri- N -Propylamine (TPrA) System RevisitedA New Route Involving TPrA •+ Cation Radicals. *J. Am. Chem. Soc.* **2002**, *124* (48), 14478–14485.